INSTITUTO NACIONAL DE PESQUISAS ESPACIAIS
Instituto Nacional de Pesquisas Espaciais
Coordenação-Geral de Engenharia, Tecnologia e Ciência Espaciais
Divisão de Clima Espacial

Memorando nº 11875/2025/INPE

São José dos Campos, 01 de Setembro de 2025

Ao Senhor José Aristeu de Souza Ruas
Serviço de Compras, Recebimento e Importação (SECRI)

Assunto: **Solicitação de Estimativa de Custos**

1. Peço, por gentileza, as providências necessárias para a emissão da Estimativa de Custos da cotação anexa.

Dados Orçamentários (INPE/CGCE):

PTRes - 233467
PI - 955656-PO09
FR - 1000

Atenciosamente,

(Assinado Eletronicamente)

Luis Eduardo Antunes Vieira
Pesquisador
Divisão de Heliofísica,
Ciências Planetárias e Aeronomia
SIAPE 1177754

Draft version August 18, 2025
Typeset using LaTeX **default** style in AASTeX7

Assessment of Daytime Sky Quality and Atmospheric Refractive Index (C_n^2) Analysis at Pico dos Dias Observatory

Edith T. Cuadros,[1] Adriano P. Almeida,[1] Franciele Carlesso,[1] David Pareja-Quispe,[2] Fernando L. Guarnieri,[1] Alisson Dal Lago,[1] Saulo R. Gargaglioni,[3] and Luis E. A. Vieira[1]

[1] *National Institute for Space Research – INPE, São José dos Campos, SP, Brazil*
[2] *Universidad Nacional Mayor de San Marcos, Lima, Perú*
[3] *Brazilian National Laboratory of Astrophysics –LNA, Itajubá, MG, Brazil*

ABSTRACT

Ground-based astronomical and Solar observations are strongly influenced by atmospheric turbulence, a dynamic phenomenon that degrades optical resolution through refractive index fluctuations. This study evaluates daytime sky quality and the refractive index structure parameter (C_n^2) at Pico dos Dias Observatory (OPD) in Brazil, integrating in situ meteorological data with the **product of European Centre for Medium-Range Weather Forecasts Reanalysis version 5**. Variables such as air temperature, wind speed, relative humidity, and cloud cover **are** analyzed across vertical and temporal scales, providing insights into diurnal, seasonal, and altitudinal atmospheric behaviors. The study highlights the distinct challenges posed by daytime turbulence, driven by solar heating and convection, on adaptive optics (AO) systems and high-precision solar spectropolarimetric instruments, such as **the prototype of the** Galileo Solar Space Telescope (GSST). **To provide context for the atmospheric conditions at the OPD, this study characterizes several key meteorological variables. Typical daytime conditions feature median air temperatures of 15–20°C and surface winds of 1.0–4.0 m/s, predominantly from the north, while nighttime conditions are cooler (10–15°C) with weaker winds shifting south-southeast. Relative humidity generally remains below 70%, especially in JJA months, favorable for astronomical observations. Cloud cover shows seasonality, with clear-sky fractions of about** 32% **at night and** 28% **by day, peaking in austral winter and minimizing in summer**. **Our** quantitative analysis of refractive index variability underscores the necessity of advanced AO technologies. Seasonal and vertical profiles of C_n^2 **present** pronounced variability, influenced by solar heating, terrain-induced airflow, and jet stream dynamics. **These findings** stress the importance of strategic scheduling and turbulence modeling to optimize performance. This comprehensive characterization advances understanding of atmospheric conditions for solar and nighttime astronomy, refining AO systems and enabling progress in high-precision astrophysics.

Keywords: Daytime sky quality — Atmospheric turbulence — Refractive index structure parameter

1. INTRODUCTION

The Galileo Solar Space Telescope (GSST) represents a pioneering Brazilian initiative developed by the National Institute for Space Research (INPE) in collaboration with the Brazilian Space Agency (AEB). Designed to provide highly accurate measurements of the solar magnetic field, it aims to enhance scientific understanding of solar magnetic processes. Using imaging spectropolarimetry and radiative transfer theory, the GSST applies a well-established diagnostic approach to study the Sun's magnetic field. To fulfill its core goal of investigating the development and lifecycle of solar magnetic structures, the GSST integrates observational data collected from both ground and space-based platforms.

Email: edith.cuadros@inpe.br

At the current stage of development, an operational ground prototype is set to be deployed at the Pico dos Dias Observatory, managed by the Brazilian National Laboratory for Astrophysics (LNA). This prototype incorporates a 50 cm diameter mirror, **which has a diffraction limit of approximately** 0.25 **arcseconds at** $\lambda = 500$ nm**, corresponding to a** 400×400 **arcsecond field of view (T. R. Rimmele & J. Marino 2011)**, allowing for highly detailed solar observations. The GSST prototype features a spectropolarimeter and is designed to study heating processes in the Sun's outer layers through the Fe I 630.25 nm spectral line (G. Giono et al. 2015). Imaging spectropolarimetry's effectiveness primarily depends on observation quality, which is affected by atmospheric turbulence. These disturbances arise from fluctuations in the refractive index due to temperature changes, leading to spatial phase distortions that degrade image quality. During polarization modulation, intensity fluctuations caused by seeing can introduce false polarization signals. **Although the sky polarization produced by atmospheric scattering becomes negligible when the solar disk is observed in a direct-incidence geometry (J. de la Cruz Rodriguez et al. 2015; T. Song et al. 2020), spurious seeing-induced crosstalk is not suppressed by solar brightness. Its mitigation instead relies on high-frequency modulation (**≥ 100 **Hz) and, preferably, on dual-beam polarimetric configurations (F. A. Iglesias & A. Feller 2019).**

Atmospheric turbulence, characterized by spatial and temporal variability driven by factors such as altitude, geographic location, and meteorological conditions, presents challenges for solar observations. Mitigating these effects relies heavily on **AO** systems, which are essential for real-time correction of wavefront distortions (T. R. Rimmele & J. Marino 2011; J. W. Hardy 1998). **These systems actively compensate for wavefront distortions in real-time, allowing ground-based telescopes to achieve near-diffraction-limited imaging (L. Zhong et al. 2020; Z. Wang et al. 2018). The OPD -** LNA, was initially designed for nighttime astronomy, where seeing conditions are evaluated using stellar images. While nighttime turbulence at OPD is measurable and relatively stable over short periods of time, it still poses several challenges. By contrast, daytime conditions are much more variable due to ground-level turbulence driven by solar heating, creating obstacles for AO system (I. Galaktionov et al. 2023). These systems lack access to point-like stellar references for wavefront sensing during daytime, relying instead on **small solar structures**, which **can evolve** on minute-long scales and complicates real-time wavefront sensing and correction (A. Y. Shikhovtsev 2024).

Turbulence within the Earth's atmosphere introduces distortions to incoming wavefronts, resulting in image blur, scintillation, and loss of resolution, a phenomenon commonly referred to as **astronomical or atmospheric seeing** (J. Vernin & C. Muñoz-Tuñón 1992; A. Tokovinin 2023; A. Y. Shikhovtsev et al. 2024a). These distortions are **characterized** governed by the refractive index structure constant (C_n^2) and the resulting Fried parameter (r_0), which provide a quantitative measure of optical turbulence strength (A. Y. Shikhovtsev et al. 2024a,b). The impact of atmospheric conditions spatial and temporal variability, driven by factors such as altitude, geographic location, and local meteorological patterns, presents challenges from ground-based **observations** (J. A. Hellemeier et al. 2019; S. L. Hidalgo et al. 2021).

Thorough knowledge of atmospheric properties and their effects on wavefront aberrations is critical for the effective design and implementation of AO systems. The Kolmogorov model is widely regarded as the foundational framework for characterizing atmospheric turbulence, quantifying turbulence strength as a function of altitude through the C_n^2. Recognizing the significance of C_n^2 is essential, as it serves as an important parameter of the Kolmogorov turbulence model. However, direct measurements of C_n^2 are costly and technically demanding, often requiring balloon-borne microthermometry. Recent studies highlight that reanalysis datasets, such as ERA5, offer practical and economical methods for estimating turbulence profiles (A. Shikhovtsev et al. 2019; A. Y. Shikhovtsev 2024). Given these challenges and needs, this study examines daytime sky conditions and the C_n^2 at the OPD using ERA5 reanalysis data. This characterization of atmospheric turbulence seeks to improve the performance of AO systems, optimize observational scheduling, and advance the GSST's scientific goals in high-precision solar spectropolarimetry. Finally, this work aims to bridge knowledge gaps in daytime atmospheric turbulence and its impact on solar observational capabilities.

2. STUDY AREA

The **OPD**, operated by the **LNA**, is located between the municipalities of Brazópolis and Piranguçu in Minas Gerais, Brazil, at an altitude of 1864 meters – approximately 900 meters above the regional average elevation. The observatory's precise geographical coordinates are 22°32′04" S and 45°34′57" W. The mountainous terrain of the area, characterized by peaks and valleys exerts a decisive influence on the modulation of regional meteorological patterns, directly impacting atmospheric dynamics. Elevated terrains act as barriers to atmospheric flow, promoting phenomena such as orographic blocking and the forced ascent of air masses, resulting in orographic precipitation and cloud formation (B. Jiménez-Esteve & D. I. Domeisen 2022). Furthermore, terrain slope shows a stronger correlation with lightning density in storms than altitude itself, demonstrating that slope enhances updraft that intensify the formation of convective storms (V. Bourscheidt et al. 2009). Orographic elevations promote the forced ascent of air masses, leading to adiabatic cooling, condensation, and orographic precipitation, a process widely documented in tropical and subtropical regions (L. A. Machado et al. 2018).

Figure 1 shows the study area. In the upper right corner, Figure 1 displays a panoramic photograph of **OPD**, where the white domes of the telescopes are surrounded by vegetation, with mountains in the background, highlighting the elevated and remote location of the site. In the lower right corner, **the** figure includes a broader context map that situates the region within Brazil, with a red box highlighting the area where the observatory is located. To the left of the figure, the geographical location of the Pico dos Dias Observatory is shown, marked by a red triangle, in the state of Minas Gerais. The area's rugged topography is also visible. Light blue and green shades represent the lower regions (below 880 m), while yellow, orange, and brown tones indicate the higher areas, varying between 880 and 2,199 m.

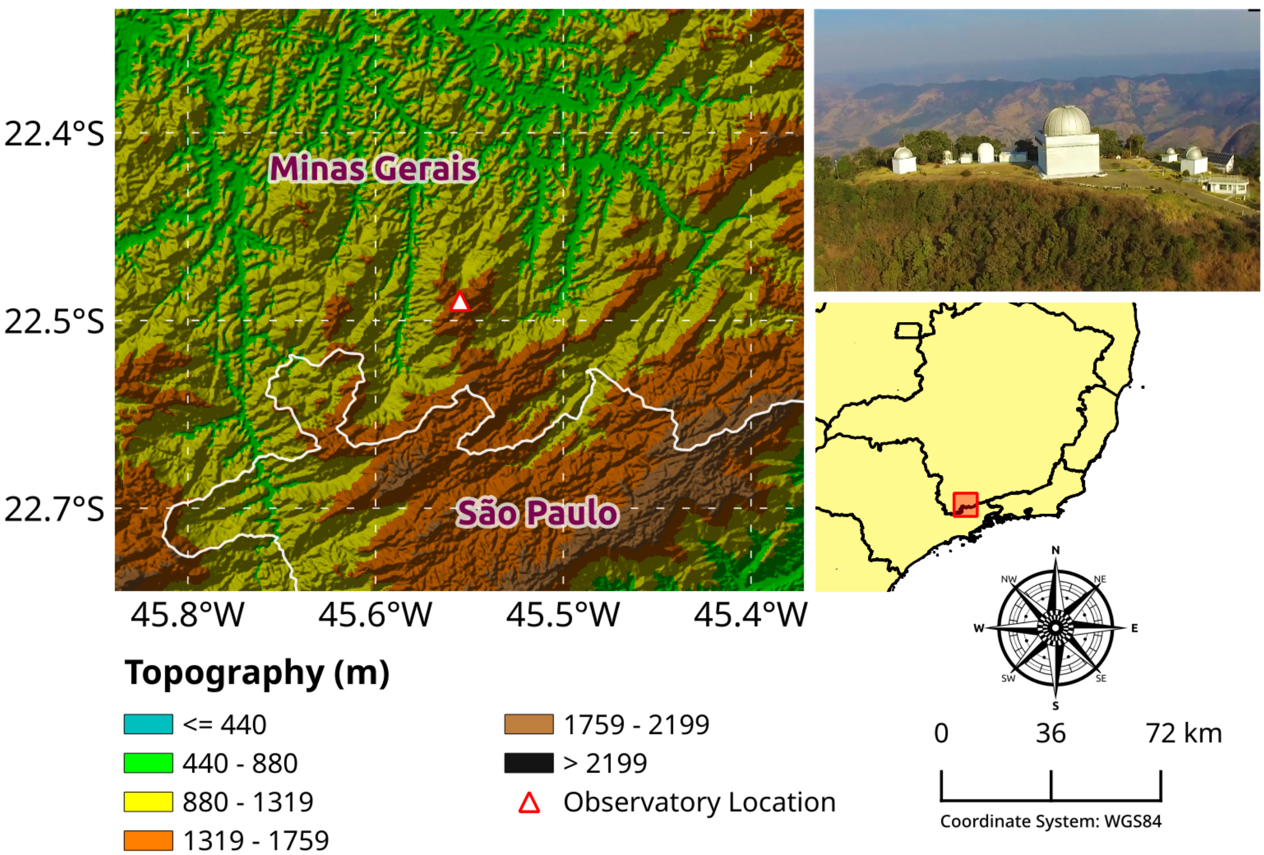

Figure 1. Study area overview highlighting the location of Pico dos Dias Observatory. The topographical map displays elevation ranges in the region, with the observatory location marked by a red triangle at coordinates $22°32'04''$ S and $45°34'57''$ W. The map covers parts of the states of Minas Gerais and São Paulo, Brazil, with topographical variations ranging from lowlands (≤ 440 m) to highlands (> 2199 m). The inset in the lower right of the topography map provides a regional context within Brazil, indicating the broader study area. An image of the observatory facilities is included to illustrate its infrastructure. The projection of the topography map follows the WGS84 coordinate system.

3. DATA

This study **uses** data from meteorological stations and reanalysis datasets. Due to the extensive temporal coverage and the availability of a wide range of meteorological variables, including vertical profiles and surface data, the primary analyses were based on reanalysis data. Data from meteorological stations **are** used to validate the reanalysis outputs, ensuring consistency with observed values. Detailed descriptions of the datasets are provided in the following subsections.

3.1. *Weather station data*

In this study, reference data were obtained from the Davis Vantage Pro2 meteorological station, a globally recognized system for monitoring atmospheric conditions. Located at the **OPD**, this station provides highly accurate, reliable measurements that meet or exceed international meteorological standards

The station comprises an Integrated Sensor Suite (ISS), which transmits data to the console via wireless or cabled connections. The ISS features a thermometer with an accuracy of $\pm 0.5^{o}$C, a hygrometer with $\pm 3\%$ precision, a barometer capable of recording pressure with an accuracy of ± 1 hPa, and an anemometer that measures wind speed with a resolution of 1 km/h and directional accuracy of $\pm 3^{o}$. In addition, the rain gauge employs a tipping bucket mechanism to measure precipitation with a resolution of 0.2 mm, calibrated both for imperial and metric units. This and other information are available in the instrument manual [4].

Data were collected by the station at a 5-minute cadence, thereby providing a high temporal resolution for atmospheric analyses. Furthermore, the system adheres to the guidelines of the World Meteorological Organization (WMO), enhancing its suitability for scientific validation and long-term monitoring. Using Davis Vantage Pro2's advanced features and robust data collection capabilities, **ensures** that the observational data used to validate the reanalysis datasets **are** accurate and reliable.

Although the observed data have a temporal resolution of 5 minutes, they **are** averaged to match the temporal scale of the reanalysis data, which is 1 hour. During preprocessing, a quality control procedure was also applied to ensure that each integrated hour includes all observations within that interval.

3.2. *Reanalysis data*

This study uses data from the European Centre for Medium-Range Weather Forecasts Reanalysis version 5 (ERA5), a widely used global reanalysis dataset. ERA5 provides hourly estimates of atmospheric variables at a global scale with a horizontal resolution of approximately 31 km (H. Hersbach et al. 2020) **and is selected for its extensive temporal and spatial coverage and demonstrated accuracy in data-sparse regions (C. Haslebacher et al. 2022)**. It is widely recognized for its high-quality data, derived from the assimilation of observations from satellites and ground-based sources. **ERA5's hourly, multi-decadal fields are therefore widely adopted in meteorology, climatology, and numerical weather and climate modelling (P. R. Zanin et al. 2024; M. Lagos-Zuniga et al. 2022; P. R. Zanin & P. Satyamurty 2021; S. M. Vicente-Serrano et al. 2023). In the astronomical domain, ERA5 reanalysis also demonstrated significant value. For instance, L. Zhu et al. (2023) validated ERA5-based seeing forecasts at several major Chilean observatories, while C. Bi et al. (2023) showed that ERA5-derived turbulence and cloud-cover fields can be used to rank candidate telescope sites in western China. Together, these studies confirm that ERA5 accurately reproduces key astroclimatic parameters (seeing, C_n^2, precipitable-water vapour and cloud fraction) with sufficient fidelity to guide site selection, inform adaptive optics design and even quantify the impacts of climate change on leading observatories (A. Y. Shikhovtsev & P. G. Kovadlo 2024; R. Priyatikanto et al. 2024; C. Haslebacher et al. 2022).**

The ERA5 dataset provides atmospheric parameters on both single levels (e.g., surface or near-surface variables) and pressure levels, ranging from the lower troposphere (1000 hPa) to the upper stratosphere (1 hPa), enabling investigations into vertical atmospheric structures and processes. In this study, single level data were used to compare with observed measurements and to support some analyses. The variables used include wind speed and direction, air temperature, dew point and sea-level pressure. Data at pressure levels were employed to analyze vertical atmospheric profiles and calculate the refractive index structure parameter (C_n^2). Variables such as wind speed and direction, air temperature, dew point, specific humidity, relative humidity, and cloud cover (low, medium, high, and total) were extracted from these pressure levels, providing essential information for understanding atmospheric dynamics and vertical stratification. ERA5 data were obtained for the region surrounding the observatory's coordinates, as illustrated in Figure 1, covering the period from January 1, 1999, to December 31, 2023. During the preprocessing stage, time series were extracted for both the single level and pressure level products corresponding to the grid point

[4] https://support.davisinstruments.com/article/y4cq28mflh-vantage-pro2-console-user-manual

Table 1. List of variables used in this study, organized according to their data source. Derived variables **are** calculated as needed to ensure consistency and facilitate comprehensive atmospheric analysis.

Source	Variable	Unit
Weather station	Air temperature	°C
	Dew point temperature	°C
	Pressure	hPa
	Wind speed	km/h
ERA5 single level	Air temperature	K
	Dew point temperature	K
	10m U-component of neutral wind	m/s
	10m V-component of neutral wind	m/s
	Cloud cover (low, medium, high, total)	Fraction (0–1)
	Sea-level pressure	Pa
ERA5 pressure level	Air temperature	K
	Dew point temperature	K
	U-component of neutral wind	m/s
	V-component of neutral wind	m/s
	Specific humidity	kg/kg
	Relative humidity	%

nearest to the observatory's coordinates. After extracting the time series, the observed and ERA5 data were converted to compatible units, and the necessary derived variables were generated. Based on this processed dataset, the analyses presented in this study were conducted. Table 1 shows all the variables for each source.

4. METHODOLOGY

To ensure high reliability and precision in the analysis, the initial phase of this study **addresses** biases present in meteorological data from weather stations. Using the 3σ standard deviation method, a statistical technique for detecting significant deviations from the mean **(V. Barnett & T. Lewis 1994)**, outliers were identified and either adjusted when feasible or removed to maintain dataset integrity. This preprocessing step **played a** crucial in reducing systematic errors that could otherwise compromise subsequent analyses.

The weather station data **are** systematically compared **to** the ERA5 reanalysis dataset (Single Level) to evaluate the fidelity of ERA5 in representing atmospheric variables in the study region. This comparison **is** pivotal in assessing the applicability of ERA5 data as a proxy for direct observational data in astronomical studies. Variables analyzed at the surface level included air temperature at 2 m and wind speed, both evaluated on an hourly basis, segregating daytime and nighttime observations. These variables are critical due to their direct influence on atmospheric stability and sky transparency, which are key factors for astronomical observations.

To evaluate the agreement between the datasets, the Pearson correlation coefficient, mean absolute error (MAE), and root mean square error (RMSE), **are** utilized. High correlation values, combined with low MAE and RMSE, indicate strong dataset alignment, confirming ERA5 as a dependable proxy in areas with sparse in-situ observations.

Atmospheric conditions at various pressure levels are important for optimizing astronomical observations. In the absence of radiosonde measurements, ERA5 reanalysis data **provide** a dependable alternative, offering detailed vertical atmospheric profiles. Hourly evaluations of variables, including humidity, air temperature, and wind, **are** conducted across various pressure levels, distinguishing between daytime and nighttime, as well as seasonal variations. This method **provide** a detailed understanding of atmospheric dynamics influencing sky quality and observational precision. Vertical profiles **provide** details on atmospheric stratification and turbulence, important features for observations at the **OPD**.

Temperature and wind variables across all ERA5 pressure levels **are** analyzed using spectral power density techniques to determine dominant frequencies and characterize turbulence scales. This approach provided insights into atmospheric transparency and the propagation of solar radiation. The findings reveal key aspects of atmospheric variability **(such as diurnal cycles, seasonal trends, and vertical C_n^2 profiles)**, supporting the assessment of Kolmogorov's turbulence theory, which is fundamental to refractive index calculations. Accurate refractive index modeling is essential for deploying adaptive optics systems.

This study **analyzes** a single ERA5 grid point aligned with the location of **OPD.** The observatory's area is roughly 1/20th of the spatial extent of an ERA5 grid cell, a mismatch that may lead to biases from ERA5's coarse resolution (Figure 1). These biases are particularly relevant for variables affected by orographic features, such as low cloud cover and wind speed.

Although some limitations remain, we selected ERA5 due to its capability to provide continuous vertical profiles in data-sparse regions, particularly where radiosondes or other similar profiling systems are not available. Therefore, our validation was confined to single-level comparisons of 2m temperature, dew-point temperature, and 10m wind speed, the accuracy of the full atmospheric column cannot be conclusively guaranteed, and profile-derived inferences should therefore be treated with appropriate circumspection.

5. ATMOSPHERIC CONDITIONS **AT** THE PICO DOS DIAS OBSERVATORY

5.1. *Comparison of ERA5* ***and*** *Ground-Based observations*

In situ measurements from weather stations serve as a benchmark for validating the dataset by comparing observational data with ERA5 single level reanalysis data.

Figure 2 displays scatter plots that compare ERA5 reanalysis data with measurements from a meteorological station for three key variables: air temperature, dew point temperature, and wind speed. These variables are analyzed separately for daytime and nighttime conditions, enabling a deeper understanding of their behavior across different observational regimes. In each plot, the dashed black line represents the relationship between ERA5 values and station observations, providing a visual reference for their agreement between the two datasets. The OPD, historically focused on night-time astronomical observations with its array of telescopes, is preparing to integrate solar studies through the addition of its first dedicated solar observation instrument, the spectropolarimeter, under the GSST project. To ensure the study remains relevant to both the current nighttime instruments and the forthcoming solar telescope, the **analysis distinguishes** between daytime (06:00–18:00 local time, UTC-3) and nighttime (18:00–06:00 local time, UTC-3) datasets. This separation provides a clear framework for interpreting results under these two distinct observational periods.

Regarding the Pearson correlation coefficient of the 2-meter air temperature (T2m) between ERA5 and the weather station, a high correlation is observed, with values of 0.85 during the daytime and 0.82 during nightime. This indicates a strong linear relationship between the two datasets, suggesting that ERA5 accurately captures the temporal patterns and relative variations in T2m.

However, ERA5 tends to overestimate temperatures, showing a bias of 3.86°C during daytime and 2.23°C during nighttime, with a more pronounced bias during the day. The MSE and RMSE metrics reflect the magnitude of the errors, and for T2m, they show RMSE values of 4.49°C during daytime and 2.94°C during nighttime. **These error magnitudes are consistent with previous ERA5 validation studies in complex terrain environments (E. Dutra et al. 2020; M. Nogueira et al. 2021) and remain within acceptable bounds for atmospheric turbulence studies (E. Masciadri et al. 2013; C. Giordano et al. 2013).**

Overall, despite the systematic biases, ERA5 demonstrates adequate performance for characterizing atmospheric turbulence at OPD. The 24-year analysis reveals that ERA5 successfully captures T2m temporal trends and variability patterns, with slightly larger discrepancies during daytime due to the challenges of modeling enhanced convective processes and boundary layer dynamics during solar heating periods. **This behavior is well-documented in the literature, where reanalysis models typically show increased uncertainty during unstable atmospheric conditions due to the complexity of representing small-scale convective processes (P. C. Kalverla et al. 2019; J. Olauson 2018; M. García-Díez et al. 2015).**

Regarding the dew point temperature (DPT), the correlation between ERA5 and the weather station is 0.86 both during the day and during nighttime, values that are relatively higher than those observed for T2m. Furthermore, MSE and RMSE metrics show lower values compared to T2m, with 4.41°C and 2.10°C during daytime, and 6.42°C

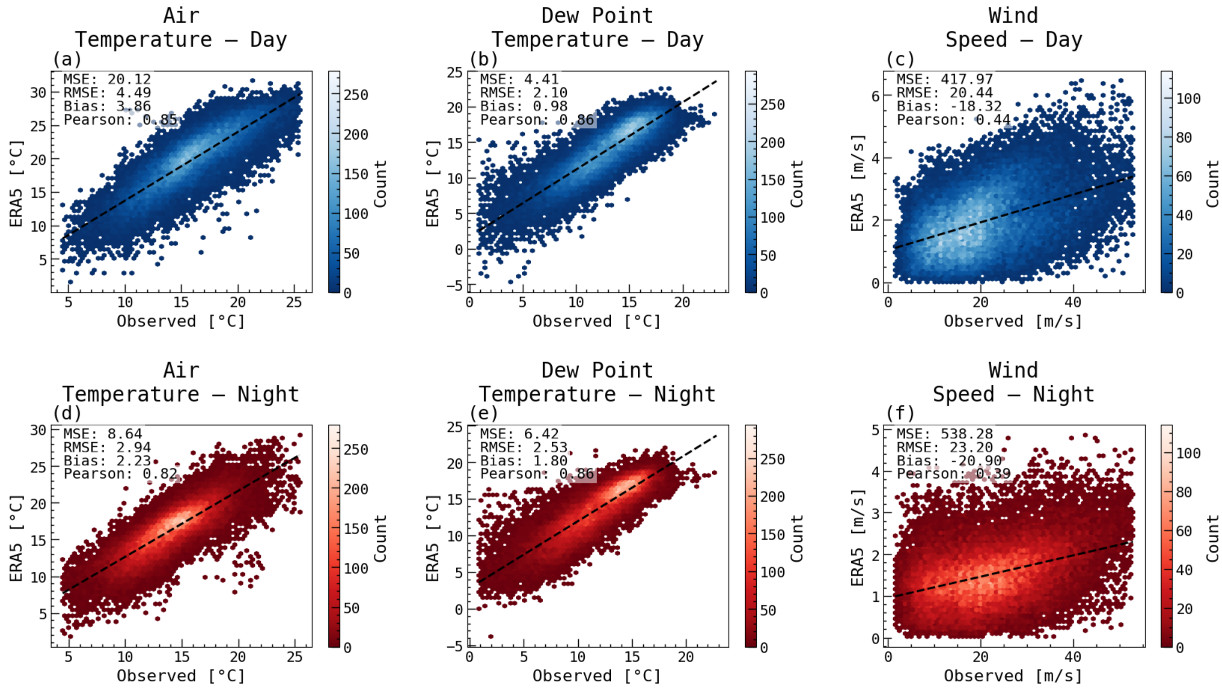

Figure 2. Density-scatter comparison of ERA5 reanalysis against in situ observations for air temperature, dew point temperature, and wind speed. Panels (a–c) show daytime results and (d–f) nighttime results. Each hexagonal bin is shaded by the number of paired observations (colorbar: Count), with darker tones indicating higher density. The dashed black line in each panel denotes the 1:1 reference. Annotated statistics include mean squared error (MSE), root mean square error (RMSE), bias (ERA5–observed) and Pearson correlation coefficient. Observed values are plotted on the horizontal axis and ERA5 values on the vertical axis; units are °C for temperature and dew point, and m/s for wind speed. Outliers beyond the insitu interquartile range were removed prior to analysis. (1999–2023 period).

and 2.53°C during nighttime, respectively. This is consistent with the bias values, which were low, at 0.98°C during daytime and 1.80°C during nighttime.

The **DPT** is a crucial factor in astronomical observations, as it directly affects the quality of the collected data. An elevated dew point can lead to water condensation on telescopes and sensors, degrading the captured images and damaging electronic components (A. Radu et al. 2012). Additionally, it can introduce interference in measurements, impacting data accuracy (J. Thomas-Osip et al. 2007). This phenomenon is particularly critical in infrared wavelength observations, where atmospheric humidity can distort images and reduce the efficiency of telescopes (A. Otárola et al. 2010). Previous studies on atmospheric water vapor in optical observatories have shown that lower dew point values enhance near-infrared observations by reducing water vapor absorption and emission (S.-H. Lee et al. 2007; M. M. Colavita et al. 2004). Therefore, understanding the dew point temperature is essential to maintain equipment functionality and optimize observation time in astronomical observatories.

In contrast, the correlation for wind speed is weaker, with Pearson values of 0.44 during daytime and 0.39 during nighttime. During the day, the MSE and RMSE values are 417.97 m/s and 20.44 m/s, respectively, while at night they are 538.28 m/s and 23.20 m/s, respectively. This result is consistent with the higher data dispersion between ERA5 and the weather station, as shown in the third column of Figure 2. Furthermore, ERA5 underestimates wind speed by -18.32 m/s during daytime and -20.90 m/s during nighttime. However, these results are consistent with previous studies, which indicate that in regions with complex and rugged topography, ERA5 has difficulties accurately representing wind values, leading to overestimations and underestimations (G. Gualtieri 2021; L. Minola et al. 2024; C. Gutiérrez et al. 2024). **ERA5 wind speed errors decrease at middle altitudes (1–4 km), with improved agreement with radar profiles (C. Suo et al. 2024)**. It is important to note that ERA5 performs better in areas with flat terrain or little variation. However, ERA5's underestimation of wind speed can have negative implications for the analysis of observational data that is sensitive to wind speed accuracy.

The variables T2m, DPT, and wind speed are fundamental factors that determine the quality of astronomical observations, as they notably influence the stability and clarity of the sky. T2m impacts the thermal environment around telescopes, potentially affecting sensor performance and introducing noise into astronomical observations. According to F. Lascaux et al. (2013), high daytime temperatures often induce atmospheric turbulence, thereby degrading optical seeing quality.

On the other hand, DPT is directly related to the atmospheric water vapor content, which plays a crucial role in absorbing and scattering electromagnetic radiation, particularly in the infrared and microwave bands. It is possible for high relative humidity levels near the dew point to cause condensation on optical components, thus affecting the quality of astronomical observations. The high correlation observed in DPT values between ERA5 and in situ measurements suggests that ERA5 is a valuable tool for assessing atmospheric conditions that impact astronomical observations, **especially in locations where observational datasets are not available.**

Wind speed plays a critical role in the performance of telescopes, as it directly affects their ability to maintain the desired pointing stability and accurately track cosmic sources, such as the Sun. In particular, high wind speeds can introduce vibrations and tracking errors, posing significant challenges for large-aperture telescopes. Near the surface, understanding wind characteristics is vital to ensure the proper installation of a telescope. This requires the use of meteorological towers tall enough to measure wind speed and direction at different heights or, alternatively, the deployment of radiosondes to obtain vertical wind profiles. Typically, the wind speed decreases near the surface due to energy loss caused by friction with the roughness of the terrain. However, in mountainous regions like the **OPD**, katabatic winds (cold air masses descending along slopes) and anabatic winds (warm air masses rising during daytime) can create intense wind flows under certain conditions. These phenomena can impact telescope performance by affecting the stability of observations and the quality of the collected data.

Strong wind speeds amplify turbulence in the planetary boundary layer, degrading the seeing conditions for optical and infrared observations (Y. Tillayev et al. 2023). The low correlation values observed for this variable highlight the limitations in the reliability of ERA5 for applications requiring high precision. For instance, low wind speeds (< 3.3 m/s) can lead to thermal stagnation and poor seeing, while excessive winds (> 10 m/s) induce vibrations in telescopes, which negatively affect the quality of astronomical observations (G. Lombardi et al. 2008; C. Giordano et al. 2014).

The wind rose analysis in Figure 3 illustrates the prevailing wind direction and speed during the daytime and nighttime throughout the four seasons. In DJF, daytime winds are predominantly from the north (N) at 33% of the time, with south-southeast (S–SE) winds contributing 10%. In this analysis ERA 5 Wind speeds typically range from 1.0 to 4.0 m/s, categorized into three color-coded intervals: 1.0–2.0 m/s (green), 2.0–3.0 m/s (yellow), and 3.0–4.0 m/s (orange). At night, northerly winds decrease slightly to 27%, while S–SE winds increase, ranging between 7% and 33%. In MAM, daytime winds remain similar to DJF, with northerly winds at 33% and S–SE winds rising to 27%. At night, S–SE winds dominate (up to 33%), while wind speeds mostly fall between 1.0 and 3.0 m/s.

In JJA, daytime winds are dominated by northerly directions (33%), with north-northeasterly (N–NE) winds appearing at frequencies below 20% and S–SE winds under 20%. At night, northerly winds decrease to 27%, while S–SE winds increase significantly (13–33%). Wind speeds typically range from 1.0 to 3.0 m/s. In SON, daytime winds are again predominantly northerly (33%), with N–NE winds below 15% and S–SE winds around 20%. At night, northerly winds decrease to about 20%, while S–SE winds range from 13% to 33%. This season sees a notable increase in stronger winds (3.0–4.0 m/s), which occur more frequently than in other seasons.

In observational astronomy, the wind rose is used to study wind patterns directly affecting atmospheric seeing, a key parameter determining astronomical images' clarity. Research conducted at the Cerro Paranal Observatory in Chile has identified that optimal seeing conditions are associated with prevailing winds from the north, with moderate velocities ranging between 8 and 12 m/s (M. Sarazin et al. 2008).

The wind rose is particularly valuable for providing precise information about predominant wind directions, enabling the optimal alignment of antennas and predicting the most favorable periods for astronomical observations (A. Otarola et al. 2019). Additionally, a detailed analysis of wind patterns is crucial for effectively implementing **AO** systems, which correct real-time distortions caused by atmospheric turbulence (B. García-Lorenzo et al. 2011; G. Lombardi et al. 2009).

In summary, the wind patterns at **OPD** exhibit distinct seasonal and diurnal variations, driven by local topography and solar heating. Northerly winds dominate during the day in all seasons, while S-SE winds become more prominent at night. Wind speeds remain mostly between 1.0 and 4.0 m/s, with SON experiencing a higher frequency of stronger winds, reflecting characteristic circulation patterns shaped by the region's unique conditions. However, it was noted

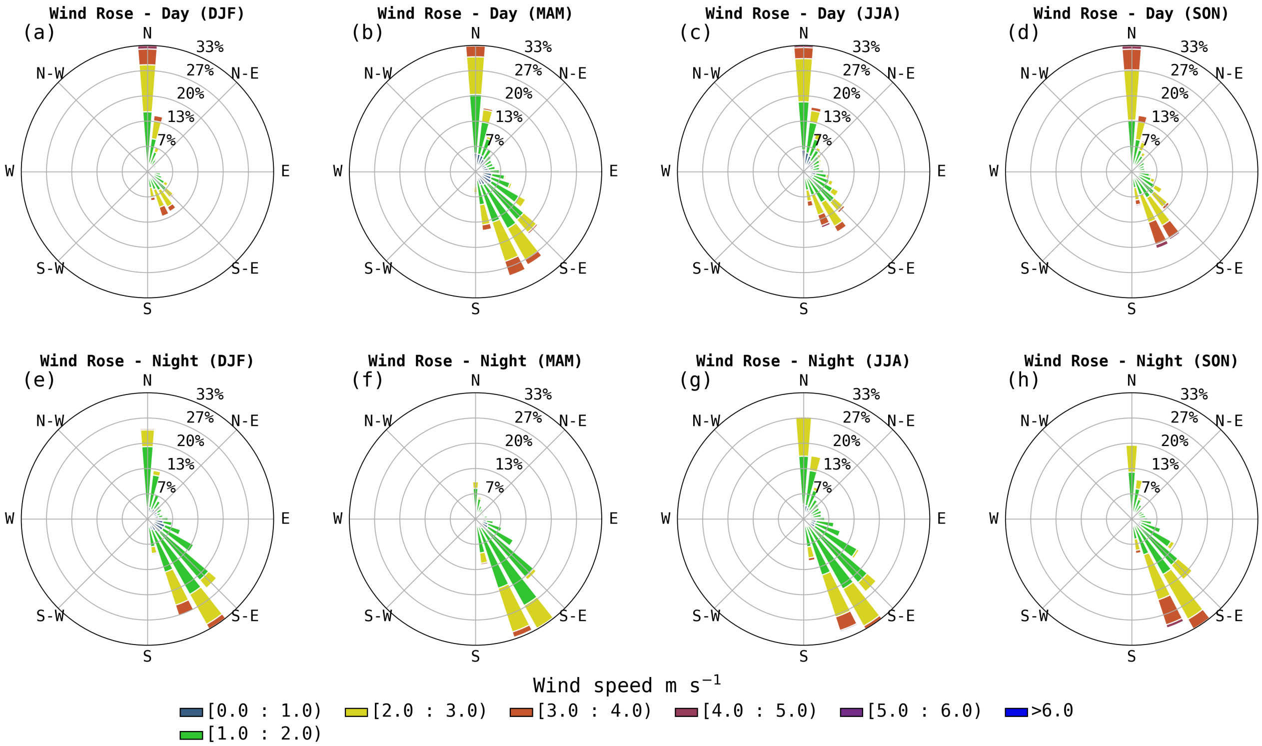

Figure 3. Wind rose diagrams showing wind direction and magnitude for different seasons (**DJF, MAM, JJA, and SON**) and times of day (day and night) (1999–2023 period).

that wind intensity data from the ERA5 model tends to underestimate near-surface wind speeds (See the third column of Figure 2). Therefore, these estimates should be interpreted with caution in the study area.

The magnitude of surface wind speed plays a crucial role in the performance and stability of astronomical telescopes, including radio telescopes. Both wind speed and temperature are key environmental factors that must be carefully considered during the planning, installation, and operation of large-aperture telescopes. High wind speeds can exert significant mechanical stress on the telescope structure, impacting its alignment and pointing accuracy. This effect is particularly pronounced in telescopes that are not shielded by a domed enclosure, where direct exposure to wind loading increases the risk of vibration or misalignment (A. Otarola et al. 2019; L. T. Maud et al. 2017; J. V. Silva et al. 2020; L. A. Bolbasova et al. 2023).

Figure 4 presents the diurnal and seasonal variability of **T2m**, **DPT**, and **wind speed** using bean plots across the four seasons and **for both daytime and nighttime periods**. The probability density distributions reveal distinct seasonal patterns and diurnal variations, with accompanying statistical summaries (percentiles, median, minimum, and maximum values) presented in tables below each panel. These variables are fundamental for characterizing sky quality, a critical factor for observational astronomy, particularly in the context of the Galileo Solar Space Telescope located at the **OPD**.

The Figure 4 a show the analysis of air temperature and reveals a well-defined seasonal cycle, characteristic of mid-latitude climates. During the DJF, daytime temperatures peak near 32 °C, while nighttime values persist relatively stable around 15 °C, reflecting a marked diurnal thermal gradient. On the other hand, the JJA season exhibits a broader thermal amplitude, with daytime temperatures fluctuating between 5 °C and 30 °C, and nighttime values between 0 °C and 25 °C. During the SON and MAM seasons show intermediate patterns, marked by an increase in temperature dispersion, which is a typical feature of atmospheric transition phases influenced by land-atmosphere coupling processes.

Figure 4b, which illustrates the dew point temperature (a key thermodynamic indicator of atmospheric moisture content) reveals greater stability throughout the diurnal cycle when compared to air temperature. This limited variability is primarily attributed to the thermal inertia of water vapor and its role in preserving hygrometric balance within the atmospheric boundary layer. In DJF the peak values typically ranging between 15 °C to 20 °C, while JJA measurements often fall below freezing (-10 °C during the day and -5 °C during the nigth) signaling the presence of cold, dry air masses.

Figure 4c show the behavior of the wind field, the frequency distribution display a notable day and night symmetry, with predominant speeds within the 0–4 m/s range in all seasons. However, during the MAM and JJA seasons, extreme wind events are observed, reaching up to 8 m/s. These events are likely associated with enhanced synoptic-scale activity, as these months typically experience intensified and more frequent frontal systems and low-pressure disturbances.

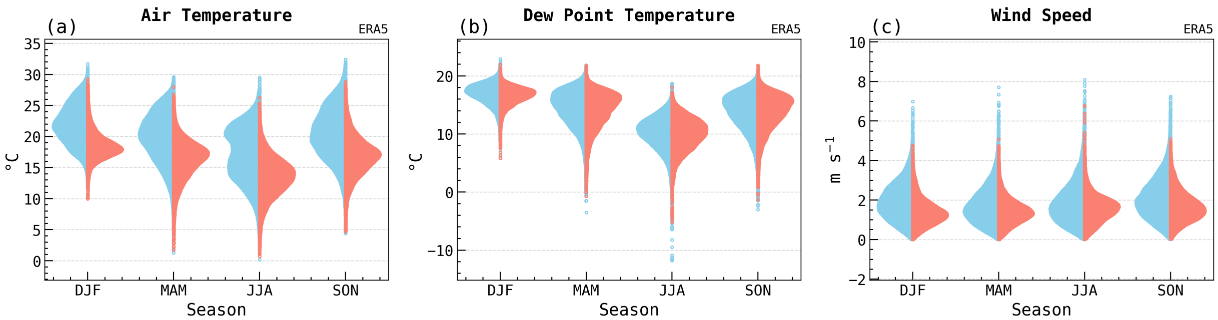

Season	Min	P10	P25	Med	P75	P90	Max
DJF	10.6	17.8	19.7	21.9	24.3	26.3	31.7
DJF	10.0	16.2	17.2	18.2	19.5	21.1	29.2
MAM	1.2	14.6	17.3	20.1	22.7	24.8	29.6
MAM	1.7	12.3	14.6	16.6	18.2	19.7	28.0
JJA	0.2	11.5	14.0	17.2	20.6	22.5	29.5
JJA	0.7	9.7	11.6	13.6	15.5	17.3	26.2
SON	4.4	15.4	17.7	20.5	23.5	25.9	32.4
SON	4.7	13.0	15.0	16.9	18.6	20.5	28.8

Season	Min	P10	P25	Med	P75	P90	Max
DJF	6.4	14.6	15.9	17.2	18.2	18.9	22.9
DJF	5.8	14.6	15.7	16.7	17.6	18.2	22.0
MAM	-3.5	10.3	12.5	14.9	16.7	18.0	21.8
MAM	-0.7	10.1	12.4	14.7	16.4	17.4	21.8
JJA	-11.8	6.4	8.4	10.4	12.0	13.4	18.7
JJA	-5.2	6.4	8.2	10.2	11.9	13.2	18.0
SON	-3.0	9.4	11.8	14.2	16.2	17.4	21.7
SON	-1.3	9.7	12.1	14.3	16.0	17.1	21.8

Season	Min	P10	P25	Med	P75	P90	Max
DJF	0.0	0.8	1.3	1.9	2.6	3.2	7.0
DJF	0.0	0.6	1.0	1.3	1.7	2.2	4.8
MAM	0.0	0.7	1.1	1.6	2.3	3.0	7.7
MAM	0.0	0.7	1.0	1.4	1.8	2.2	5.1
JJA	0.0	0.7	1.1	1.7	2.5	3.3	8.1
JJA	0.0	0.7	1.1	1.6	2.0	2.4	6.8
SON	0.0	0.9	1.4	2.0	2.7	3.5	7.2
SON	0.0	0.8	1.2	1.6	2.1	2.7	5.1

Day Night

Figure 4. Distribution of ERA5 (1999–2023) meteorological variables by season and diurnal period. Bean plots show the probability density distribution of (a) air temperature (°C), (b) dew point temperature (°C), and (c) wind speed (m s^{-1}) for day (light blue) and night (light red) periods across four seasons: DJF (December-January-February), MAM (March-April-May), JJA (June-July-August), and SON (September-October-November). The violin-shaped distributions display the data density, with scattered points representing individual observations. Tables below each panel present descriptive statistics including minimum (Min), 10th percentile (P10), 25th percentile (P25), median (Med), 75th percentile (P75), 90th percentile (P90), and maximum (Max) values for each season-period combination. Blue-shaded rows indicate daytime statistics, while red-shaded rows represent nighttime statistics.

5.2. *Vertical assessment of ERA5 atmospheric parameters*

Ensuring the quality of **astronomical** observations requires a thorough understanding of the behavior of key atmospheric variables throughout the vertical column of the atmosphere, which includes the troposphere and stratosphere. In this context, atmospheric temperature, wind speed, relative humidity and cloud cover **are** analyzed on hourly, monthly, and seasonal scales. **This analysis relies on ERA5 data from a single vertical atmospheric column. However, for telescope observations at elevations other than the zenith, the light path is oblique and may extend beyond the boundaries of the considered grid cell. At low elevations, it can traverse atmospheric regions whose properties are not represented in the analyzed column.**

To assess the validity range of this single-column approximation, we calculate the condition under which the horizontal displacement of the ray at a geometric height (h), given by:

$$\Delta r(h) = h \tan z, \tag{1}$$

where z is the zenith angle and $\varepsilon = 90^\circ - z$ is the elevation, does not exceed half of the grid cell width $\Delta x/2$. Using the OPD site as reference, where the horizontal resolution of ERA5 is $\Delta x \approx 31\,\mathrm{km}$, and

considering that most of the optical turbulence is concentrated below $h_{\max} = 18\,\mathrm{km}$ (lower stratosphere), the validity limit of the approximation is reached when

$$h_{\max} \cot \varepsilon_{\min} = \frac{\Delta x}{2}, \tag{2}$$

From this relation we obtain

$$\varepsilon_{\min} = \arctan\left(\frac{\Delta x}{2h_{\max}}\right), \tag{3}$$

which, using the values above, yields

$$\varepsilon_{\min} \approx 40.7^{\circ} \tag{4}$$

Therefore, the single column approximation is valid for observations performed at elevations higher than approximately 40° (zenith distances $z \lesssim 50^{\circ}$, air mass $\sec z \lesssim 1.56$). For observing programs that include lower elevations, a multi-column integration would be required to accurately model the atmospheric properties along the line of sight.

Figure 5 illustrates the hourly climatological behavior of air temperature as a function of pressure across the 37 vertical levels of ERA5 for the four seasons. During the DJF, at low altitudes (1000–800 hPa), the highest temperatures range from 15 to 25 °C between 10:00 and 16:00, while during the early morning hours (00:00–06:00), they decrease to values between 5 and 15 °C. At mid-altitudes (800–400 hPa), temperatures range from 10 to -10 ° C, with slight increases during the day. At high altitudes (400–1 hPa), extremely cold temperatures range from -40 to -70 °C, with minimal diurnal variation, representing a thermally stable upper layer. In MAM, at low altitudes, temperatures can reach up to 25 °C near midday and drop to between 10 and 15 °C during the early morning. At mid-altitudes, temperatures range from 13 to -20 °C, with a greater diurnal thermal amplitude compared to DJF, while at high altitudes, they remain below -40 °C, with slight increases during the day.

During the JJA, low altitudes exhibit predominantly cooler temperatures, ranging between 15 and 20 °C during the early morning hours and peaking at up to 25 °C between 12:00 and 16:00. At midaltitudes, the thermal range decreases between 10 and -20 °C, colder than in the previous seasons. At high altitudes, temperatures range from -20 to -80 °C, with slight daytime increases due to solar radiation. Finally, in SON, the thermal behavior at low altitudes is similar to that observed in DJF but with slightly lower intensities; the highest temperatures (up to 25 °C) occur between 10:00 and 16:00, while during the early morning hours (00:00–08:00), they range from 15 to 20 °C. At mid-altitudes, temperatures vary between 15 and -20 °C, with a reduced diurnal amplitude, and at high altitudes, they remain between -20 and -70 °C, with no significant changes throughout the day.

The Figure 6 illustrates the monthly climatology of the air temperature as a function of atmospheric pressure for daytime **panel** (a) and nighttime (b) conditions. During the day, it is observed that in the lower layers (1000-800 hPa), the air temperature exhibits higher values from September to April, exceeding 25 °C. In contrast, from May to August, the air temperature drops below 25 °C. This pattern aligns with expectations, as DJF and transitional months receive higher solar radiation, while JJA months experience significantly reduced solar input. In the mid-level atmosphere (800–400 hPa), the air temperature ranges between 15 °C and -18 °C, with the lowest values occurring during the JJA months. At higher altitudes (400-1 hPa), the air temperature fluctuates between -20 °C and -70 °C.

At night, the behavior of air temperature mirrors the pattern of the day, although maximum temperatures persist for shorter periods. In the lower layers (1000-800 hPa), the highest air temperature values are recorded between November and April, reaching approximately 25 °C, while temperatures fall below 20 °C from May to October. In midlevels (800-400 hPa), the air temperature ranges from 10 ° C to -20 ° C, with the highest variability observed between May and September. At higher altitudes (400-1 hPa), the temperature variations vary less throughout the year, with values ranging between -20 °C and -70 °C.

Both Figure 5 and Figure 6 exhibit the expected tropospheric lapse rate, with air temperature decreasing steadily with pressure from the surface up to the tropopause (∼100 – 50 hPa, or ∼11 – 20 km). Above this level, the trend reverses, and a weak warming is observed, attributable to ozone driven radiative heating in the lower stratosphere. This transition, evident at the upper boundary of the profiles, is completely consistent with the canonical vertical temperature structure of the atmosphere.

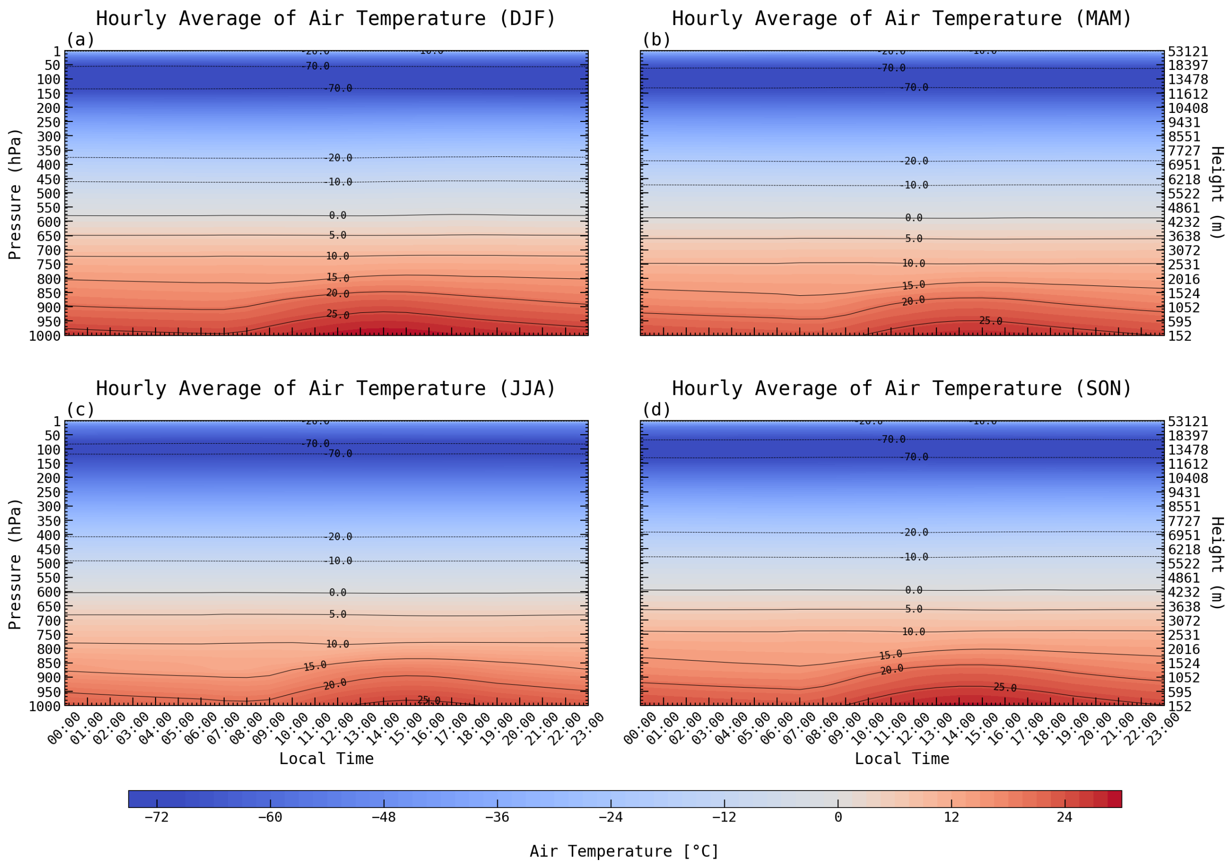

Figure 5. Hourly climatology of vertical profiles (1999–2023) of air temperature across different seasons (**panels with titles:** DJF, MAM, JJA, SON), showing variations with height on the **vertical axes** and time of **horizontal axes**.

Figure 7 illustrates the hourly wind speed patterns throughout the vertical atmospheric column available in ERA5 for the four seasons of the year. During all seasons, winds between 1000 and 850 hPa are weak, with speeds ranging from 0.4 to 3.0 m/s. These winds reach their relative maximum intensity between 09:00 and 16:00 hours, with speeds varying from 2 to 3 m/s.

In the DJF, winds between 850 and 350 hPa exhibit speeds ranging from 3 to 10 m/s. At higher altitudes, between 350 and 100 hPa, winds intensify, reaching speeds close to 20 m/s. Above 100 hPa, between 100 and 50 hPa, wind speeds decrease to approximately 7 m/s. During MAM, winds between 850 and 450 hPa show a similar pattern to that observed in DJF. However, above 400 hPa, winds intensify further, reaching speeds of up to 30 m/s between 250 and 150 hPa.

In JJA, winds exhibit a similar behavior to MAM between 850 and 450 hPa, with speeds varying from 7 to 10 m/s. Above 550 hPa, winds progressively intensify, exceeding 30 m/s between 300 and 150 hPa. In SON, winds between 850 and 550 hPa range from 3 to 10 m/s. Above 500 hPa, wind speeds increase, reaching up to 25 m/s between 250 and 150 hPa. It is important to highlight that a jet stream region is identified at high levels, located approximately between 300 and 150 hPa. This region varies in intensity and expands or contracts vertically, displaying similar characteristics throughout the four seasons. Additionally, above 850 hPa and below 400 hPa, there is little variation in wind intensity over the 24-hour period analyzed.

Between 1000 and 850 hPa, winds generally remain low due to friction but increase slightly during the day (from 09:00 to 16:00 hours) as heating promotes vertical mixing. Although large-scale circulations dominate wind speeds, in mountainous regions such as that of the **OPD**, friction and thermal convection influence both the intensity and direction of near-surface winds. While observatories located above the turbulent boundary layer, such as those on Mauna Kea **in Hawaii**, avoid some surface wind effects, they still must contend with high-altitude turbulence caused

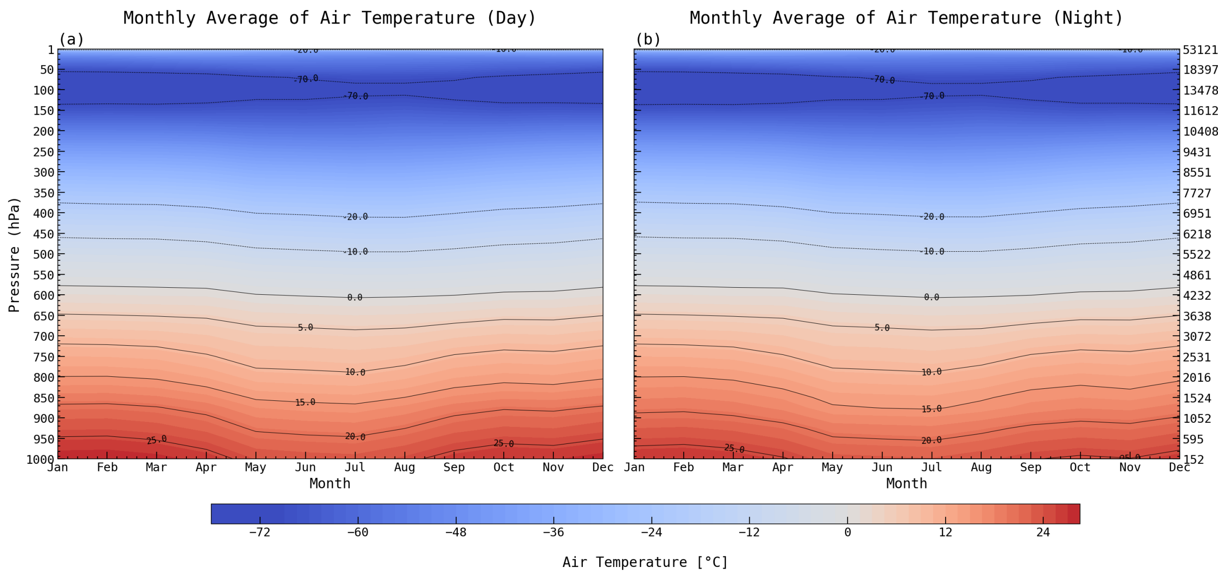

Figure 6. Monthly climatology of vertical air temperature (1999–2023) from ERA5, differentiated into a) daytime and b) nighttime.

by jet streams (R. Racine & B. L. Ellerbroek 1995; D. A. Erasmus & L. A. Thompson 1986; N. C. Sharma & J. E. Barnes 2016).

To better understand atmospheric processes at different vertical levels, the atmosphere is divided into layers relevant for astronomical observations. A widely accepted classification distinguishes two primary regimes: the atmospheric boundary layer (ABL), which extends approximately up to 1–2 km in altitude, and the free atmosphere, located above this level. The ABL is directly influenced by interactions between the Earth's surface and the atmosphere, such as friction, diurnal heating, and turbulent mixing processes. In contrast, the free atmosphere, situated above the ABL, experiences minimal surface influence and exhibits greater dynamic stability. In this region, turbulent flows are generally negligible, except in areas affected by wind shear instabilities, breaking gravity waves, or inertial instabilities (A. Dörnbrack et al. 2022).

Atmospheric turbulence caused by strong winds can significantly degrade astronomical seeing. Conversely, laminar flow conditions create optimal seeing environments. The intensity and variability of this turbulence are influenced by factors such as wind speed and direction, local topography, and the surrounding environment (S. S. Ningombam et al. 2017).

At lower altitudes, temperatures fluctuate more significantly due to the daily solar cycle. In contrast, higher altitudes tend to be more thermally stable due to reduced solar penetration and more efficient radiative cooling, which dampens temperature swings. These vertical temperature gradients contribute to atmospheric turbulence, especially during transitions from day to night (T. Travouillon et al. 2003; B. Ma et al. 2020). While daytime conditions near the surface usually promote stronger turbulence, the cooling of lower layers during the night leads to a more stable atmosphere with reduced turbulence, thereby providing conditions favorable for astronomical observations under dark, cloud-free skies.

Strong jet streams at higher altitudes, most pronounced in JJA due to larger equator-to-pole temperature gradients, can induce turbulence that negatively impacts observations. During the day, near-surface winds increase slightly as a result of solar heating, and the region around the jet stream, typically at around 200 hPa (Figure 7), becomes more turbulent, exacerbating distortions in solar imaging and spectroscopy. At night, as the atmosphere cools and stabilizes, lower-level turbulence subsides, improving clarity, but the persistent jet stream remains a challenge for high-resolution observations. In JJA, stronger temperature gradients intensify the jet stream, while in DJF, these gradients weaken, reducing high-altitude wind speeds and turbulence. Ultimately, variations in solar heating and seasonal temperature gradients shape the vertical structure of atmospheric winds, significantly influencing the quality of ground-based solar observations throughout the day and night (N. C. Sharma & J. E. Barnes 2016; R. Racine & B. L. Ellerbroek 1995).

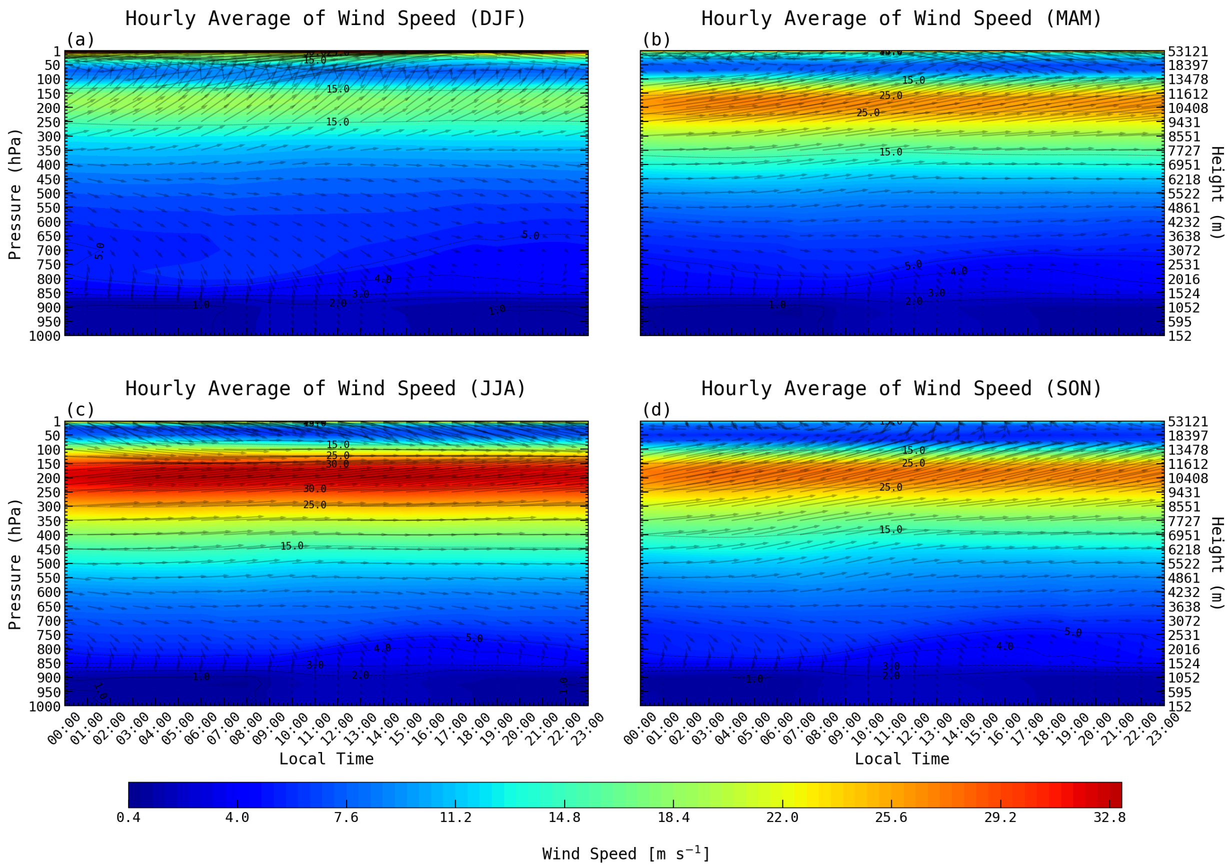

Figure 7. Hourly climatology of vertical wind speed and wind direction (1999–2023) from ERA5 across different seasons (DJF, MAM, JJA, SON), showing variations with height (pressure) and time of day.

Figure 8 depicts the hourly behavior of relative humidity (RH) across different pressure levels available in ERA5 for the four seasons. During DJF, RH exhibits high values (>80%) between the 950 and 700 hPa levels, with the highest concentration of RH located above 850 hPa between 08:00 and 18:00 hours. This is associated with the presence of solar radiation during this period. In the MAM season, the highest RH concentration follows a pattern similar to that observed in DJF. However, the band of highest concentration (>80%) is thinner, generally located between the levels of 900 and 800 hPa.

During the **dry** JJA season, the band of highest RH concentration is located between 1000 and 800 hPa, with concentrations below 70% between 00:00 and 10:00 hours. After this period, RH concentrations decrease to values below 60%. In SON, the band of highest RH concentration begins to expand due to the onset of the rainy season, showing a pattern similar to that observed in DJF. However, it presents a narrower vertical extent, with values below 80% and located between the 950 and 850 hPa levels. In all seasons, above the upper part of the band of highest RH concentration, the values gradually decrease until reaching their minimum (approximately 0%) at the highest levels of the atmosphere (1 hPa). Monitoring air temperature and relative humidity is crucial not just for understanding climatic conditions but also for operating telescopes and implementing specific control systems. Components such as detectors and filters are affected by operating temperature. **Large optomechanical components without active thermal control (such as primary and secondary mirrors, corrector plates, spider vanes, and structural trusses) respond directly to environmental changes; temperature gradients of $\gtrsim 1$ K can induce mirror seeing, focus drift, and astigmatism, while high RH promotes condensation and degrades reflective and anti-reflective coatings (L. Noethe 2002). In contrast, modern imaging detectors and interference filters usually employ closed-loop thermal regulation and are consequently far less sensitive to ambient fluctuations.**

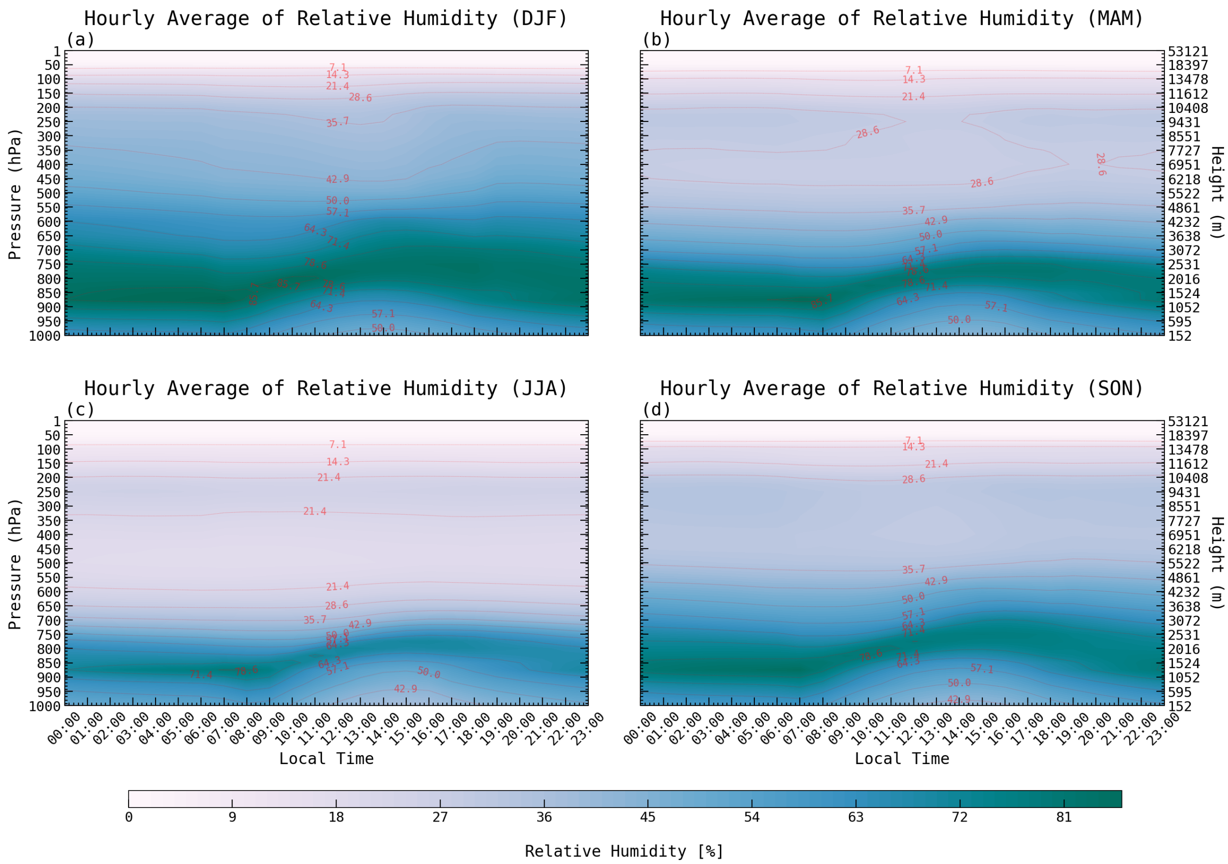

Figure 8. Hourly climatology of vertical relative humidity (1999–2023) from ERA5 across different seasons (DJF, MAM, JJA, SON), showing variations with height (pressure) and time of day.

High relative humidity can lead **to** water condensation, which can **degrade** observations **by affecting detectors**, electronic equipment, and **optical performance** (e.g., decrease the reflectance of mirrors). To prevent the formation of dew, it is important to set relative humidity thresholds. Some instruments **interrupt** observations when humidity reaches 90% as a precaution. More conservative limits may also be used, depending on local conditions. Also, to avoid water condensation, it is essential to monitor relative humidity and the dew point, particularly when the instruments are maintained at lower temperatures than the air. **A common condensation safety criterion flags any interval in which the ambient dew-point temperature difference, $\Delta T \equiv T - T_{\mathrm{d}}$, falls below $2°\mathrm{C}$ (within the broader 1 to $5°\mathrm{C}$ range discussed by G. Lombardi et al. 2008), observations should remain suspended until $\Delta T \geq 2°\mathrm{C}$ is restored.**

Cloud cover can affect astronomical observations, motivating the analysis of its diurnal and seasonal variability. Following the ECMWF ERA5 classification (H. Hersbach et al. 2020), clouds are categorized by altitude: low-cloud cover (LCC, $h < 2\,\mathrm{km}$), medium-cloud cover (MCC, $2 \leq h < 7\,\mathrm{km}$), and high-cloud cover (HCC, $h \geq 7\,\mathrm{km}$), with total cloud cover (TCC) representing the integrated fractional cloudiness across all levels. Figure 9 presents the climatological distribution of cloud cover by type for the 1999–2023 period.

Panel (a) shows the variation in cloud cover over the course of a day. Low clouds exhibit minimal coverage between 12:00 and 22:00, with percentages ranging from 5% to 60%. However, during the nighttime and early morning hours (23:00 to 11:00), the variability increases, spanning from 5% to 100%. Medium clouds peak in coverage during the late morning and evening hours (11:00 to 23:00), ranging between 0% and 60%, while showing reduced coverage from 00:00 to 10:00 (0% to 35%). High clouds display relatively consistent coverage throughout the day, with their highest presence observed during the afternoon to early morning period (15:00 to 07:00), ranging from 0% to 90%. In contrast, lower concentrations of high clouds are observed between 08:00 and 14:00, with values ranging from 0% to 60%. In panel (b), we examine the monthly distribution of cloud cover. Low clouds are most prevalent from September to May, with coverage ranging from 0% to 80%, while the lowest concentrations occur during the JJA months, with values between 0% and 50%. Specifically, August exhibits the lowest low-cloud coverage. Medium clouds reach their maximum concentration between October and March (5% to 70%), with reduced coverage observed from April to September (0% to 35%). High clouds show similar trends, with higher concentrations from October to March (0% to 100%), while during April to September they show reduced coverage, varying between 0% and 60%, and reaching values as low as 20% in August.

This analysis highlights that months with higher precipitation also correlate with increased cloud cover. However, it is important to acknowledge that the **OPD**, situated in a mountainous region, may experience localized orographic influences, which could cause ERA5 to overestimate **LCC** in certain instances, as depicted in Figure 2. Furthermore, Figure 9 highlights that optimal conditions for astronomical observations are typically during specific hours (09:00 to 22:00) and in the JJA months, when cloud cover is generally lower.

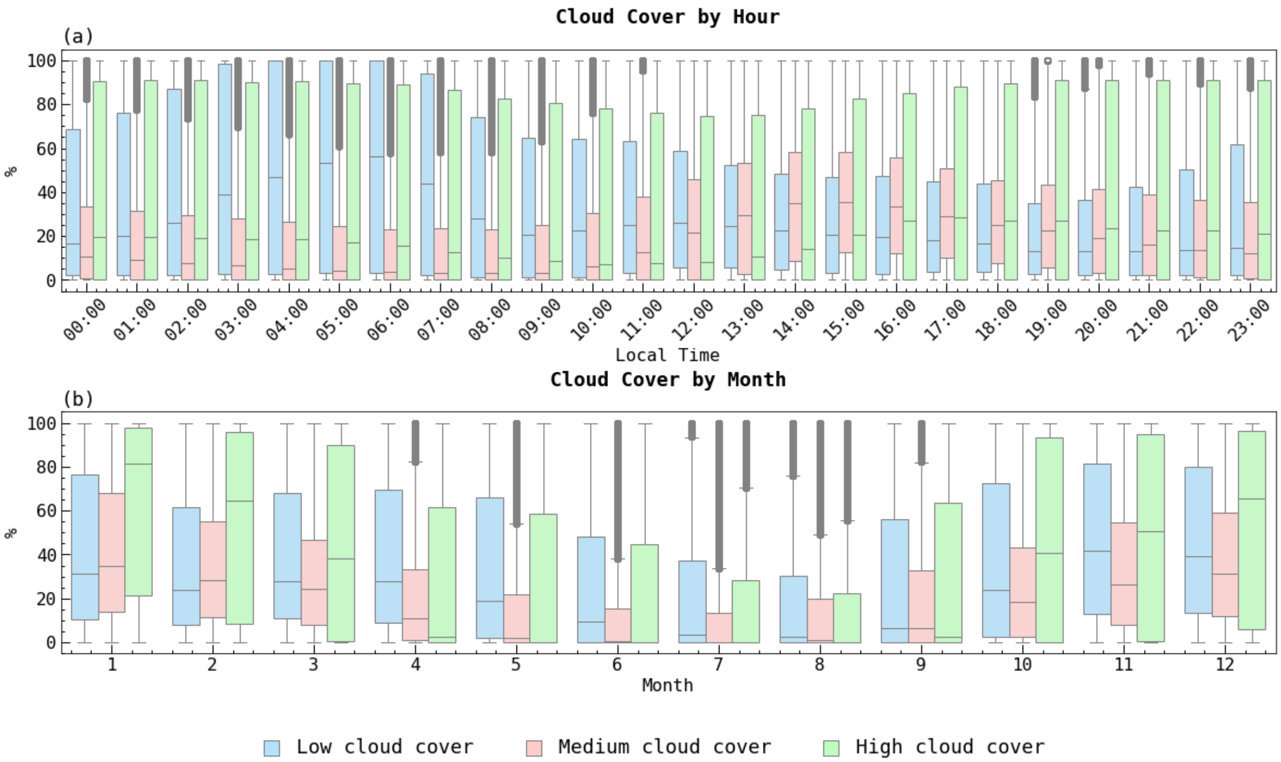

Figure 9. Climatological variations in cloud cover (1999-2023) across (a) hourly and (b) monthly timescales. The data is categorized into low, medium, and high cloud cover fractions.

Cloud cover dynamics is critical for understanding and optimizing astronomical observations, particularly for solar studies (J. Bergman 1997; D. Arbeláez-Cardona et al. 2020; Y. Lei et al. 2020; Q. Ye 2010). **LCC** affects visible observations by scattering visible and infrared radiation, leading to reduced contrast and reduced signal quality for solar instruments (J. Bergman 1997). **HCC** affects the infrared and microwave regimes; thin cirrus clouds, although often transparent to visible light, attenuate infrared signals and can interfere with all-sky surveys and certain spectroscopy tasks (M. Musiolková et al. 2021). Variations in cloud cover exhibit cyclical patterns throughout the day, with significant coverage in both high and low cloud layers. **LCC** often peak during the early morning and late evening, potentially due to temperature inversions or radiative cooling at night, while high clouds tend to be more evenly distributed but may vary due to daily convection or large-scale weather systems. The patterns shown in Figure 9, emphasize the need for temporal and spatial analyses of cloud cover to optimize observational planning.

To effectively assess and optimize observational quality, specific thresholds must be applied for categorizing cloud cover conditions. For instance, clear-sky periods are defined as intervals where cloud cover is below 25% for at least six consecutive hours (D. Mandat et al. 2014). This criterion ensures that the sky remains sufficiently clear to support high-quality astronomical imaging. In contrast, partially cloudy conditions are characterized by cloud cover between 25% and 65%. While such conditions may still allow for observational activities, higher levels of cloudiness are generally unsuitable for high-precision spectroscopic or imaging work.

Clear-sky periods are defined as intervals where TCC remains below 10% for at least six consecutive hours (J. Tian et al. 2016). This stringent criterion ensures optimal atmospheric transparency and minimal extinction, providing excellent conditions for high-precision astronomical imaging and photometry. In our case, following the same criterion of J. Tian et al. (2016), partially cloudy conditions (defined by TCC between 10% and 65%) represent intermediate atmospheric states. While not ideal for the demanding observations. These threshold definitions provide an understanding for observation scheduling and site characterization, enabling astronomers to match observational requirements with appropriate atmospheric conditions.

Applying the same cloud coverage thresholds to the complete 25-year dataset reveals seasonal and diurnal patterns in observational opportunities (Table 2). The analysis offers that JJA provides the favorable conditions for daytime solar observations, with 6560 clear hours compared to only 186 hours during DJF. Conversely, nighttime observations show a more balanced seasonal distribution, with MAM providing the highest number of clear hours (2142), followed closely by SON (1682 hours) and DJF (1681). Although JJA is favorable for daytime solar observations, it offers fewer nighttime opportunities (1595 clear hours).

The overall statistics indicate that 52% of daytime hours (10,106 out of 19,820) satisfy the stringent clear-sky criterion, whereas nighttime achieves 39% (7,100 out of 17,978). The higher daytime fraction reflects enhanced atmospheric stability during the JJA dry season, when reduced convective activity and minimal precipitation create optimal conditions for ground-based solar observations. These results have direct implications for the GSST operational strategy, suggesting that high-priority solar observations should be concentrated in the May–August window, while nighttime programs can be scheduled more evenly throughout the year. The data further support the feasibility of spectroscopic programs under partially cloudy conditions, which account for 49% of daytime hours and 61% of nighttime hours, thereby offering substantial opportunities for studies of atmospheric and stellar composition. A more detailed presentation of cloud-cover statistics is provided in Appendix A of this work.

Table 2. Seasonal distribution of clear and cloudy sky conditions for daytime (06:00–18:00) and nighttime (18:00–06:00) periods at OPD from 1999–2023. Clear conditions are defined as total cloud cover ≤10% for at least 6 consecutive hours; cloudy conditions as 10–65% cloud cover. Values represent total hours for each season across the 25-year period.

	Daytime		Nighttime	
Season	Clear	Cloudy	Clear	Cloudy
DJF	186	134	1681	2045
MAM	1620	1549	2142	3550
JJA	6560	6647	1595	2832
SON	1740	1384	1682	2451
Average	2526	2428	1775	2719
Total	10106	9714	7100	10878

In addition, to assess how temperature, wind, and dew point propagate throughout the vertical column and to quantify uncertainties in meteorological variables due to ERA5 data limitations, we performed 1000-member Monte Carlo simulations. Because direct observational profiles are not available at OPD, the simulations used the mean and standard deviation of ERA5 data at each pressure level, diurnal period, and season to estimate potential uncertainties. Each realization perturbed the ERA5 air temperature, dew point temperature, and wind speed profiles with Gaussian errors scaled to match observed surface discrepancies, and the resulting uncertainty estimates were aggregated by atmospheric layer: troposphere (200–1000 hPa), stratosphere (2–200 hPa), and mesosphere (1–2 hPa). As shown in Table 3, the propagated uncertainties reveal variability across atmospheric layers and seasons. Temperature uncertainties are highest in the troposphere, particularly during JJA (117.94±378.46% daytime), reflecting the challenging nature of temperature retrievals during JJA dry season when thermal stratification is most pronounced. Stratospheric temperature uncertainties remain more moderate

(10.58–12.65%), while mesospheric values show intermediate levels (54.74–66.31%).Dewpoint t emperature uncertainties shows extreme seasonal dependence, with SON showing exceptional propagated errors in the troposphere (782.17±3455.77% daytime), indicating the compounding effect of humidity retrieval uncertainties during transitional seasons. Wind speed uncertainties demonstrate more uniform behavior across the vertical column, typically ranging from 75–110% across all layers and seasons.

	Daytime			Nighttime		
Variable/Season	Troposphere	Stratosphere	Mesosphere	Troposphere	Stratosphere	Mesosphere
Temperature Uncertainty (%)						
DJF	32.23±37.71	10.58±8.95	61.26±6.87	31.20±37.28	10.55±8.76	58.81±0.12
MAM	52.42±85.63	11.67±8.67	60.76±9.96	48.51±71.59	12.08±9.11	56.08±9.10
JJA	117.94±378.46	12.47±9.14	57.10±2.60	106.94±325.03	12.00±8.15	54.74±3.49
SON	84.34±235.99	12.65±10.25	66.31±2.86	79.62±213.47	12.33±9.35	60.35±3.40
Dewpoint Uncertainty (%)						
DJF	76.52±144.34	6.51±4.36	22.68±1.14	67.88±111.08	6.48±3.95	21.27±0.33
MAM	99.46±175.28	7.15±4.70	22.66±0.38	104.41±211.09	7.26±4.83	22.63±0.33
JJA	112.66±201.03	7.56±5.11	23.07±3.07	115.85±233.87	7.34±4.64	23.02±1.84
SON	782.17±3455.77	7.42±4.80	21.74±0.81	889.77±3961.11	7.37±4.79	20.12±1.32
Wind Speed Uncertainty (%)						
DJF	102.99±7.41	77.94±17.36	53.02±3.15	102.86±5.86	75.47±18.46	56.99±10.56
MAM	104.52±6.31	102.98±5.00	110.16±0.79	104.46±7.92	103.74±5.21	107.19±5.15
JJA	100.59±10.58	93.15±17.23	110.06±3.85	97.68±11.04	94.21±17.84	111.86±0.01
SON	97.76±8.55	98.81±14.26	108.53±1.00	97.37±8.75	99.46±15.04	107.80±0.02

Table 3. Layer-wise percentage uncertainty (mean ± SD) of temperature, dewpoint, and wind speed by season and diurnal period. Daytime and Nighttime blocks list DJF, MAM, JJA, and SON. Percentage uncertainty is defined as $100 \times \frac{\text{upper}-\text{lower}}{2|\text{orig\_mean}|}$, where "upper" and "lower" are 95% Monte-Carlo (1000 samples) confidence bounds at each pressure level; values are averaged within each atmospheric layer (Troposphere ≥300 hPa, Stratosphere 10–300 hPa, Mesosphere 1–10 hPa).

The preservation of variability patterns in ERA5 data ensures that the turbulence characteristics essential for C_n^2 calculations are accurately represented, consistent with previous validation studies of reanalysis data for atmospheric optics applications (A. Shikhovtsev et al. 2019; C. Qing et al. 2016).

6. ATMOSPHERIC REFRACTIVE INDEX

6.1. *Seasonal Characteristics of Atmospheric Turbulence* ***in Astronomical Observations***

Atmospheric turbulence is a critical phenomenon in terrestrial astronomy, arising from variations in atmospheric temperature, wind speed and pressure that cause fluctuations in the refractive index (J. d. D. Sanchez-López et al. 2011). These fluctuations are primarily driven by the heating of air masses near the Earth's surface, which, in combination with dynamic forces such as convection and wind, generate turbulence. Air masses with different temperatures and pressures exhibit varying refractive index values, leading to distortions in the path of light rays and degrading the quality of images captured by ground-based telescopes. Turbulent motion is characterized by a high Reynolds number and involves random secondary flows known as eddies. According to Kolmogorov's theory, these eddies undergo a cascade process, fragmenting into progressively smaller eddies until their energy dissipates due to viscosity. Kolmogorov's turbulence model assumes homogeneity and isotropy, positing that the energy spectrum depends only on the separation between two points in the turbulent layer. Energy in turbulence originates from large-scale processes such as wind shear or convection (Y. D. Dwivedi et al. 2021). In the cascade process, larger eddies of size L_0(outer scale) break into smaller eddies, transferring energy down to the microscale l_0(inner scale), where dissipation occurs. Within the inertial subrange spanning eddy sizes between l_0 and L_0, fluctuations in the refractive index are significant. At scales smaller than l_0, viscous dissipation converts turbulent energy into heat.

The spectrum of turbulent flows encompasses a wide range of spatial and temporal scales. Observations in the free atmosphere reveal that energy spectra of synoptic-scale temperature and wind velocity inhomogeneities follow E(f) $\propto f^{-3}$ for scales ranging from 2500 km to 800 km. In the mesoscale range (< 600 km), spectra exhibit a power-law behavior $E(f) \propto f^{-5/3}$, consistent with the Kolmogorov-Obukhov theory (A. N. Kolmogorov et al. 1991; A.

Shikhovtsev et al. 2019). In the micrometeorological range, both $E(f) \propto f^{-3}$ and $E(f) \propto f^{-5/3}$ power laws are observed, depending on the scale. Turbulence significantly impacts the performance of ground-based telescopes by distorting the wavefront of incoming light. Even small variations in atmospheric temperature ($0.1 - 1^{\circ}$ C) correspond to minute deviations in the refractive index, sufficient to degrade optical resolution (J. W. Hardy 1998).

Geographic factors also influence turbulence strength, with mountain summits being preferred for observatories due to lower turbulence levels. However, windward locations often face severe turbulence caused by wind-driven disturbances over mountain terrain, compounded by daytime surface heating, which generates convection currents that contribute to turbulent flow (J. Schmidli 2013; P. Bekhrad et al. 2023). The refractive index structure parameter, C_n^2, is commonly used to quantify turbulence strength (A. Shikhovtsev et al. 2019; A. Y. Shikhovtsev & P. G. Kovadlo 2024). It depends on altitude and spatial frequency, and its mathematical representation is given as:

$$C_n^2(z) = \left(\frac{AP(z)}{< T >^2 (z)}\right)^2 \cdot \frac{E(f_L, z)\, exp\left\{-3\left(ln\, \frac{f_t}{f_L}\right) - \frac{5}{3}\left(ln\, \frac{f_l}{f_t}\right)\right\}}{0.125} f_l^{\frac{5}{3}}, \tag{5}$$

where f_L; f_l **are** the frequencies in the **high and low** spatial frequency **rages, respectively**; f_t is the spatial frequency in the transient spectral region (from -3 to $-\frac{5}{3}$); while A is defined as 80×10^{-6} $khPa^1$ and P denotes the pressure in hectopascal(hPa); T **is the absolute temperature in kelvins (K); and** z **is the geopotential height above mean sea level in metres (m)** (A. N. Kolmogorov 1941; V. I. Tatarskii 1971; V. I. Tatarski 2016; F. Quatresooz et al. 2023).

Understanding and mitigating turbulence is crucial for enhancing image quality in ground-based astronomical observations. **AO** systems utilize turbulence models to predict and correct wavefront distortions in real time (T. R. Rimmele et al. 2020). This systems, not only enables sharper imaging but also facilitates detailed studies of solar phenomena, planetary systems, and stellar objects. Additionally, atmospheric dispersion caused by refractive index variations can be counteracted using prisms designed to realign spectral components **(C. Wynne & S. Worswick 1986)**. The optimization of observatory sites further reduces turbulence-induced limitations (J. W. Hardy 1998; C. Haslebacher et al. 2022). Strategic site selection (favoring elevated, arid regions with stable atmospheric conditions) minimizes the effects of temperature gradients and convection currents. This interdisciplinary approach, combining insights from physics, astronomy, and meteorology, highlights the intricate relationship between atmospheric dynamics and optical performance.

6.2. *Atmospheric Turbulence Energy Spectrum*

The analysis of atmospheric turbulence through energy spectra provides critical insights into the variability of meteorological parameters across altitudes and scales, which is fundamental for calculating refractive index fluctuations K. K. Tung & W. W. Orlando (2003). Turbulence induced variations in temperature, pressure, and wind speed directly affect the refractive index, remarkably influencing the performance of systems such as astronomical telescopes and adaptive optics.

Atmospheric turbulence modifies air density by introducing temperature and pressure fluctuations, which alter the refractive index. The turbulence energy spectrum, characterized by distinct scaling regimes ($k^{-5/3}$ for the inertial subrange and k^{-3} for enstrophy dominated scales), show the distribution of energy across spatial and temporal scales. The spectral slope (β) quantifies the strength of turbulence at various scales, providing a structure to evaluate refractive index variability. Figures 10 and 11 illustrate the energy spectra of temperature and wind speed fluctuations, respectively, highlighting the dominant turbulent processes at multiple altitudes.

The turbulence regimes vary significantly with altitude, reflecting differences in atmospheric dynamics across the surface layer, boundary layer, and free atmosphere (A. S. Monin & A. M. Obukhov 1954; J. R. Garratt 1994). Near the surface, small-scale turbulence driven by energy flux dominates, while higher altitudes are governed by large-scale processes associated with entrophy flux. These altitude dependent variations influence the vertical distribution of refractive index fluctuations, necessitating the consideration of layer-specific turbulence characteristics to each atmospheric region. Furthermore, daily and seasonal fluctuations in turbulence, **manifested by** shifts in spectral patterns, **induce corresponding** variations in the refractive index. For example, intense turbulence during the day caused by solar heating or increased atmospheric stability during JJA noticeably affects optical path lengths.

By fitting **the observed** turbulence spectra to theoretical models, the energy spectrum enables refined predictions of refractive index variability. Parameters such as the refractive index structure function C_n^2, derived from spectral

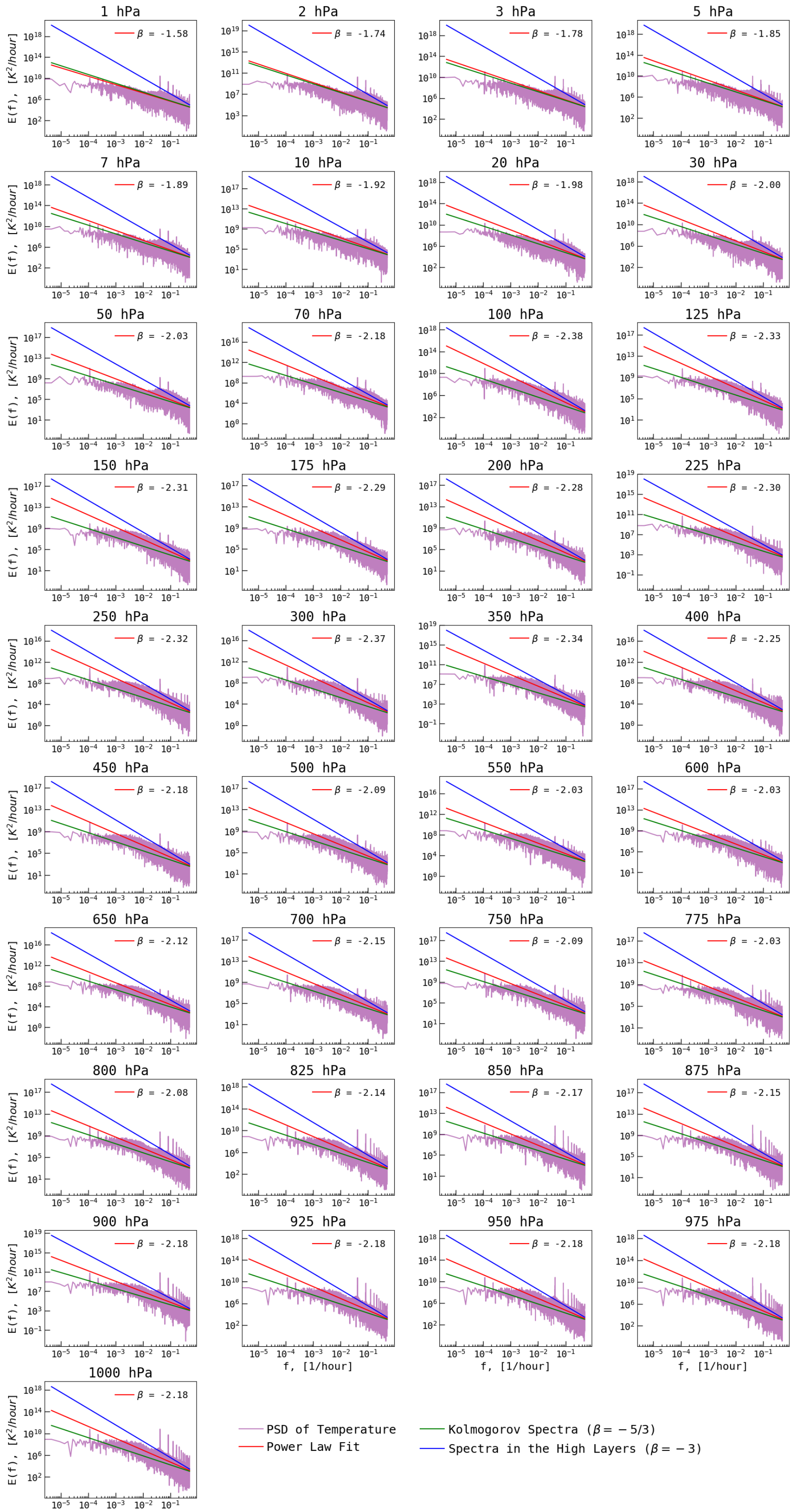

Figure 10. Energy spectra of air temperature fluctuations across atmospheric pressure levels at OPD. Each panel shows the power spectral density (PSD, pruple line) fitted with power law slopes (red line), compared against theoretical Kolmogorov spectra with $\beta = -5/3$ (blue line, inertial subrange) and $\beta = -3$ (green line, enstrophy-dominated regime). The spectral slope β for each pressure level is indicated in the upper right corner of each panel. Frequency is expressed in units of [1/hour], with energy density in [K^2/hour].

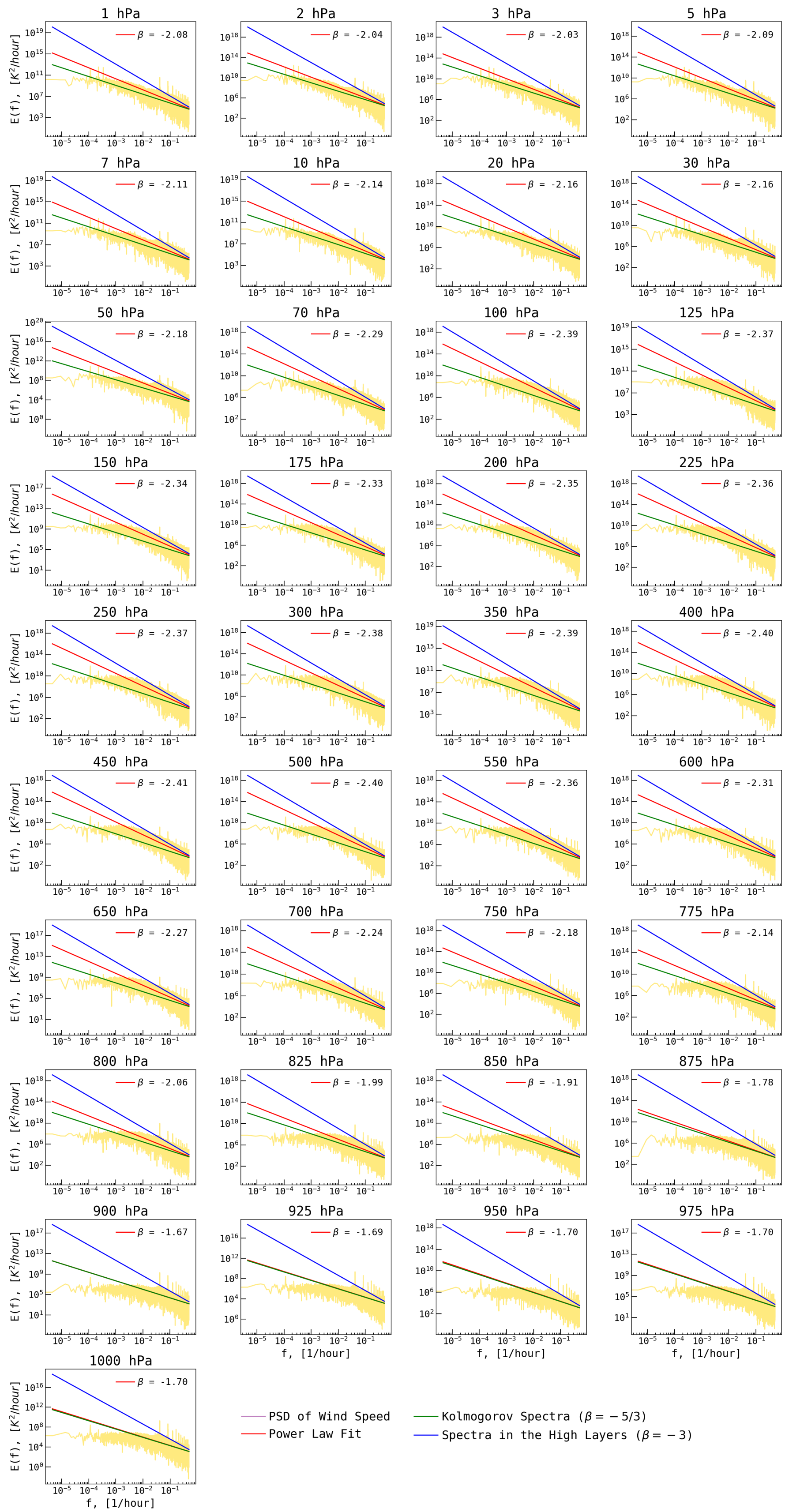

Figure 11. Energy spectra of wind speed fluctuations across atmospheric pressure levels at OPD. Each panel shows the power spectral density (PSD, yellow points) fitted with power law slopes (red line), compared against theoretical Kolmogorov spectra with $\beta = -5/3$ (blue line, inertial subrange) and $\beta = -3$ (green line, enstrophy-dominated regime). The spectral slope β for each pressure level is indicated in the upper right corner of each panel. Frequency is expressed in units of [1/hour], with energy density in [(m/s)^2/hour].

analysis, quantify the magnitude and scale of turbulence. Figures 12 and 13 present the frequency dependent energy spectra of wind speed and temperature across pressure levels, emphasizing the transitions between scaling regimes and the underlying turbulent mechanisms.

The spectral slopes β, shown across varying altitudes, reflect the dominant turbulent processes, relieving in the identification of energy transfer mechanisms. These understanding improve the accuracy of turbulence models, improving their applicability in adaptive optics and astronomical observations. Seasonal and diurnal patterns, observed through changes in spectral characteristics, further underscore the complexity of refractive index variability. The analysis of the energy spectrum provides as a strong foundation for calculating variations in the refractive index, which are critical for optical applications. By measuring turbulence induced fluctuations in meteorological variables, the energy spectrum captures the spatial and temporal variability of the refractive index, provide accurate modeling under diverse environmental conditions. This insight is not just theoretical but highly practical, supporting the optimization of systems dependent on atmospheric stability, such as adaptive optics and high-resolution imaging at the OPD observatory.

6.3. *Refractive index*

Refractive index variations degrade image quality by causing distortions along the optical path, which is a problem for astronomy (R. Davies & M. Kasper 2012). The refractive index structure parameter C_n^2 quantifies the strength of turbulence across atmospheric layers. It is a critical input **to** mitigate turbulence-induced distortions.

Turbulence originates primarily in the troposphere, where temperature gradients and wind speed variations are most pronounced. The seasonal variation of C_n^2 values, shown in Figures 14 and 15, reflects the dynamic interplay between temperature gradients and wind shear across different altitudes. These figures highlight seasonal patterns in turbulence strength and distribution during day and night.

Figure 14 illustrates daytime seasonal changes in C_n^2, with purple curves representing wind-induced turbulence and red curves corresponding to temperature-driven variations, the daytime reveal the influence of solar heating and atmospheric instability. The troposphere, at lower altitudes, displays the highest C_n^2 values due to intense turbulence driven by rapid temperature changes and wind fluctuations. Midday solar heating intensifies atmospheric instability, leading to increased scattering and image degradation. At higher altitudes, in the mesosphere, turbulence is predominantly driven by wind dynamics.

In the stratosphere, more stable temperature gradients lead to moderate levels of turbulence **, typically within $10^{-16} \lesssim C_n^2 \lesssim 10^{-13}\,\mathrm{m}^{-2/3}$. Values below $10^{-16}\,\mathrm{m}^{-2/3}$ indicate weak (good) conditions, whereas those above $10^{-13}\,\mathrm{m}^{-2/3}$ correspond to strong (poor) turbulence. Representative daytime measurements at benchmark solar sites fall within these ranges, at the Teide Observatory (Tenerife), nearsurface C_n^2 values cluster around a few $10^{-14}\,\mathrm{m}^{-2/3}$ at local noon (D. Sprung & E. Sucher 2013), while at Haleakalā (Hawaii) , daytime minima of the Fried parameter reach ~ 3–4 cm at 500 nm, consistent with strong ground-layer turbulence near midday (R. J. Alliss & B. D. Felton 2009)**. Although localized peaks in C_n^2 arise from phenomena such as wind shear and temperature inversions. Seasonal patterns indicate that during JJA and SON, jet stream dynamics intensify turbulence, while in DJF, solar heating and convection dominate. Transitional seasons like MAM display moderate C_n^2 values, reflecting a balance between reduced solar heating and variable weather conditions. At higher altitudes, such as the mesosphere, turbulence is dominated by wind-induced mixing, particularly during periods of strong wind shear. The high-altitude turbulence layers notably impact the **OPD**. Figure 15, illustrates that nighttime turbulence patterns differ from daytime due to the absence of direct solar heating, leading to more stable temperature gradients. However, localized turbulence persists in the troposphere and lower stratosphere due to residual heat, wind shear, and atmospheric mixing. In the mesosphere, wind-driven turbulence remains significant, with seasonal peaks influenced by large-scale atmospheric dynamics such as jet streams and planetary waves.

In the stratosphere, more stable temperature gradients lead to moderate levels of turbulence, although localized peaks in C_n^2 arise from phenomena such as wind shear and temperature inversions. Seasonal patterns indicate that during JJA and SON, jet stream dynamics intensify turbulence, while in DJF, solar heating and convection dominate. Transitional seasons like MAM display moderate C_n^2 values, reflecting a balance between reduced solar heating and variable weather conditions. At higher altitudes, such as the mesosphere, turbulence is dominated by wind-induced mixing, particularly during periods of strong wind shear. The high-altitude turbulence layers notably impact the **OPD** . Figure (15) illustrates that nighttime turbulence patterns differ from daytime due to the absence of direct solar heating, leading to more stable temperature gradients. However, localized turbulence persists in the troposphere and lower stratosphere due to residual heat, wind shear, and atmospheric mixing. In the mesosphere, wind-driven

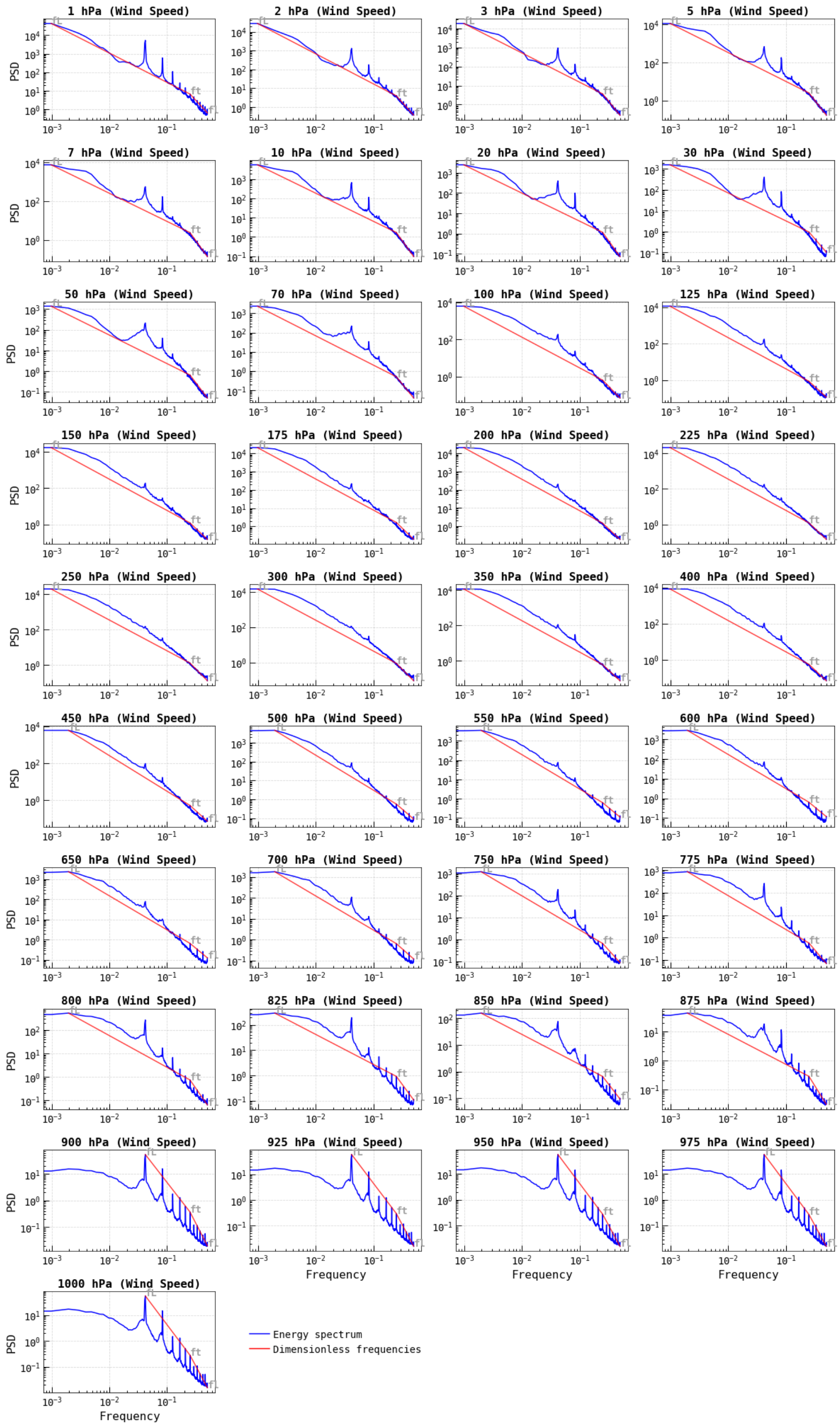

Figure 12. Frequencies of wind speed across multiple atmospheric pressure levels (from 1 hPa to 1000 hPa). The blue lines represent the Power Spectral Density, illustrating the distribution of energy across various spatial frequencies, while the red lines mark the dimensionless frequency scaling regimes.

turbulence remains significant, with seasonal peaks influenced by large-scale atmospheric dynamics such as jet streams and planetary waves.

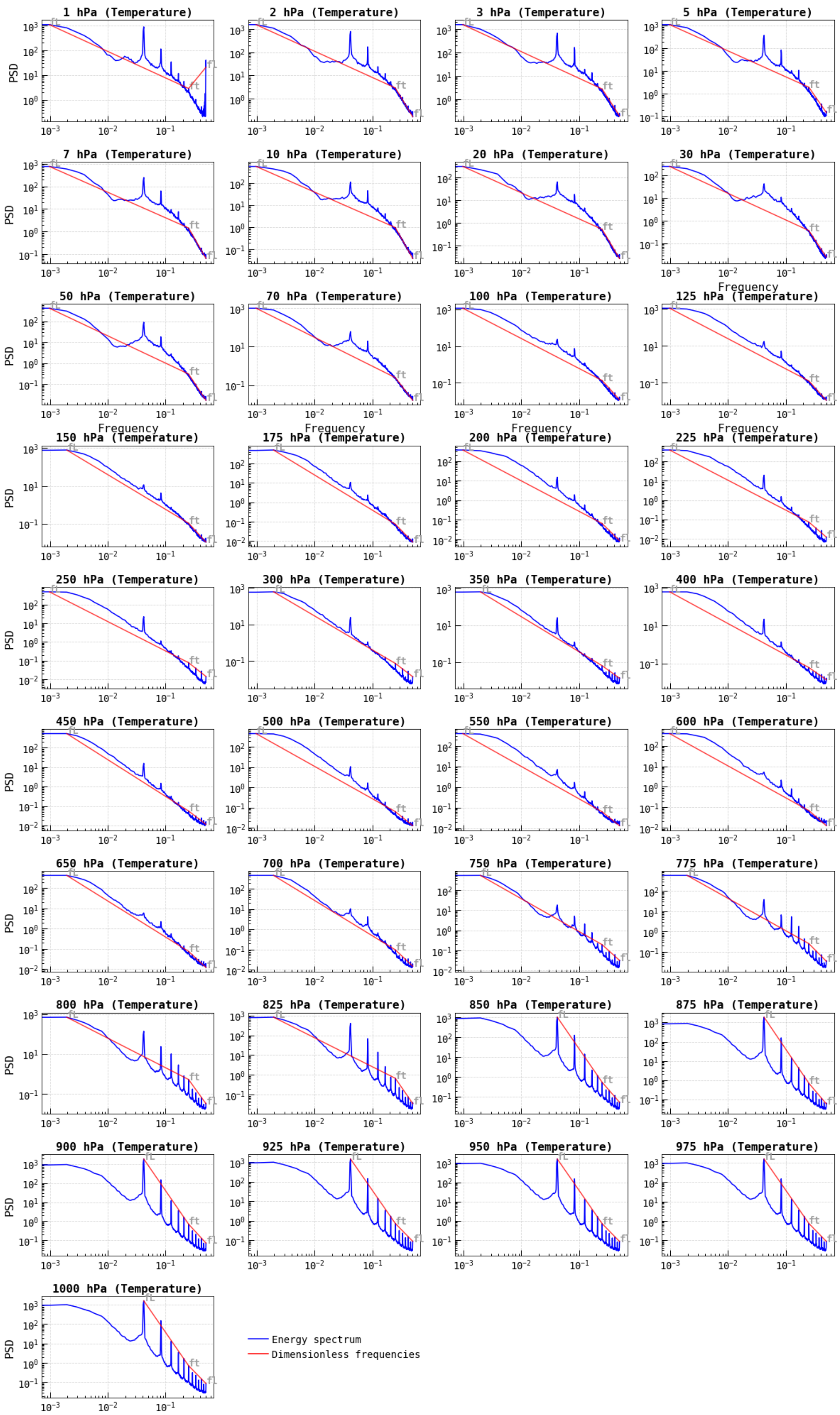

Figure 13. Identification of the theoretical regimes, where f_L is the frequency from the low spatial frequency range; f_l is the frequency in the high spatial frequency range; f_t is the spatial frequency in the transient spectral region (from -3 to $-\frac{5}{3}$).

The behavior of turbulence follows the Kolmogorov model, in which energy is injected at large scales and cascades down to smaller scales, where it dissipates. Most optical distortions occur on larger scales as these dominate the energy spectrum. Crucially, refractive index variations across the visible-to-infrared spectrum are nearly **wavelength-**

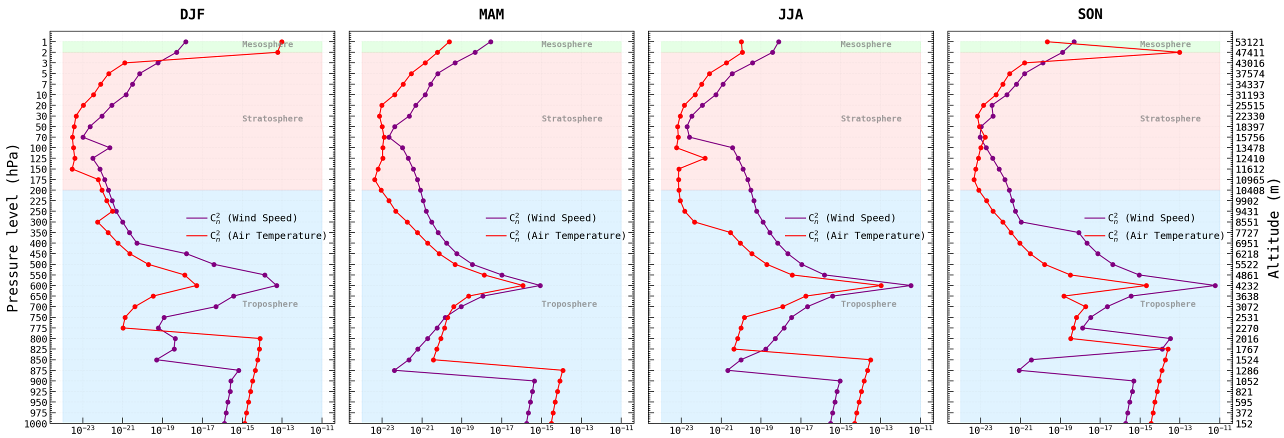

Figure 14. Seasonal variations in C_n^2 during the daytime, turbulence intensity is highest in the troposphere due to solar heating, with additional contributions from stratospheric wind shear and mesospheric wind-driven mixing.

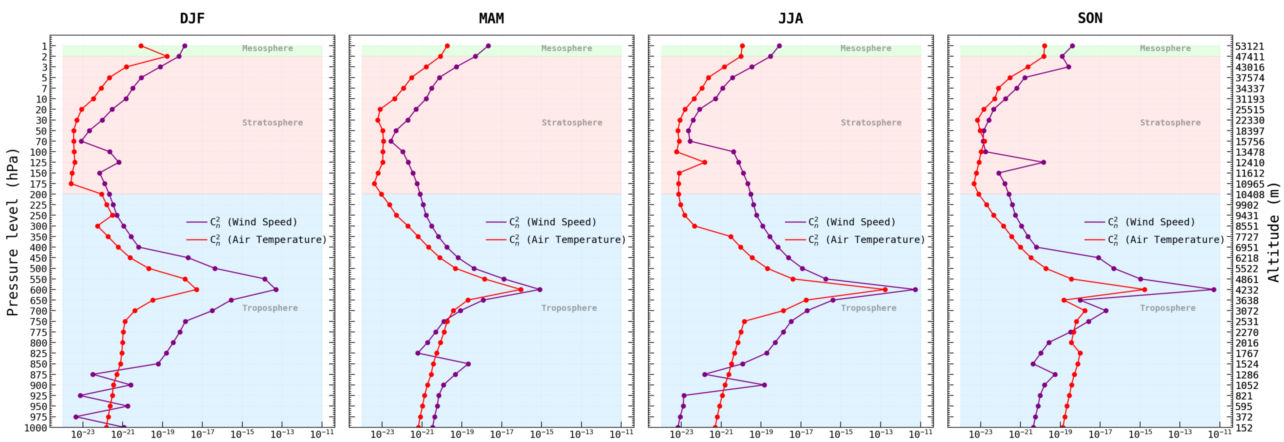

Figure 15. Seasonal variations in C_n^2 during the nighttime, illustrating how residual heat and wind shear affect turbulence across the troposphere, stratosphere, and mesosphere. High-altitude turbulence remains dominated by wind-driven effects, even in the absence of solar heating at OPD.

independent, minimizing dispersion effects in this range. This makes **the correction of turbulence effects** in astronomy feasible across multiple wavelengths.

These results feature the importance of accounting for seasonal and altitudinal turbulence variations in the design and operation of solar observatories. By integrating precise models of C_n^2 variability, future advancements in the **AO** system can further enhance observational capabilities across multiple wavelengths.

6.4. *Adaptive Optics Considerations*

Atmospheric turbulence presents a important challenge for high-resolution ground-based astronomy by distorting incoming wavefronts due to refractive index fluctuations (J. W. Hardy 1998; R. Davies & M. Kasper 2012). AO systems reduce these effects through real-time wavefront correction, improve telescope performance. The underlying physical framework is well described by Kolmogorov's turbulence theory, which explains how energy cascades from large-scale motions to the smaller scales that dominate optical seeing. Modern AO implementations use wavefront sensors and deformable mirrors to counteract distortions in real time, thus restoring diffraction-limited resolution (P. G. Kovadlo et al. 2019). AO performance is governed by three parameters: the Fried parameter (r_0), the isoplanatic angle (θ_0), and the atmospheric coherence time (τ_0).

In this work, these parameters are computed from the seasonal median of C_n^2 profiles and turbulence-weighted wind speeds derived from ERA5 reanalysis, vertically integrated over the OPD (0–18 km). Table 4 presents the seasonal and diurnal medians for $\lambda = 500$ nm. The r_0 peaks in austral autumn

(MAM) and winter (JJA), with median daytime values of 13–16 cm and nighttime values of 14–18 cm. The θ_0 remains relatively stable throughout the year, ranging from 3.4–3.6″ during the day and 4.3–4.7″ at night, while the τ_0 reaches its maximum during calm nocturnal periods in JJA and SON (7.2–8.3 ms)

Table 4. Comparative AO metrics at benchmark observatories (literature ranges at $\lambda = 500$ nm). Values are indicative medians ranges; methods and temporal sampling differ across sites.

Site	Regime	r_0 (cm)	θ_0 (arcsec)	τ_0 (ms)	Notes	Ref.
OPD (this work)	Day	13–16	3.4–3.6	5.4–5.7	Seasonal medians (MAM/SON best)	This work
	Night	14–18	4.3–4.7	7.2–8.3	Seasonal medians (JJA/SON best)	This work
Cerro Paranal	Night	15–20	1.9–2.3	3–6†	VLT site monitor; excellent free-atm.	M. Sarazin et al. (2008)
Mauna Kea	Night	14–19	2.0–2.4	3–6†	Mean conditions across facilities	M. Chun et al. (2009)
Teide (OT) / ORM	Night	12–15	2.2–2.4	3–5†	Canary Islands sites	G. Lombardi et al. (2009)
Big Bear (BBSO)	Day	13–15	2–3	–	Solar AO (site-dependent seeing)	C. Denker et al. (2007)

Note—OPD values are seasonal medians over 0–18 km above site. External sites list typical literature ranges at $\lambda = 500$ nm. †Indicative τ_0 ranges inferred from wind climatologies and seeing statistics; many studies do not tabulate τ_0 directly. Direct comparisons should be interpreted with caution, as site-testing methodologies, instrument heights, and temporal coverage differ across locations.

In terms of r_0, our nighttime values (14–17cm) are comparable to those reported for Cerro Paranal (15–20 cm; M. Sarazin et al. 2008) and Mauna Kea (14–19 cm; M. Chun et al. 2009), and exceed typical values measured at Teide Observatory and Roque de los Muchachos (12–15cm; G. Lombardi et al. 2009). Daytime values (13–16 cm) are competitive with the best solar AO sites, such as Big Bear Solar Observatory (13–15 cm; C. Denker et al. 2007), though still below nighttime performance.

Finally, OPD exhibits AO-relevant conditions that are competitive with internationally recognized sites. Seasonal and diurnal differences highlight the importance of tailoring AO operation modes to prevailing conditions. While these cross-site comparisons emphasize OPD's potential, they should be interpreted with caution, since differences in methodology and temporal coverage across datasets mean that the results are indicative rather than strictly equivalent.

7. CONCLUSIONS

This study **presents** a comprehensive assessment of daytime sky quality and atmospheric turbulence at the **OPD**, emphasizing the refractive index structure derived from ERA5 reanalysis data. By advancing the understanding of atmospheric dynamics, **these** findings contribute to optimizing ground-based astronomical observations, particularly **AO** systems and solar observation instruments such as the **GSST**.

The results confirm important diurnal and seasonal variations in atmospheric variables (including temperature, wind speed, and relative humidity) significantly and critically affect sky quality.

The ERA5 reanalysis dataset exhibited a strong correlation with surface meteorological observations for temperature and dew point, supporting its use in deriving the variability patterns required for C_n^2 estimation. In contrast, wind speed showed a weaker correlation, mainly due to the complex orography surrounding the OPD site, which is not completely resolved at the spatial resolution of ERA5. This underestimation can influence the mechanical turbulence component and should be addressed with local corrections or complementary measurements when high accuracy is required. Even so, given the strong agreement in thermal variables, ERA5 remains a valuable resource for investigating atmospheric conditions at high-altitude observatories, particularly in the absence of extensive observational datasets.

The study **identify** solar heating, wind shear, and seasonal jet stream activity as primary turbulence drivers. Near-surface turbulence, driven by temperature gradients, peaks during the day, while high-altitude jet streams impact optical clarity, particularly in JJA. Analysis of energy spectra validated Kolmogorov's turbulence theory, providing important knowledge into refractive index fluctuations that degrade astronomical image quality.

Notably, turbulence intensity decreases with altitude; however, variability introduced by jet streams (especially during JJA and SON) requires others approaches. JJA months and nighttime conditions generally offer the best observational opportunities, characterized by reduced cloud cover and turbulence levels. The temporal and spatial characteristics of turbulence further highlight the necessity of AO systems tailored to the unique atmospheric dynamics at OPD.

The analysis of the wind rose **provide** us with information on the direction of the winds, indicating that the winds towards the north predominate during the day, while the winds in a south-southeast direction predominate at night, this is important to better program astronomical observations.

Cloud cover emerged as a key determinant of observational quality. Lower cloud fractions during JJA mornings and evenings align with optimal conditions for solar and stellar imaging.

The findings provide actionable guidance for improving AO system design and observational strategies. By utilizing ERA5 data to predict turbulence and atmospheric variability, observatories can optimize scheduling for low-turbulence periods, enhancing image resolution and data fidelity. Future research should prioritize integrating real-time turbulence measurements with reanalysis data to refine models and mitigate atmospheric distortions.

The study underscores the critical role of understanding turbulence dynamics in improving solar observation accuracy and predicting solar phenomena. These insights are vital for optimizing OPD's observational capabilities throughout the year.

This work bridges critical gaps in understanding daytime atmospheric turbulence and provides important knowledge for advancing high-precision optical astronomy. It establishes a strong foundation for enhanced solar and stellar research at OPD and similar observatories, which contributes to the broader fields of ground-based astronomy and **AO** innovation.

ACKNOWLEDGMENTS

The authors acknowledge the CNPq/PCI grant Process Number 301353/2024-7, MCTI-INPE; CNPq, Process Number 312377/2022-3; AEB; and acknowledge São Paulo Research Foundation (FAPESP), Brazil, Process Number 2021/13309-6 for their financial support; the LNA for their collaboration and weather data and finally the Copernicus Climate Change Service for access to the ERA5 dataset.

APPENDIX

A. LONG-TERM SKY CONDITION STATISTICS

A.1. *Daytime total cloud coverage condition*

Table 5 presents a comprehensive 25-year climatology of daytime sky conditions at the OPD, providing essential baseline data for astronomical observation planning and site characterization studies.

The analysis reveals distinct seasonal patterns in sky clarity, with the austral JJA months consistently showing the highest frequency of clear sky conditions. July emerges as the optimal month with an average of 96.2 clear periods, followed closely by August (101.8 clear periods) and June (64.4 clear periods). This JJA maximum aligns with the regional dry season, when reduced convective activity and lower humidity levels create favorable conditions for astronomical observations.

In contrast, the austral DJF show significantly reduced clear sky frequency, with December, January, and February averaging only 1.6, 2.9, and 3.0 clear periods respectively. This dramatic seasonal contrast reflects the influence of the South American Monsoon system, which brings increased cloud cover and precipitation during DJF.

The transitional seasons exhibit intermediate behavior, with MAM showing a gradual increase in clear sky frequency from March (3.5 periods) to May (43.5 periods), while SON displays the reverse trend, with September maintaining relatively high clear sky frequency (54.9 periods) before declining toward DJF conditions.

Notably, the data show considerable interannual variability, with some years exhibiting exceptional conditions. For example, 2008 recorded 190 clear periods in July, while 2003 achieved 155 clear periods in June. Such variations likely reflect large-scale climate oscillations and highlight the importance of long-term statistical characterization for observatory planning.

The average annual clear sky frequency of 404.2 periods positions OPD favorably among mid-latitude astronomical sites, particularly considering the challenging tropical/subtropical climate conditions. The pronounced seasonal cycle emphasizes the importance of scheduling high-priority observations during the optimal JJA period while developing adaptive strategies for the more challenging austral summer months.

Table 5. Monthly distribution of clear and cloudy sky conditions during daytime hours (06:00–18:00 local time) at OPD from 1999–2023. Clear sky conditions are defined as total cloud cover ≤10% for at least 6 consecutive hours. Cloudy conditions are defined as total cloud cover between 10% and 65% for at least 6 consecutive hours. Values represent the number of clear/cloudy days per month, with monthly averages and annual totals provided.

Year	Month Sky	Jan	Feb	Mar	Apr	May	Jun	Jul	Aug	Sep	Oct	Nov	Dec	Total
1999	Clear	0.00	0.00	3.00	5.00	53.00	45.00	25.00	136.00	74.00	1.00	0.00	5.00	347.00
	Cloudy	9.00	0.00	30.00	33.00	45.00	5.00	66.00	21.00	17.00	29.00	38.00	23.00	316.00
2000	Clear	1.00	0.00	1.00	41.00	71.00	104.00	54.00	77.00	9.00	6.00	0.00	1.00	365.00
	Cloudy	18.00	11.00	16.00	50.00	29.00	26.00	18.00	13.00	18.00	41.00	8.00	14.00	262.00
2001	Clear	0.00	0.00	1.00	34.00	29.00	40.00	89.00	77.00	12.00	26.00	0.00	5.00	313.00
	Cloudy	45.00	27.00	44.00	35.00	29.00	25.00	7.00	37.00	17.00	13.00	11.00	12.00	302.00
2002	Clear	0.00	0.00	13.00	23.00	27.00	63.00	75.00	48.00	21.00	23.00	0.00	0.00	293.00
	Cloudy	13.00	13.00	57.00	64.00	36.00	10.00	19.00	44.00	11.00	44.00	10.00	9.00	330.00
2003	Clear	6.00	4.00	2.00	20.00	63.00	155.00	120.00	95.00	52.00	11.00	0.00	1.00	529.00
	Cloudy	9.00	37.00	41.00	29.00	20.00	27.00	22.00	8.00	21.00	13.00	21.00	14.00	262.00
2004	Clear	0.00	0.00	0.00	16.00	17.00	48.00	45.00	119.00	128.00	12.00	5.00	0.00	390.00
	Cloudy	13.00	26.00	23.00	27.00	21.00	26.00	20.00	26.00	24.00	3.00	14.00	32.00	255.00
2005	Clear	0.00	1.00	0.00	28.00	70.00	79.00	106.00	170.00	1.00	5.00	0.00	0.00	460.00
	Cloudy	8.00	39.00	25.00	37.00	21.00	27.00	14.00	25.00	14.00	10.00	40.00	2.00	262.00
2006	Clear	0.00	0.00	2.00	21.00	51.00	64.00	158.00	87.00	65.00	3.00	0.00	0.00	451.00
	Cloudy	30.00	27.00	29.00	42.00	7.00	38.00	10.00	21.00	15.00	11.00	15.00	1.00	246.00
2007	Clear	0.00	10.00	4.00	5.00	30.00	114.00	127.00	90.00	71.00	9.00	0.00	1.00	461.00
	Cloudy	0.00	31.00	44.00	62.00	17.00	14.00	8.00	10.00	37.00	23.00	30.00	50.00	326.00
2008	Clear	0.00	0.00	8.00	33.00	111.00	13.00	190.00	118.00	49.00	2.00	0.00	0.00	524.00
	Cloudy	13.00	16.00	28.00	13.00	23.00	39.00	15.00	30.00	6.00	13.00	21.00	29.00	246.00
2009	Clear	0.00	0.00	0.00	16.00	42.00	57.00	25.00	59.00	11.00	0.00	0.00	0.00	210.00
	Cloudy	8.00	14.00	11.00	27.00	33.00	26.00	27.00	31.00	18.00	20.00	29.00	29.00	273.00
2010	Clear	2.00	7.00	13.00	11.00	30.00	117.00	126.00	162.00	56.00	9.00	12.00	6.00	551.00
	Cloudy	4.00	43.00	48.00	22.00	35.00	9.00	15.00	9.00	16.00	21.00	32.00	13.00	267.00
2011	Clear	0.00	0.00	0.00	6.00	21.00	63.00	85.00	106.00	95.00	17.00	0.00	5.00	398.00
	Cloudy	41.00	20.00	8.00	36.00	18.00	27.00	9.00	4.00	20.00	28.00	13.00	39.00	263.00
2012	Clear	0.00	0.00	8.00	0.00	8.00	14.00	155.00	106.00	51.00	21.00	10.00	0.00	373.00
	Cloudy	14.00	23.00	52.00	55.00	13.00	23.00	5.00	19.00	24.00	31.00	6.00	28.00	293.00
2013	Clear	0.00	3.00	0.00	25.00	51.00	10.00	94.00	76.00	49.00	1.00	12.00	0.00	321.00
	Cloudy	21.00	30.00	6.00	5.00	19.00	32.00	30.00	36.00	7.00	17.00	14.00	12.00	229.00
2014	Clear	7.00	27.00	3.00	9.00	13.00	42.00	34.00	137.00	76.00	53.00	0.00	0.00	401.00
	Cloudy	48.00	37.00	19.00	12.00	8.00	24.00	4.00	19.00	8.00	24.00	15.00	15.00	233.00
2015	Clear	25.00	0.00	0.00	0.00	12.00	54.00	64.00	173.00	91.00	9.00	0.00	0.00	428.00
	Cloudy	44.00	24.00	3.00	19.00	8.00	25.00	17.00	12.00	17.00	35.00	1.00	8.00	213.00
2016	Clear	0.00	0.00	2.00	48.00	23.00	66.00	111.00	82.00	18.00	4.00	0.00	0.00	354.00
	Cloudy	8.00	26.00	24.00	41.00	8.00	8.00	16.00	23.00	60.00	23.00	27.00	46.00	310.00
2017	Clear	0.00	9.00	6.00	0.00	18.00	61.00	94.00	95.00	172.00	22.00	19.00	2.00	498.00
	Cloudy	5.00	26.00	11.00	17.00	23.00	26.00	38.00	22.00	13.00	19.00	18.00	24.00	242.00
2018	Clear	0.00	1.00	7.00	15.00	62.00	17.00	102.00	54.00	39.00	0.00	0.00	4.00	301.00
	Cloudy	4.00	11.00	35.00	33.00	11.00	31.00	24.00	19.00	20.00	16.00	13.00	40.00	257.00
2019	Clear	16.00	12.00	1.00	22.00	33.00	78.00	105.00	71.00	21.00	36.00	0.00	5.00	400.00
	Cloudy	45.00	33.00	20.00	51.00	22.00	51.00	26.00	17.00	39.00	37.00	19.00	18.00	378.00
2020	Clear	15.00	0.00	0.00	29.00	101.00	39.00	104.00	128.00	64.00	2.00	0.00	0.00	482.00
	Cloudy	23.00	11.00	25.00	6.00	11.00	31.00	33.00	5.00	23.00	77.00	62.00	14.00	321.00
2021	Clear	0.00	0.00	14.00	24.00	50.00	46.00	148.00	116.00	34.00	0.00	0.00	0.00	432.00
	Cloudy	16.00	51.00	65.00	24.00	22.00	36.00	7.00	10.00	48.00	8.00	29.00	32.00	348.00
2022	Clear	0.00	0.00	0.00	12.00	62.00	73.00	102.00	64.00	46.00	0.00	7.00	5.00	371.00
	Cloudy	60.00	25.00	79.00	23.00	57.00	4.00	16.00	19.00	31.00	54.00	16.00	20.00	404.00
2023	Clear	0.00	0.00	0.00	1.00	40.00	148.00	68.00	98.00	67.00	0.00	31.00	0.00	453.00
	Cloudy	9.00	10.00	51.00	29.00	20.00	1.00	33.00	25.00	25.00	14.00	7.00	38.00	262.00
Average	Clear	2.88	2.96	3.52	17.76	43.52	64.40	96.24	101.76	54.88	10.88	3.84	1.60	404.24
	Cloudy	20.32	24.44	31.76	31.68	22.24	23.64	19.96	20.20	21.96	24.96	20.36	22.48	284.00

A.2. *Nighttime Sky Condition Statistics*

Table 6 presents the nighttime counterpart to the daytime analysis, providing a baseline data for traditional nighttime astronomical observations at OPD. The comparison between diurnal and nocturnal sky conditions provides an understanding of the atmospheric dynamics affecting ground-based astronomy.

Nighttime observations generally benefit from more stable atmospheric conditions compared to daytime, as evidenced by the slightly reduced seasonal contrast in clear sky frequency. Under the stringent 10% cloud cover threshold, nighttime conditions show an annual average of 388.6 clear periods, remarkably similar to daytime statistics but with different seasonal distribution patterns.

The austral winter months remain optimal for nighttime observations, with July and August achieving 98.3 and 98.6 clear periods respectively. However, the transition months show interesting differences from daytime patterns. May demonstrates particularly favorable nighttime conditions (45.6 clear periods), while September maintains relatively good conditions (41.7 clear periods), providing extended observational windows during seasonal transitions.

The austral summer continue to present the most challenging conditions, with minimal clear sky occurrence averaging 1.5–2.1 clear periods per month. This persistent pattern reflects the dominance of the South American Monsoon system, which affects both diurnal and nocturnal atmospheric conditions.

Notably, nighttime conditions show enhanced stability during certain transitional periods compared to daytime. The reduced solar heating eliminates convective turbulence, leading to more predictable atmospheric behavior and improved seeing conditions when skies are clear. This is particularly evident during MAM and SON months, where nighttime observations may be more reliable than their daytime counterparts.

The cloudy sky category (10–65% cloud cover) represents 435.1 periods annually, indicating partially usable conditions for less demanding observational programs. These conditions may still permit certain types of nighttime astronomy, including bright object observations, instrument calibration, and adaptive optics testing.

For OPD's traditional nighttime observational programs, these statistics confirm the site's viability for stellar astronomy, with the JJA months providing optimal conditions for deep-sky observations, high-resolution spectroscopy, and precision photometry. The data support scheduling critical nighttime observations during the May–August window while maintaining operational flexibility during transitional seasons.

The comparison between daytime (solar) and nighttime (stellar) observational windows at OPD demonstrates the site's dual capability for comprehensive astronomical research, with both regimes showing similar overall clear sky frequencies but complementary seasonal optimization periods.

Table 6. Monthly distribution of clear and cloudy sky conditions during nighttime hours (18:00–06:00 local time) at OPD from 1999–2023. Clear sky conditions are defined as total cloud cover ≤10% for at least 6 consecutive hours. Cloudy conditions are defined as total cloud cover between 10% and 65% for at least 6 consecutive hours. Values represent the number of clear/cloudy nights per month, with monthly averages and annual totals provided.

Year	Month Sky	Jan	Feb	Mar	Apr	May	Jun	Jul	Aug	Sep	Oct	Nov	Dec	Total
1999	Clear	0.00	0.00	0.00	1.00	66.00	72.00	31.00	139.00	65.00	7.00	0.00	5.00	386.00
	Cloudy	15.00	6.00	58.00	38.00	38.00	37.00	75.00	32.00	43.00	21.00	28.00	43.00	434.00
2000	Clear	0.00	0.00	0.00	56.00	45.00	83.00	65.00	15.00	2.00	12.00	0.00	0.00	278.00
	Cloudy	33.00	23.00	38.00	72.00	49.00	60.00	32.00	35.00	40.00	47.00	16.00	31.00	476.00
2001	Clear	0.00	1.00	0.00	15.00	28.00	27.00	88.00	86.00	10.00	25.00	0.00	5.00	285.00
	Cloudy	46.00	23.00	38.00	68.00	65.00	73.00	18.00	41.00	39.00	21.00	37.00	25.00	494.00
2002	Clear	0.00	0.00	16.00	7.00	41.00	64.00	88.00	54.00	11.00	4.00	0.00	0.00	285.00
	Cloudy	19.00	9.00	76.00	90.00	40.00	50.00	13.00	81.00	40.00	49.00	5.00	20.00	492.00
2003	Clear	6.00	14.00	0.00	14.00	76.00	157.00	121.00	101.00	44.00	20.00	0.00	0.00	553.00
	Cloudy	6.00	53.00	52.00	66.00	45.00	42.00	26.00	25.00	21.00	30.00	35.00	6.00	407.00
2004	Clear	0.00	0.00	0.00	5.00	12.00	56.00	51.00	126.00	77.00	13.00	1.00	0.00	341.00
	Cloudy	6.00	22.00	44.00	35.00	28.00	14.00	39.00	27.00	57.00	13.00	31.00	29.00	345.00
2005	Clear	0.00	0.00	1.00	7.00	47.00	64.00	107.00	139.00	10.00	4.00	0.00	0.00	379.00
	Cloudy	11.00	60.00	47.00	67.00	46.00	80.00	33.00	45.00	27.00	15.00	37.00	12.00	480.00
2006	Clear	0.00	0.00	0.00	29.00	96.00	53.00	151.00	90.00	40.00	7.00	3.00	0.00	469.00
	Cloudy	23.00	27.00	37.00	58.00	19.00	78.00	45.00	29.00	30.00	16.00	41.00	5.00	408.00
2007	Clear	0.00	4.00	4.00	9.00	37.00	106.00	129.00	111.00	17.00	8.00	0.00	0.00	425.00
	Cloudy	0.00	59.00	91.00	72.00	36.00	31.00	9.00	35.00	61.00	30.00	39.00	48.00	511.00
2008	Clear	0.00	0.00	1.00	16.00	101.00	0.00	200.00	94.00	48.00	0.00	0.00	4.00	464.00
	Cloudy	17.00	16.00	48.00	45.00	39.00	84.00	37.00	51.00	5.00	23.00	15.00	41.00	421.00
2009	Clear	0.00	0.00	0.00	15.00	44.00	67.00	31.00	61.00	6.00	5.00	0.00	0.00	229.00
	Cloudy	26.00	16.00	14.00	46.00	33.00	38.00	44.00	44.00	51.00	14.00	34.00	27.00	387.00
2010	Clear	0.00	0.00	1.00	2.00	32.00	152.00	132.00	179.00	60.00	16.00	6.00	0.00	580.00
	Cloudy	4.00	52.00	50.00	47.00	44.00	12.00	52.00	30.00	49.00	11.00	41.00	13.00	405.00
2011	Clear	0.00	0.00	0.00	0.00	28.00	78.00	91.00	107.00	73.00	3.00	0.00	2.00	382.00
	Cloudy	41.00	48.00	5.00	69.00	40.00	28.00	36.00	13.00	42.00	45.00	34.00	49.00	450.00
2012	Clear	0.00	0.00	0.00	0.00	5.00	7.00	143.00	113.00	28.00	12.00	16.00	0.00	324.00
	Cloudy	29.00	33.00	92.00	73.00	40.00	41.00	22.00	22.00	61.00	44.00	23.00	28.00	508.00
2013	Clear	0.00	2.00	0.00	15.00	75.00	32.00	76.00	74.00	28.00	4.00	5.00	0.00	311.00
	Cloudy	12.00	35.00	13.00	20.00	52.00	52.00	41.00	48.00	26.00	18.00	39.00	41.00	397.00
2014	Clear	5.00	7.00	0.00	12.00	13.00	41.00	48.00	116.00	91.00	33.00	0.00	0.00	366.00
	Cloudy	53.00	41.00	75.00	47.00	33.00	46.00	30.00	44.00	14.00	25.00	14.00	16.00	438.00
2015	Clear	9.00	0.00	0.00	0.00	6.00	66.00	41.00	135.00	58.00	6.00	0.00	0.00	321.00
	Cloudy	41.00	26.00	22.00	50.00	14.00	54.00	30.00	32.00	36.00	40.00	3.00	0.00	348.00
2016	Clear	0.00	0.00	1.00	45.00	35.00	90.00	89.00	86.00	27.00	11.00	4.00	1.00	389.00
	Cloudy	6.00	28.00	19.00	93.00	34.00	20.00	29.00	27.00	51.00	17.00	32.00	48.00	404.00
2017	Clear	0.00	0.00	4.00	0.00	9.00	85.00	108.00	88.00	141.00	18.00	17.00	0.00	470.00
	Cloudy	13.00	35.00	40.00	26.00	40.00	29.00	64.00	21.00	27.00	17.00	25.00	12.00	349.00
2018	Clear	0.00	3.00	10.00	10.00	55.00	12.00	105.00	55.00	34.00	1.00	0.00	1.00	286.00
	Cloudy	2.00	12.00	46.00	57.00	32.00	25.00	41.00	26.00	51.00	18.00	20.00	48.00	378.00
2019	Clear	16.00	9.00	0.00	19.00	39.00	75.00	120.00	58.00	24.00	37.00	0.00	2.00	399.00
	Cloudy	89.00	37.00	12.00	42.00	23.00	79.00	22.00	19.00	58.00	48.00	35.00	22.00	486.00
2020	Clear	17.00	0.00	0.00	37.00	115.00	36.00	103.00	167.00	48.00	5.00	0.00	0.00	528.00
	Cloudy	24.00	14.00	62.00	21.00	29.00	32.00	40.00	22.00	45.00	86.00	49.00	7.00	431.00
2021	Clear	0.00	3.00	3.00	31.00	42.00	58.00	157.00	87.00	8.00	0.00	0.00	0.00	389.00
	Cloudy	4.00	62.00	88.00	54.00	44.00	60.00	21.00	18.00	80.00	17.00	39.00	57.00	544.00
2022	Clear	0.00	0.00	0.00	21.00	48.00	85.00	113.00	61.00	45.00	2.00	0.00	18.00	393.00
	Cloudy	48.00	52.00	73.00	66.00	65.00	27.00	26.00	34.00	28.00	38.00	31.00	6.00	494.00
2023	Clear	0.00	0.00	0.00	1.00	46.00	160.00	69.00	122.00	48.00	3.00	33.00	0.00	482.00
	Cloudy	11.00	2.00	47.00	60.00	53.00	8.00	74.00	32.00	46.00	5.00	12.00	41.00	391.00
Average	Clear	2.12	1.72	1.64	14.68	45.64	69.04	98.28	98.56	41.72	10.24	3.40	1.52	388.56
	Cloudy	23.16	31.64	47.48	55.28	39.24	44.00	35.96	33.32	41.12	28.32	28.60	27.00	435.12

B. ADDITIONAL VERTICAL PROFILE VARIABLES

Figure 16 shows the variation in relative humidity (RH) between day and night. During the day, RH is consistently lower, particularly in the upper troposphere, due to heating and vertical mixing, which decrease atmospheric moisture. This low daytime RH is beneficial for astronomical observations, as it reduces water vapor, improving transparency. In contrast, at night, RH levels rise throughout the troposphere, especially near the surface, because of cooling. Higher nighttime RH can lead to dew formation, potentially harming observatory equipment, which may require protective measures such as dew shields or active heating systems.

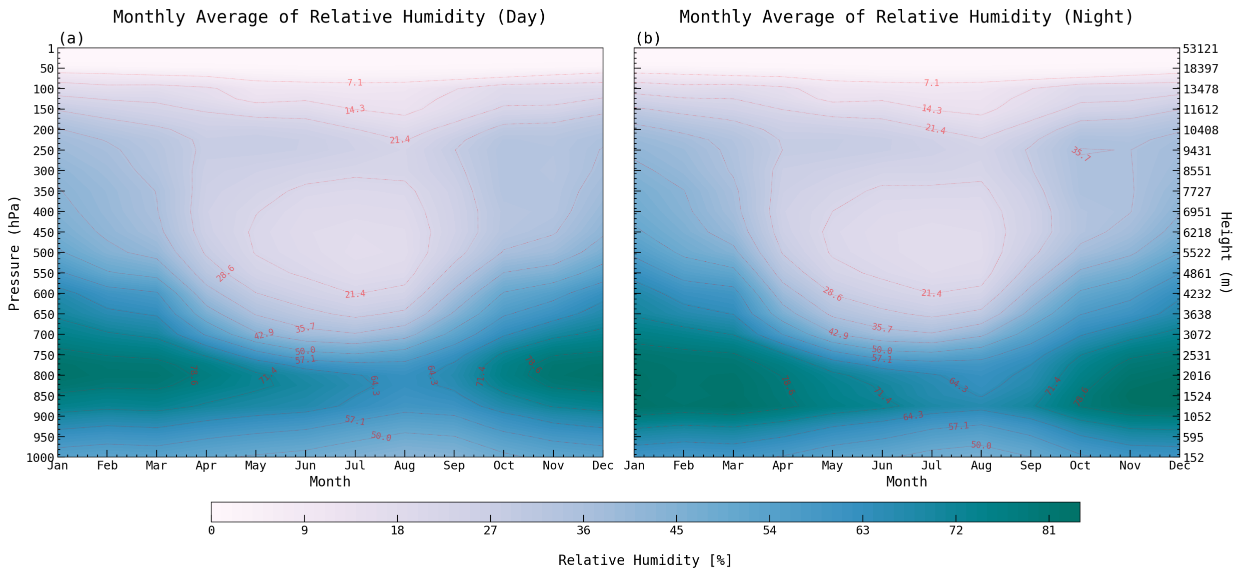

Figure 16. Comparison of Monthly Mean Relative Humidity between Daytime and Nocturnal Periods.

In Figure 17, the specific humidity is highest near the surface and decreases with altitude, varying seasonally. During DJF, cooler conditions lead to prolonged elevated surface humidity, while JJA reflects warmer, drier conditions, and the lowest surface humidity. MAM and SON are transitional periods with moderate humidity. The high surface humidity during DJF increases atmospheric water vapor, affecting observational clarity by absorbing infrared radiation and scattering visible light. Elevated nighttime humidity across all seasons increases the risk of dew formation in telescopes, requiring mitigation. JJA provides the best conditions for optical and infrared observations as a result of its lower humidity.

Figure 18, the variation in specific humidity at different altitudes and its impact on astronomical observations. During the day, humidity is lower because of heating and mixing, while at night, it rises because of cooling, especially near the surface. Seasonal patterns show that JJA has the lowest atmospheric water vapor, which is beneficial for infrared and optical astronomy, whereas DJF has higher surface humidity, posing challenges such as dew and frost for nighttime observations. Higher altitude observatories consistently experience low humidity, avoiding surface-level peaks. The best conditions for astronomical observations occur in the daytime and during JJA, while DJF and nighttime present more difficult conditions because of increased humidity and related effects.

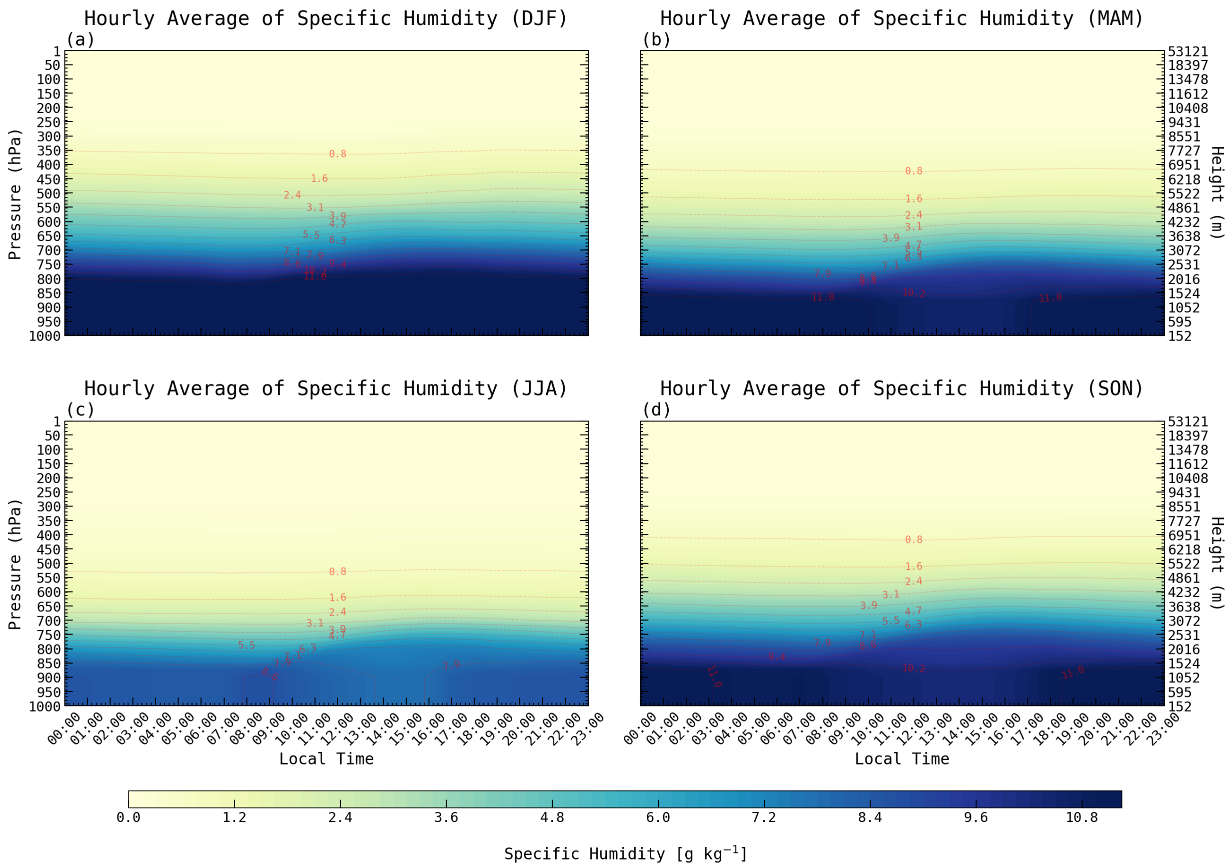

Figure 17. These panels illustrate diurnal (hourly) variations in specific humidity across different altitudes for each season.

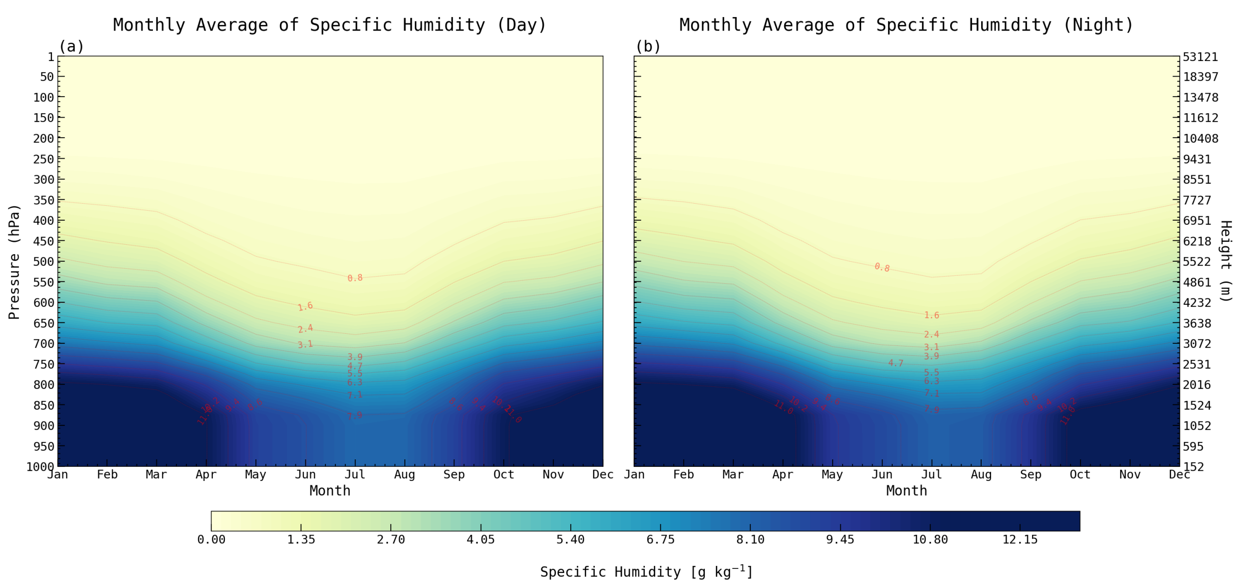

Figure 18. Comparison of Monthly Mean Specific Humidity between Daytime and Nocturnal Periods.

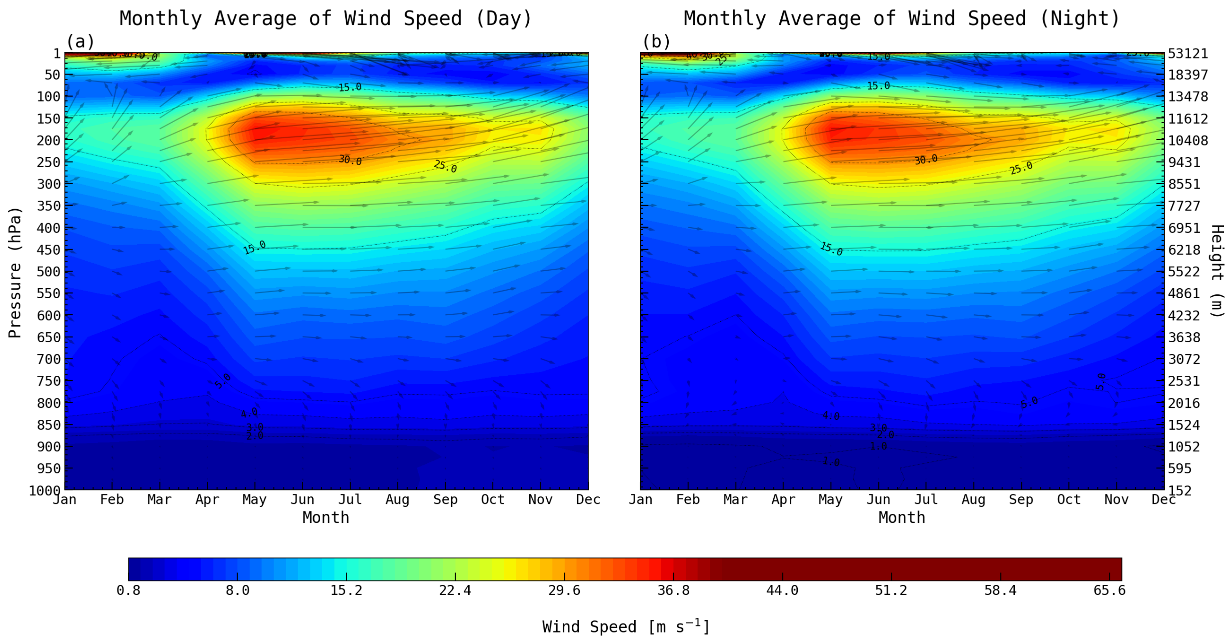

Figure 19. This graph presents the monthly average wind speed profiles for daytime (a) and nighttime (b) conditions, with pressure (hPa) and height (m) as vertical axes.

REFERENCES

Alliss, R. J., & Felton, B. D. 2009, in Proceedings of the Advanced Maui Optical and Space Surveillance Technologies Conference, E54

Arbeláez-Cardona, D., Silva-Villa, E., Galvez, J., Martínez, J. A., & Cuartas-Restrepo, P. 2020, International Journal of Remote Sensing, 41, 5103 , doi: 10.1080/01431161.2020.1727051

Barnett, V., & Lewis, T. 1994, Outliers in statistical data, Vol. 3 (New York: Wiley New York)

Bekhrad, P., Leitgeb, E., & Ivanov, H. 2023, Electronics, 13, 55, doi: 10.3390/electronics13010055

Bergman, J. 1997, Journal of Climate, 10, 2330, doi: 10.1175/1520-0442(1997)010⟨2330:ANIOCD⟩2.0.CO;2

Bi, C., Qing, C., Qian, X., et al. 2023, Monthly Notices of the Royal Astronomical Society. https://api.semanticscholar.org/CorpusID:265204529

Bolbasova, L. A., Shikhovtsev, A. Y., & Ermakov, S. A. 2023, Monthly Notices of the Royal Astronomical Society, 520, 4336

Bourscheidt, V., Junior, O. P., Naccarato, K., & Pinto, I. 2009, Atmospheric Research, 91, 508

Chun, M., Wilson, R., Avila, R., et al. 2009, Monthly Notices of the Royal Astronomical Society, 394, 1121

Colavita, M. M., Swain, M. R., Akeson, R. L., Koresko, C. D., & Hill, R. J. 2004, Publications of the Astronomical Society of the Pacific, 116, 876

Davies, R., & Kasper, M. 2012, Annual Review of Astronomy and Astrophysics, 50, 305–351, doi: 10.1146/annurev-astro-081811-125447

de la Cruz Rodriguez, J., Löfdahl, M. G., Sütterlin, P., Hillberg, T., & van der Voort, L. R. 2015, Astronomy & Astrophysics, 573, A40

Denker, C., Tritschler, A., Rimmele, T. R., et al. 2007, Publications of the Astronomical Society of the Pacific, 119, 170

Dutra, E., Muñoz-Sabater, J., Boussetta, S., et al. 2020, Earth and Space Science, 7, e2019EA000984, doi: 10.1029/2019EA000984

Dwivedi, Y. D., Nukala, V. B., Maddula, S. P., & Nair, K. 2021, Revista Brasileira de Meteorologia, 36, 63, doi: 10.1590/0102-77863540083

Dörnbrack, A., Bechtold, P., & Schumann, U. 2022, Journal of Geophysical Research: Atmospheres, 127, e2022JD036654, doi: 10.1029/2022JD036654

Erasmus, D. A., & Thompson, L. A. 1986, in SPIE Proceedings, Vol. 0628 (SPIE), 148–155, doi: 10.1117/12.963522

Galaktionov, I., Sheldakova, J., Samarkin, V., Toporovsky, V., & Kudryashov, A. 2023, in Photonics, Vol. 10, MDPI, 1147

García-Lorenzo, B., Eff-Darwich, A., Fuensalida, J., & Castro-Almazán, J. 2011, Monthly Notices of the Royal Astronomical Society, 414, 801

García-Díez, M., Fernández, J., Fita, L., & Yagüe, C. 2015, Quarterly Journal of the Royal Meteorological Society, 141, 2746, doi: 10.1002/qj.2561

Garratt, J. R. 1994, Earth-Science Reviews, 37, 89

Giono, G., Katsukawa, Y., Ishikawa, R., et al. 2015, in Space Science Symposium No. MSFC-E-DAA-TN20235

Giordano, C., Vernin, J., Muñoz-Tuñón, C., & Trinquet, H. 2014, in Observatory Operations: Strategies, Processes, and Systems V, Vol. 9149, SPIE, 166–173, doi: 10.1117/12.2056832

Giordano, C., Vernin, J., Ramió, H. V., et al. 2013, Monthly Notices of the Royal Astronomical Society, 430, 3102, doi: 10.1093/mnras/stt117

Gualtieri, G. 2021, Energies, 14, 4169

Gutiérrez, C., Molina, M., Ortega, M., López-Franca, N., & Sánchez, E. 2024, Climate Dynamics, 1

Hardy, J. W. 1998, Adaptive optics for astronomical telescopes, Vol. 16 (Oxford University Press, USA)

Haslebacher, C., Demory, M.-E., Demory, B.-O., Sarazin, M., & Vidale, P. L. 2022, Astronomy & amp; Astrophysics, 665, A149, doi: 10.1051/0004-6361/202142493

Hellemeier, J. A., Yang, R., Sarazin, M., & Hickson, P. 2019, Monthly Notices of the Royal Astronomical Society, 482, 4941

Hersbach, H., Bell, B., Berrisford, P., et al. 2020, Quarterly Journal of the Royal Meteorological Society, 146, 1999

Hidalgo, S. L., Muñoz-Tuñón, C., Castro-Almazán, J. A., & Varela, A. M. 2021, Publications of the Astronomical Society of the Pacific, 133, 105002

Iglesias, F. A., & Feller, A. 2019, Optical Engineering, 58, 082417

Jiménez-Esteve, B., & Domeisen, D. I. 2022, Quarterly Journal of the Royal Meteorological Society, 148, 2344, doi: https://doi.org/10.1002/qj.4306

Kalverla, P. C., Duncan Jr, J. B., Steeneveld, G.-J., & Holtslag, A. A. M. 2019, Wind Energy Science, 4, 193, doi: 10.5194/wes-4-193-2019

Kolmogorov, A. N. 1941, in Dokl. Akad. Nauk. SSSR, Vol. 32, 19–21

Kolmogorov, A. N., Levin, V., Hunt, J. C. R., Phillips, O. M., & Williams, D. 1991, Proceedings of the Royal Society of London. Series A: Mathematical and Physical Sciences, 434, 9, doi: 10.1098/rspa.1991.0075

Kovadlo, P. G., Lukin, V. P., & Shikhovtsev, A. Y. 2019, Atmospheric and Oceanic Optics, 32, 202, doi: 10.1134/S1024856019020076

Lagos-Zuniga, M., Balmaceda-Huarte, R., Regoto, P., et al. 2022, Climate Dynamics, 62, 4541

Lascaux, F., Masciadri, E., & Fini, L. 2013, Monthly Notices of the Royal Astronomical Society, 436, 3147, doi: 10.1093/mnras/stt1803

Lee, S.-H., Baek, J.-H., Moon, B.-K., et al. 2007, Journal of Astronomy and Space Sciences, 24, 339

Lei, Y., Letu, H., Shang, H., & Shi, J. 2020, Climate Dynamics, 54, 2941, doi: 10.1007/s00382-020-05149-x

Lombardi, G., Zitelli, V., & Ortolani, S. 2009, Monthly Notices of the Royal Astronomical Society, 399, 783

Lombardi, G., Zitelli, V., Ortolani, S., Pedani, M., & Ghedina, A. 2008, Astronomy &; Astrophysics, 483, 651–659, doi: 10.1051/0004-6361:20078372

Ma, B., Shang, Z., Hu, Y., et al. 2020, Nature, 583, 771

Machado, L. A., Calheiros, A. J., Biscaro, T., et al. 2018, Atmospheric Chemistry and Physics, 18, 6461

Mandat, D., Pech, M., Hrabovsky, M., et al. 2014, arXiv preprint arXiv:1402.4762

Masciadri, E., Lascaux, F., & Fini, L. 2013, Monthly Notices of the Royal Astronomical Society, 436, 1968, doi: 10.1093/mnras/stt1708

Maud, L. T., Tilanus, R. P. J., van Kempen, T. A., et al. 2017, A&A, 605, A121, doi: 10.1051/0004-6361/201731197

Minola, L., Zhang, G., Ou, T., et al. 2024, Climate Dynamics, 62, 933

Monin, A. S., & Obukhov, A. M. 1954, Contrib. Geophys. Inst. Acad. Sci. USSR, 151, e187

Musiolková, M., Huszár, P., Navrátil, M., & Špunda, V. 2021, Quarterly Journal of the Royal Meteorological Society, 147, 2834

Ningombam, S. S., Kathiravan, S., Parihar, P. S., et al. 2017, Experimental Astronomy, 43, 145, doi: 10.1007/s10686-017-9525-6

Noethe, L. 2002, in Progress in optics, Vol. 43 (Elsevier), 1–69

Nogueira, M., Soares, P. M. M., Tomé, R., & Miranda, P. M. A. 2021, Theoretical and Applied Climatology, 136, 347, doi: 10.1007/s00704-019-02918-9

Olauson, J. 2018, Renewable Energy, 126, 322, doi: 10.1016/j.renene.2018.03.056

Otárola, A., Travouillon, T., Schöck, M., et al. 2010, Publications of the Astronomical Society of the Pacific, 122, 470

Otarola, A., De Breuck, C., Travouillon, T., et al. 2019, Publications of the Astronomical Society of the Pacific, 131, 045001

Priyatikanto, R., Admiranto, A. G., Djamaluddin, T., Rachman, A., & Wijaya, D. 2024, Publications of the Astronomical Society of Australia, 41, e058

Qing, C., Wu, X., Li, X., et al. 2016, Optics Express, 24, 13303, doi: 10.1364/OE.24.013303

Quatresooz, F., Vanhoenacker-Janvier, D., & Oestges, C. 2023, Radio Science, 58, 1

Racine, R., & Ellerbroek, B. L. 1995, in SPIE Proceedings, Vol. 2534 (SPIE), 248–257, doi: 10.1117/12.217743

Radu, A., Angelescu, T., Curtef, V., et al. 2012, Monthly Notices of the Royal Astronomical Society, 422, 2262

Rimmele, T. R., & Marino, J. 2011, Living Reviews in Solar Physics, 8, 1

Rimmele, T. R., Warner, M., Keil, S. L., et al. 2020, Solar Physics, 295, 1

Sanchez-López, J. d. D., Arvizu, M. A., Mendieta, F. J., & Hipólito, I. N. 2011, Advanced Trends in Wireless Communications, 303

Sarazin, M., Melnick, J., Navarrete, J., & Lombardi, G. 2008, The Messenger, 132, 23

Schmidli, J. 2013, Journal of the atmospheric sciences, 70, 4041

Sharma, N. C., & Barnes, J. E. 2016, Aerosol and Air Quality Research, 16, 729–737, doi: 10.4209/aaqr.2015.05.0347

Shikhovtsev, A., Kovadlo, P., & Lukin, V. 2019, Atmosphere, 10, 499

Shikhovtsev, A. Y. 2024, Publications of the Astronomical Society of Japan, 76, 538

Shikhovtsev, A. Y., & Kovadlo, P. G. 2024, Applied Sciences, 14, 5439

Shikhovtsev, A. Y., Potanin, S. A., Kopylov, E. A., et al. 2024a, Atmosphere, 15, 1346

Shikhovtsev, A. Y., Qing, C., Kopylov, E. A., Potanin, S. A., & Kovadlo, P. G. 2024b, Remote Sensing, 16, 2102

Silva, J. V., de Castro, C. G. G., Passarelli, C., et al. 2020, Journal of Atmospheric and Solar-Terrestrial Physics, 199, 105214

Song, T., Cai, Z., Liu, Y., et al. 2020, Monthly Notices of the Royal Astronomical Society, 499, 1909

Sprung, D., & Sucher, E. 2013, in Remote Sensing of Clouds and the Atmosphere XVIII; and Optics in Atmospheric Propagation and Adaptive Systems XVI, Vol. 8890, SPIE, 321–329

Suo, C., Sun, A., Yan, C., et al. 2024, Atmosphere, 15, 1153

Tatarski, V. I. 2016, Wave propagation in a turbulent medium (Courier Dover Publications)

Tatarskii, V. I. 1971, Jerusalem: Israel Program for Scientific Translations, 1971

Thomas-Osip, J., McWilliam, A., Phillips, M., et al. 2007, Publications of the Astronomical Society of the Pacific, 119, 697

Tian, J., Deng, L., Zhang, X., et al. 2016, Publications of the Astronomical Society of the Pacific, 128, 105003

Tillayev, Y., Azimov, A., Ehgamberdiev, S., & Ilyasov, S. 2023, Atmosphere, doi: 10.3390/atmos14020199

Tokovinin, A. 2023, Atmosphere, 14, 1694

Travouillon, T., Ashley, M., Burton, M., Storey, J., & Loewenstein, R. 2003, Astronomy & Astrophysics, 400, 1163

Tung, K. K., & Orlando, W. W. 2003, Journal of the atmospheric sciences, 60, 824

Vernin, J., & Muñoz-Tuñón, C. 1992, Astronomy and Astrophysics (ISSN 0004-6361), vol. 257, no. 2, p. 811-816., 257, 811

Vicente-Serrano, S. M., Domínguez-Castro, F., Reig, F., et al. 2023, Geoscience Data Journal, 10, 505

Wang, Z., Zhang, L., Kong, L., et al. 2018, Monthly Notices of the Royal Astronomical Society, 478, 1459

Wynne, C., & Worswick, S. 1986, Monthly Notices of the Royal Astronomical Society, 220, 657

Ye, Q. 2010, Publications of the Astronomical Society of the Pacific, 123, 113 , doi: 10.1086/658201

Zanin, P. R., Pareja-Quispe, D., & Espinoza, J.-C. 2024, Agricultural and Forest Meteorology, 352, 110040

Zanin, P. R., & Satyamurty, P. 2021, Journal of Hydrometeorology, 22, 1609

Zhong, L., Zhang, L., Shi, Z., et al. 2020, Astronomy & Astrophysics, 637, A99

Zhu, L., Zhang, H., Sun, G., et al. 2023, Monthly Notices of the Royal Astronomical Society, 522, 1419

INSTITUTO NACIONAL DE PESQUISAS ESPACIAIS
Instituto Nacional de Pesquisas Espaciais
Coordenação-Geral de Engenharia, Tecnologia e Ciência Espaciais
Divisão de Clima Espacial

DECLARAÇÃO DE ENQUADRAMENTO AO ART. 2º, INC.I, DA LEI Nº 13.315/2016

Declaramos, para fins de enquadramento à Lei 13.315/2016, que dispõe sobre a incidência do Imposto sobre a Renda Retido na Fonte sobre remessas ao exterior de valores destinados, entre outros, de serviços, que o objeto a ser contratado, a saber, é a publicação do artigo científico intitulado "Assessment of Daytime Sky Quality and Atmospheric Refractive Index (C2n) Analysis at Pico dos Dias Observatory" de autoria de Luis Eduardo Antunes Vieira, implicará em pagamento pela prestação de serviço de natureza científica, não estando, portanto, sujeito à retenção na fonte do imposto sobre a renda, nos termos do art. 2º, inciso I, da supramencionada Lei:

"Art. 2º Não estão sujeitas à retenção na fonte do imposto sobre a renda:

I – as remessas destinadas ao exterior para fins educacionais, científicos ou culturais, inclusive para pagamento de taxas escolares, de taxas de inscrição em congressos, conclaves, seminários ou assemelhados e de taxas de exames de proficiência; e

(...)"

São José dos Campos, 01 de Setembro de 2025.

(Assinado Eletronicamente)

Luis Eduardo Antunes Vieira
Pesquisador
Divisão de Heliofísica,
Ciências Planetárias e Aeronomia
SIAPE 1177754

INSTITUTO NACIONAL DE PESQUISAS ESPACIAIS
Instituto Nacional de Pesquisas Espaciais
Coordenação-Geral de Engenharia, Tecnologia e Ciência Espaciais
Divisão de Clima Espacial

DECLARAÇÃO DE ARTIGO NÃO PUBLICADO

Declaro que o artigo científico "Assessment of Daytime Sky Quality and Atmospheric Refractive Index (C2n) Analysis at Pico dos Dias Observatory" foi submetido e aceito pela revista, e ainda não foi publicado. Esclareço que o artigo científico pode ser disponibilizado temporariamente em regime "Open Access" a critério exclusivo da Editora até que seja realizado o pagamento da taxa de publicação, quando então o referido artigo será efetivamente publicado segundo as políticas editoriais da Revista.

Atenciosamente,

(Assinado Eletronicamente)

Luis Eduardo Antunes Vieira
Pesquisador
Divisão de Heliofísica,
Ciências Planetárias e Aeronomia
SIAPE 1177754

INSTITUTO NACIONAL DE PESQUISAS ESPACIAIS

REQUISIÇÃO DE COMPRAS

REQUISIÇÃO DE COMPRAS		
Referência: DIHPA-017/2025-RC	**Processo SEI:** 01340.006530/2025-30	**Versão: 1**
Coordenação: CGCE	**Unidade:** DIHPA	**Sigla EDT:** ATDIHPA
Requisitante: Luis Eduardo Antunes Vieira	**Ramal:** 7851	**SIAPE:** 1177754
Resp/Fiscal do Contrato: Luis Eduardo Antunes Vieira	**Ramal:** 7851	**SIAPE:** 1177754
Gerente Téc:	**Ramal:**	**SIAPE:**
Resp/Fiscal do Contrato Substituto: Alisson Dal Lago	**Ramal:** 7808	**SIAPE:** 1466122

DESCRIÇÃO ORÇAMENTÁRIA					
Valor Total Estimado R$ 15.123,02	**PTRES** 233467	**PI** 955656-PO09	**Fonte** 1000	**Natureza da Despesa** 339039	**Item de despesa** 266

Item	**Código**	**Descrição do Material**	**Subitem**	**Unidade**	**Quant.**	**Valor Unitário (R$)**
1	13141	PUBLICAÇÃO DE ARTIGO CIENTÍFICO EM REVISTA INTERNACIONAL E NACIONAL .	92	SV	1.00	R$ 15.123,02

Possíveis Fornecedores	**Finalidade**	**Observações**
	Pagamento de Artigo Científico:	

	"Assessment of Daytime Sky Quality and Atmospheric Refractive Index (C2n) Analysis at Pico dos Dias Observatory."	

ASSINATURAS ELETRÔNICAS	
Aprovação - Titular Imediato: Alisson Dal Lago **SIAPE:** 1466122	**Aprovação - Titular Nível A:** Joaquim Eduardo Rezende Costa **SIAPE:** 0664811
Autorização - Responsável pelo Plano Orçamentário: Alisson Dal Lago **SIAPE:** 1466122	**Há Disponibilidade Orçamentária - SEPOR** (Vide assinatura eletrônica)
O conteúdo deste documento foi gerado no SIPLAN em 18/09/2025 às 14:58:03	

Documento assinado eletronicamente por **Alisson Dal Lago**, **Chefe da Divisão de Heliofísica, Ciências Planetárias e Aeronomia**, em 18/09/2025, às 15:04 (horário oficial de Brasília), com fundamento no § 3º do art. 4º do Decreto nº 10.543, de 13 de novembro de 2020.

Documento assinado eletronicamente por **Joaquim Eduardo Rezende Costa**, **Coordenador-Geral de Engenharia, Tecnologia e Ciência Espaciais substituto**, em 18/09/2025, às 15:12 (horário oficial de Brasília), com fundamento no § 3º do art. 4º do Decreto nº 10.543, de 13 de novembro de 2020.

Documento assinado eletronicamente por **Marcela de Fátima Nascimento de Macedo Torres**, **Analista em Ciência e Tecnologia**, em 18/09/2025, às 15:37 (horário oficial de Brasília), com fundamento no § 3º do art. 4º do Decreto nº 10.543, de 13 de novembro de 2020.

A autenticidade deste documento pode ser conferida no site https://sei.mcti.gov.br/verifica.html, informando o código verificador **13100660** e o código CRC **BF77C2EA**.

IOP Publishing | No.2 The Distillery, Glassfields, Avon Street, Bristol BS2 0GR, UK
Tel +44 (0)117 929 7481 **ioppublishing.org**

Ministério da Ciência, Tecnologia e Inovação (MCTI)
Instituto Nacional de Pesquisas Espaciais (INPE)
Dr. Luis Eduardo Antunes Vieira

Dear Dr. Luis Eduardo Antunes Vieira,

Title: Assessment of Daytime Sky Quality and Atmospheric Refractive Index (C$_n^2$) Analysis at Pico dos Dias Observatory

We are pleased that the manuscript above has been accepted for publication in The Astrophysical Journal Supplement Series. Please contact the IOP office, (email: apjproduction@ioppublishing.org), for any questions or problems that may arise during the production process.

This article, and all articles published in the Astrophysical Journal Supplement Series, is going to be published Open Access (OA).

The cost associated with your article is **$2,441.69**. IOP's DUN number is 217408160.

Sincerely,

Abby Carson (she/her/hers)

Publisher, Partner Publishing

IOP Publishing, Inc.
190 N Independence Mall West
Suite 601
Philadelphia, PA 19106

Abby.Carson@ioppublishing.org

MINISTÉRIO DA CIÊNCIA, TECNOLOGIA E INOVAÇÃO

INSTITUTO NACIONAL DE PESQUISAS ESPACIAIS
Avenida dos Astronautas, 1758, - Bairro Jardim da Granja,
CEP 12227-010, São José dos Campos - SP - http://www.inpe.br/

ANEXO ESTIMATIVA DE CUSTOS 051B/2025-S

FORNECEDOR:	IOP Publishing		
OBJETO:	Serviço de Publicação de Artigo	**EMITIDA POR:**	IMPEX - Importação & Exportação / SECRI
REQUISITANTE:	Dr. Luis Eduardo Antunes Vieira	**RAMAL:**	6115

CUSTOS FINANCEIROS INDIRETOS	**VALOR TOTAL DOS SERVIÇOS EM USD**	**VALOR UNITÁRIO DESPESAS EXTERNAS POR EVENTO EM USD**	**VALOR UNITÁRIO COMISSÃO BANCÁRIA POR EVENTO EM REAIS**	**QUANTIDADE DE SERVIÇOS/EVENTOS**	**VALOR EM REAIS**
Valor do serviço a ser contratado	USD 2,441.69	-	-	1,00	R$ 15.123,02
Emissão do Contrato de Câmbio do Banco do Brasil	-	-	-	-	R$ 0,00
Despesas bancárias no Exterior (Valor em USD E EUR ISENTO)	USD 0,00	-	R$ 0,00	1,00	R$ 0,00
				VALOR TOTAL DO PROCESSO	**R$ 15.123,02**

Haverá isenção do Imposto de Renda sobre remessa financeira ao Exterior para pagamento de serviços caso haja no processo declaração de enquadramento à Lei 13.315/2016, artigo 2º, inciso I, por tratar-se as remessas de serviços destinados a fins educacionais ou científicos.

Taxa Ptax Venda USD Bacen 11/09/2025	**5,3858**	**Taxa utilizada: Ptax USD Venda Bacen + 15% = 6,19367**	**SEI n°** 01340.006530/2025-30
EMITIR RC NO VALOR DE:		**R$ 15.123,02**	

IMPORTANTE:

1) O valor da REQUISIÇÃO DE COMPRA deverá ser o valor total do serviço a ser contratado.

2) O valor total das despesas bancárias é equivalente a **R$ 0,00** - Emissão do Contrato de Câmbio Banco do Brasil.

3) O INPE não efetua pagamento antecipado.

4) Certifique-se de que a Proforma/cotação é do exportador no exterior e não do representante no Brasil.

5) Proforma/Cotação deve conter: Dados do exportador, valor total, forma de pagamento e dados bancários para pagamento.

6) Todos os valores a serem pagos devem estar na Proforma ou Invoice, inclusive taxas bancárias.

7) Para remessas financeiras ao Exterior para pagamento de serviços, haverá retenção de IR (Decreto 3.000/99, art. 685, II, alínea "a" E IN 1.455/14, artigo 16), exceto se houver, no processo, declaração de enquadramento à Lei 13.315/2016, artigo 2º, inciso I, assinada pelo requisitante/responsável, por tratar-se de aquisição de serviços destinados a fins educacionais ou científicos.

8) Caso a prestação de serviço não seja de natureza educacional ou científica haverá a necessidade de incluir no processo a declaração de não enquadramento e informar ao beneficiário que haverá retenção de imposto de renda para sua ciência e verificação se isto onerará o valor de sua proposta - a área de Importação e Exportação poderá efetuar o cálculos do imposto de renda caso solicitado.

INSTITUTO NACIONAL DE PESQUISAS ESPACIAIS
Instituto Nacional de Pesquisas Espaciais
Coordenação-Geral de Gestão Organizacional
Coordenação de Administração
Serviço de Compras, Recebimento e Importação
Grupo de Instrução Processual

Memorando nº 13069/2025/INPE

Ao Senhor Amarildo José Pereira - SECAC

Assunto: Publicação de Artigo Científico

Considerando a dúvida exarada quanto à correta instrução para o prosseguimento da Requisição de Compras nº DIHPA-017/2025 (Publicação de Artigo Científico), solicitamos desse Setor de Capacitação por Competências - SECAC, análise e manifestação quanto ao referido objeto, se será atendido através do formulário INPE-012 - "Solicitação de Capacitação" ou por via de Requisição de Compras ora apresentada nos autos.

Atenciosamente,

(assinado eletronicamente)
José Aristeu de Souza Ruas
Chefe do Serviço de Compras, Recebimento e Importação - SECRI
SIAPE 664036

Anexos

Não Possui.

INSTITUTO NACIONAL DE PESQUISAS ESPACIAIS
Instituto Nacional de Pesquisas Espaciais
Coordenação de Ensino, Pesquisa e Extensão
Divisão de Extensão e Capacitação
Setor de Capacitação por Competências

Memorando nº 13109/2025/INPE

São José dos Campos, 19 de setembro de 2025

Ao Senhor Chefe do Serviço de Compras, Recebimento e Importação - SECRI

Assunto: Publicação de Artigo Científico

Em atenção ao Memorando nº 13069/2025/INPE (SEI nº 13156344), após analise dos documentos do processo 01340.006530/2025-30, este Setor de Capacitação por Competências constatou que não se trata de inscrição em evento no qual dá direito à publicação de artigo. Trata-se somente do pagamento de publicação de artigo científico, podendo ser atendido via Requisição de Compras **DIHPA-017/2025-RC** (SEI nº 13100660).

Atenciosamente,

(assinado eletronicamente)

Amarildo José Pereira
Chefe do Setor de Capacitação por Competências - SECAC
SIAPE 0673265

Anexos

Não Possui.

INSTITUTO NACIONAL DE PESQUISAS ESPACIAIS

JUSTIFICATIVA

AUTORIZAÇÃO DE AVISO DE CONTRATAÇÃO

(art. 72, inciso VIII, da Lei nº 14.133/2021)

Aviso de Contratação nº: 64/2025
Processo nº: 01340.006530/2025-30
Objeto: PUBLICAÇÃO DO ARTIGO CIENTÍFICO INTITULADO: "ASSESSMENT OF DAYTIME SKY QUALITY AND ATMOSPHERIC REFRACTIVE INDEX (C2n) ANALYSIS AT PICO DOS DIAS OBSERVATORY

No uso das atribuições que me foram subdelegadas pelo inciso III, do art. 1º, da Portaria nº 1639/2025/SEI-INPE (SEI nº 13157577), e após a análise da documentação que instrui o presente processo, **AUTORIZO** a contratação do objeto em epígrafe por meio da Dispensa Eletrônica nº 90106/2025, com fulcro no inciso II, do art. 75, da Lei nº 14.133/2021.

Valor estimado da contratação: R$ 15.123,02 (quinze mil e cento e vinte e três reais e dois centavos).

Ao Serviço de Compras, Recebimento e Importação - SECRI, para as providências de divulgação do referido Aviso, em cumprimento ao disposto no parágrafo único, do art. 72, da Lei nº 14.133/2021.

(assinado eletronicamente)
Raul Ferreira da Silva Junior
Ordenador de Despesas
SIAPE 2796948

INSTITUTO NACIONAL DE PESQUISAS ESPACIAIS
Instituto Nacional de Pesquisas Espaciais
Coordenação-Geral de Gestão Organizacional
Coordenação de Administração
Serviço de Compras, Recebimento e Importação
Grupo Permanente de Pregão Eletrônico

Memorando nº 13689/2025/INPE

São José dos Campos, 01 de outubro de 2025

Ao Senhor Luis Eduardo Antunes Vieira

Assunto: **Elaboração de novo DFD e Alteração do Termo de Referência**

Prezado, considerando que o Identificador da futura contratação (240106-227/2025), consoante Formulário - Condições de Fornecimento SEI n° 13100655, já foi utilizado no processo SEI n° 01340.003681/2025-36 e que o sistema de divulgação não permite a utilização deste número por mais de uma vez, solicito por gentileza, a elaboração de novo Documento de Formalização de Demanda, no sistema PGC do compras.gov.br, para esta compra, bem como a alteração/correção do Formulário - Condições de Fornecimento em seu item 5., para que possamos dar continuidade ao processo.

Atenciosamente,

(assinado eletronicamente)
Sueli Ribeiro Martins
Assistente em Ciência e Tecnologia
SIAPE 3271224

Anexos e Minutas

Não Possui.

CONDIÇÕES DE FORNECIMENTO

1. OBJETO

Publicação do artigo científico "Assessment of Daytime Sky Quality and Atmospheric Refractive Index (C2n) Analysis at Pico dos Dias Observatory."

2. OBJETIVO

Divulgação de trabalhos científicos da Divisão de Heliofísica, Ciências Planetárias e Aeronomia - DIHPA.

3. JUSTIFICATIVA

A requisição de compra mencionada trata-se do pagamento de publicação do artigo científico intitulado "Assessment of Daytime Sky Quality and Atmospheric Refractive Index (C2n) Analysis at Pico dos Dias Observatory", de autoria de Luis Eduardo Antunes Vieira, na revista Astrophysical Journal Supplement.

Considerando que a obra é resultado de trabalho de pesquisa, registramos a importância da publicação que será veiculada no meio científico nacional e internacional, cumprindo assim nossa missão institucional que é gerar e transmitir conhecimento técnico e científico de alta qualidade em sensoriamento remoto e suas aplicações em benefício da sociedade.

4. FORMA DE PAGAMENTO

100% após a execução dos serviços.

5. PREVISÃO NO PLANO DE CONTRATAÇÕES ANUAL

O objeto da contratação está previsto no Plano de Contratações Anual 2025, conforme detalhamento a seguir:

ID PCA no PNCP: 01263896000164-0-000008/2025;

Data de publicação no PNCP: 10/05/2024;

Id do item no PCA: 963;

Classe/Grupo: 891 - SERVIÇOS DE REPRODUÇÃO, PUBLICAÇÃO E IMPRESSÃO;

Identificador da Futura Contratação: 240106-256/2025;

Elaborado por:

(Assinado Eletronicamente)

Luis Eduardo Antunes Vieira
Pesquisador
Divisão de Heliofísica,
Ciências Planetárias e Aeronomia
SIAPE 1177754

Revisado por:

(Assinado Eletronicamente)

Alisson Dal Lago
Chefe da Divisão de Heliofísica,
Ciências Planetárias e Aeronomia
SIAPE 1466122

Aprovado por:

(Assinado Eletronicamente)

Adenilson Roberto da Silva
Coordenador-Geral de Engenharia,
Tecnologia e Ciência Espaciais
SIAPE 1356765

Documento assinado eletronicamente por **Luis Eduardo Antunes Vieira**, **Pesquisador**, em 01/10/2025, às 16:25 (horário oficial de Brasília), com fundamento no § 3º do art. 4º do Decreto nº 10.543, de 13 de novembro de 2020.

Documento assinado eletronicamente por **Alisson Dal Lago**, **Chefe da Divisão de Heliofísica, Ciências Planetárias e Aeronomia**, em 01/10/2025, às 17:12 (horário oficial de Brasília), com fundamento no § 3º do art. 4º do Decreto nº 10.543, de 13 de novembro de 2020.

Documento assinado eletronicamente por **Adenilson Roberto da Silva**, **Coordenador-Geral de Engenharia e Tecnologia e Ciência Espaciais**, em 02/10/2025, às 10:04 (horário oficial de Brasília), com fundamento no § 3º do art. 4º do Decreto nº 10.543, de 13 de novembro de 2020.

A autenticidade deste documento pode ser conferida no site https://sei.mcti.gov.br/verifica.html, informando o código verificador **13191591** e o código CRC **AA488F0C**.

INSTIT.NAC.DE PESQ.ESPACIAIS-S.J.CAMPOS - MCT

Aviso de Contratação 64/2025

Informações Básicas

Número do artefato	UASG	Editado por	Atualizado em
64/2025	240106-INSTIT.NAC.DE PESQ.ESPACIAIS-S.J.CAMPOS - MCT	JOSE ARISTEU DE SOUZA RUAS	02/10/2025 10:35 (v 0.5)

Status

ASSINADO

Outras informações

Categoria	Número da Contratação	Processo Administrativo
V - prestação de serviços, inclusive os técnico-profissionais especializados/Trabalho técnico, científico ou artístico		01340.006530/2025-30

1. <Item editável>

AVISO DE CONTRATAÇÃO DIRETA

90106/2025

CONTRATANTE (UASG)

INSTITUTO NACIONAL DE PESQUISAS ESPACIAIS (240106)

OBJETO

Publicação do artigo científico “Assessment of Daytime Sky Quality and Atmospheric Refractive Index (C2n) Analysis at Pico dos Dias Observatory.”

VALOR TOTAL DA CONTRATAÇÃO

R$ 15.123,02

DATA DA SESSÃO PÚBLICA

De 02/10/2025

HORÁRIO DA FASE DE LANCES

Sem disputa

CRITÉRIO DE JULGAMENTO:

Menor preço por item

TRATAMENTO FAVORECIDO ME/EPP/EQUIPARADAS
NÃO

MARGEM DE PREFERÊNCIA PARA ALGUM ITEM

NÃO

MINISTÉRIO DA CIÊNCIA, TECNOLOGIA E INOVAÇÃO - MCTI

INSTITUTO NACIONAL DE PESQUISAS ESPACIAIS - INPE

AVISO DE CONTRATAÇÃO DIRETA Nº 90106/2025

(Processo Administrativo nº 01340.006530/2025-30)

Torna-se público que o **MINISTÉRIO DA CIÊNCIA, TECNOLOGIA E INOVAÇÃO - MCTI**, por meio do **INSTITUTO NACIONAL DE PESQUISAS ESPACIAIS - INPE**, sediado na Avenida dos Astronautas n° 1758, Jardim da Granja, CEP 12.227-010, realizará Dispensa Eletrônica com critério de julgamento menor preço, na hipótese do art. 75, inciso II, nos termos da Lei nº 14.133, de 1º de abril de 2021, da Instrução Normativa SEGES/ME nº 67, de 8 de julho de 2021, e demais normas aplicáveis.

1. DO OBJETO

1.1. O objeto do presente procedimento é a escolha da proposta mais vantajosa para a contratação, por dispensa de licitação, de Publicação do artigo científico "Assessment of Daytime Sky Quality and Atmospheric Refractive Index (C2n) Analysis at Pico dos Dias Observatory.", conforme condições, quantidades e exigências estabelecidas neste Aviso de Contratação Direta e seus anexos.

1.1.1. Havendo mais de um item, faculta-se ao fornecedor a participação em quantos forem de seu interesse.

1.2. O critério de julgamento adotado será o **menor preço**, observadas as exigências contidas neste Aviso de Contratação Direta e seus Anexos quanto às especificações do objeto.

2. DO REGISTRO DE PREÇOS

2.1 Não se Aplica.

3. DA PARTICIPAÇÃO NA DISPENSA ELETRÔNICA

3.1. A participação na presente dispensa eletrônica ocorrerá por meio do Sistema de Dispensa Eletrônica, ferramenta informatizada integrante do Sistema de Compras do Governo Federal – Compras.gov.br, disponível no Portal de Compras do Governo Federal, no endereço eletrônico www.gov.br/compras.

3.1.1. O procedimento será divulgado no Compras.gov.br e no Portal Nacional de Contratações Públicas - PNCP, e encaminhado automaticamente aos fornecedores registrados no Sistema de Cadastramento Unificado de Fornecedores - Sicaf, por mensagem eletrônica, na correspondente linha de fornecimento que pretende atender.

3.1.2. O Compras.gov.br poderá ser acessado pela web ou pelo aplicativo Compras.gov.br.

3.1.3. O fornecedor é o responsável por qualquer transação efetuada diretamente ou por seu representante no Sistema de Dispensa Eletrônica, não cabendo ao provedor do Sistema ou ao órgão entidade promotor do procedimento a responsabilidade por eventuais danos decorrentes de uso indevido da senha, ainda que por terceiros não autorizados.

3.2. Não poderão participar desta dispensa de licitação:

3.2.1 aquele que não atenda às condições deste Aviso de Contratação Direta e seu(s) anexo(s);

3.2.2. sociedade que desempenhe atividade incompatível com o objeto da dispensa;

3.2.3. empresas estrangeiras que não tenham representação legal no Brasil com poderes expressos para receber citação e responder administrativa ou judicialmente;

3.2.4. autor do anteprojeto, do projeto básico ou do projeto executivo, pessoa física ou jurídica, quando a contratação versar sobre obra, serviços ou fornecimento de bens a ele relacionados;

3.2.5. empresa, isoladamente ou em consórcio, responsável pela elaboração do projeto básico ou do projeto executivo, ou empresa da qual o autor do projeto seja dirigente, gerente, controlador, acionista ou detentor de mais de 5% (cinco por cento) do capital com direito a voto, responsável técnico ou subcontratado, quando a contratação versar sobre obra, serviços ou fornecimento de bens a ela necessários;

3.2.6. pessoa física ou jurídica que se encontre, ao tempo da contratação, impossibilitada de contratar em decorrência de sanção que lhe foi imposta;

3.2.7. aquele que mantenha vínculo de natureza técnica, comercial, econômica, financeira, trabalhista ou civil com dirigente do órgão ou entidade contratante ou com agente público que desempenhe função na dispensa de licitação ou atue na fiscalização ou na gestão do contrato, ou que deles seja cônjuge, companheiro ou parente em linha reta, colateral ou por afinidade, até o terceiro grau;

3.2.8. empresas controladoras, controladas ou coligadas, nos termos da Lei nº 6.404, de 15 de dezembro de 1976, concorrendo entre si;

3.2.9. pessoa física ou jurídica que, nos 5 (cinco) anos anteriores à divulgação do aviso, tenha sido condenada judicialmente, com trânsito em julgado, por exploração de trabalho infantil, por submissão de trabalhadores a condições análogas às de escravo ou por contratação de adolescentes nos casos vedados pela legislação trabalhista;

3.2.10. pessoas jurídicas reunidas em consórcio;

3.2.11. Organização da Sociedade Civil de Interesse Público - OSCIP, atuando nessa condição.

3.2.12. sociedades cooperativas.

3.3. Não poderá participar, direta ou indiretamente, da dispensa eletrônica ou da execução do contrato agente público do órgão ou entidade contratante, devendo ser observadas as situações que possam configurar conflito de interesses no exercício ou após o exercício do cargo ou emprego, nos termos da legislação que disciplina a matéria, conforme § 1º do art. 9º da Lei n.º 14.133, de 2021.

3.4. O impedimento de que trata o item 3.3.6 aplica-se também ao fornecedor que atue em substituição a outra pessoa, física ou jurídica, com o intuito de burlar a efetividade da sanção a ela aplicada, inclusive a sua controladora, controlada ou coligada, desde que devidamente comprovado o ilícito ou a utilização fraudulenta da personalidade jurídica do fornecedor.

3.5. A critério da Administração e exclusivamente a seu serviço, o autor dos projetos e a empresa a que se referem os itens 3.2.4 e 3.2.5 poderão participar no apoio das atividades de planejamento da contratação, de execução da dispensa ou de gestão do contrato, desde que sob supervisão exclusiva de agentes públicos do órgão ou entidade.

3.6. Equiparam-se aos autores do projeto as empresas integrantes do mesmo grupo econômico.

3.7. O disposto nos itens 3.2.4 e 3.2.5 não impede a dispensa ou a contratação de serviço que inclua como encargo do contratado a elaboração do projeto básico e do projeto executivo, nas contratações integradas, e do projeto executivo, nos demais regimes de execução.

3.8. Em dispensas e contratações realizadas no âmbito de projetos e programas parcialmente financiados por agência oficial de cooperação estrangeira ou por organismo financeiro internacional com recursos do financiamento ou da contrapartida nacional, não poderá participar pessoa física ou jurídica que integre o rol de pessoas sancionadas por essas entidades ou que seja declarada inidônea nos termos da Lei nº 14.133, de 2021.

3.9. A vedação de que trata o item 3.4, estende-se a terceiro que auxilie a condução da contratação na qualidade de integrante de equipe de apoio, profissional especializado ou funcionário ou representante de empresa que preste assessoria técnica.

4. DO INGRESSO NA DISPENSA ELETRÔNICA E DO CADASTRAMENTO DA PROPOSTA INICIAL

4.1. O ingresso do fornecedor na disputa da dispensa eletrônica ocorrerá com o cadastramento de sua proposta inicial, na forma deste item.

4.2, O fornecedor interessado, após a divulgação do Aviso de Contratação Direta, encaminhará, exclusivamente por meio do Sistema de Dispensa Eletrônica, a proposta com a descrição do objeto ofertado, a marca do produto, quando for o caso, e o preço ou o desconto, até a data e o horário estabelecidos para abertura do procedimento.

4.3. Todas as especificações do objeto contidas na proposta, em especial o preço ou o desconto ofertado, vinculam a Contratada.

4.4. Nos valores propostos estarão inclusos todos os custos operacionais, encargos previdenciários, trabalhistas, tributários, comerciais e quaisquer outros que incidam direta ou indiretamente na execução do objeto.

> 4.4.1. A proposta deverá conter declaração de que compreende a integralidade dos custos para atendimento dos direitos trabalhistas assegurados na Constituição Federal, nas leis trabalhistas, nas normas infralegais, nas convenções coletivas de trabalho e nos termos de ajustamento de conduta vigentes na data de entrega das propostas.
>
> 4.4.2. Os preços ofertados, tanto na proposta inicial, quanto na etapa de lances, serão de exclusiva responsabilidade do fornecedor, não lhe assistindo o direito de pleitear qualquer alteração, sob alegação de erro, omissão ou qualquer outro pretexto.

4.5. Se o regime tributário da empresa implicar o recolhimento de tributos em percentuais variáveis, a cotação adequada será aquela correspondente à média dos efetivos recolhimentos da empresa nos últimos doze meses.

4.6. Independentemente do percentual do tributo que constar da planilha, no pagamento serão retidos na fonte os percentuais estabelecidos pela legislação vigente.

4.7. A apresentação das propostas implica obrigatoriedade do cumprimento das disposições nelas contidas, em conformidade com o que dispõe o Termo de Referência, assumindo o proponente o compromisso de executar os serviços nos seus termos, bem como de fornecer os materiais, equipamentos, ferramentas e utensílios necessários, em quantidades e qualidades adequadas à perfeita execução contratual, promovendo, quando requerido, sua substituição.

4.8. O prazo de validade da proposta não será inferior a **60** (**sessenta**) **dias,** a contar da data de sua apresentação.

4.9. No cadastramento da proposta inicial, o fornecedor deverá, também, assinalar Termo de Aceitação, em campo próprio do sistema eletrônico, relativo às seguintes declarações:

4.9.1. que inexistem fatos impeditivos para sua habilitação no certame, ciente da obrigatoriedade de declarar ocorrências posteriores;

4.9.2. que está ciente e concorda com as condições contidas no Aviso de Contratação Direta e seus anexos;

4.9.3. que se responsabiliza pelas transações que forem efetuadas no sistema, assumindo-as como firmes e verdadeiras;

4.9.4. que cumpre as exigências de reserva de cargos para pessoa com deficiência e para reabilitado da Previdência Social, previstas em lei e em outras normas específicas;

4.9.5. que não emprega menor de 18 anos em trabalho noturno, perigoso ou insalubre e não emprega menor de 16 anos, salvo menor, a partir de 14 anos, na condição de aprendiz, nos termos do art. 7°, inciso XXXIII, da Constituição; e

4.9.6. não possui empregados executando trabalho degradante ou forçado, observando o disposto nos incisos III e IV do art. 1º e no inciso III do art. 5º da Constituição Federal.

4.10. . O fornecedor organizado em cooperativa deverá declarar, ainda, em campo próprio do sistema eletrônico, que cumpre os requisitos estabelecidos no art. 16 da Lei nº 14.133, de 2021.

4.11. O fornecedor deverá declarar em campo próprio do sistema se o produto ou serviço ofertado é manufaturado nacional beneficiado por um dos critérios de margem de preferência indicados no Termo de Referência, quando for o caso, para usufruir do benefício.

4.12. O fornecedor enquadrado como microempresa, empresa de pequeno porte ou sociedade cooperativa deverá declarar, ainda, em campo próprio do sistema eletrônico, que cumpre os requisitos estabelecidos no art. 3° da Lei Complementar nº 123, de 2006, estando apto a usufruir do tratamento favorecido estabelecido em seus arts. 42 a 49, observado o disposto nos §§ 1º ao 3º do art. 4º, da Lei n.º 14.133, de 2021.

5. DA FASE DE LANCES

5.1. A partir da data e horário estabelecidos neste Aviso de Contratação Direta, a sessão pública será automaticamente aberta pelo sistema para o envio de lances públicos e sucessivos, exclusivamente por meio do sistema eletrônico, sendo encerrado no horário de finalização de lances também já previsto neste Aviso.

5.2. Iniciada a etapa competitiva, os fornecedores deverão encaminhar lances exclusivamente por meio de sistema eletrônico, sendo imediatamente informados do seu recebimento e do valor consignado no registro.

5.2.1. O lance deverá ser ofertado pelo **valor unitário** do item.

5.3. O fornecedor somente poderá oferecer valor inferior ou percentual de desconto superior ao último lance por ele ofertado e registrado pelo sistema.

5.3.1. O fornecedor poderá oferecer lances sucessivos iguais ou superiores ao lance que esteja vencendo o certame, desde que inferiores ao menor por ele ofertado e registrado pelo sistema, sendo tais lances definidos como “lances intermediários” para os fins deste Aviso de Contratação Direta.

5.3.2. O intervalo mínimo de diferença de valores ou percentuais entre os lances, que incidirá tanto em relação aos lances intermediários quanto em relação ao que cobrir a melhor oferta é de **0,5%** (**meio por cento**).

5.4. Havendo lances iguais ao menor já ofertado, prevalecerá aquele que for recebido e registrado primeiro no sistema.

5.5. Caso o fornecedor não apresente lances, concorrerá com o valor de sua proposta.

5.6. Durante o procedimento, os fornecedores serão informados, em tempo real, do valor do menor lance ou do maior desconto registrado, vedada a identificação do fornecedor.

5.7. Imediatamente após o término do prazo estabelecido para a fase de lances, haverá o seu encerramento, com o ordenamento e divulgação dos lances, pelo sistema, em ordem crescente de classificação.

5.7.1 O encerramento da fase de lances ocorrerá de forma automática pontualmente no horário indicado, sem qualquer possibilidade de prorrogação e não havendo tempo aleatório ou mecanismo similar.

6. DA FASE DE JULGAMENTO E ACEITAÇÃO DAS PROPOSTAS

6.1. Encerrada a fase de lances, quando a proposta do primeiro colocado permanecer acima do preço máximo ou abaixo do desconto definido para a contratação, o gestor poderá negociar condições mais vantajosas.

6.1.1. Neste caso, será encaminhada contraproposta ao fornecedor que tenha apresentado o menor preço ou o maior desconto, para que seja obtida a melhor proposta compatível em relação ao estipulado pela Administração.

6.1.2. A negociação poderá ser feita com os demais fornecedores classificados, exclusivamente por meio do sistema, respeitada a ordem de classificação, quando o primeiro colocado, mesmo após a negociação, for desclassificado em razão de sua proposta permanecer acima do preço máximo ou abaixo do desconto definido para a contratação.

6.2. Em qualquer caso, concluída a negociação, se houver, o resultado será divulgado a todos e registrado na ata do procedimento da dispensa eletrônica, devendo esta ser anexada aos autos do processo de contratação.

6.3. Constatada a compatibilidade entre o valor da proposta e o estipulado para a contratação, será solicitado ao fornecedor o envio da proposta adequada ao último lance ofertado ou ao valor negociado, se for o caso, acompanhada dos documentos complementares, quando necessários.

6.4. Encerrada a etapa de negociação, se houver, o gestor verificará se o fornecedor provisoriamente classificado em primeiro lugar atende às condições de participação no certame, conforme previsto no art. 14 da Lei nº 14.133, de 2021, legislação correlata e nos itens 3.2 e seguintes deste Aviso, especialmente quanto à existência de sanção que impeça a participação no processo de contratação direta ou a futura contratação, mediante a consulta aos seguintes cadastros:

6.4.1. Sicaf;

6.4.2. Cadastro Nacional de Empresas Punidas – CNEP, mantido pela Controladoria-Geral da União (https://www.portaltransparencia.gov.br/sancoes/cnep).

6.5. A consulta aos cadastros será realizada no nome e no CNPJ da empresa fornecedora.

6.6. A consulta no CNEP quanto às sanções previstas na Lei nº 8.429, de 1992, também ocorrerá no nome e no CPF do sócio majoritário da empresa fornecedora, se houver, por força do art. 12 da citada lei.

6.7. Caso conste na Consulta de Situação do fornecedor a existência de Ocorrências Impeditivas Indiretas, o órgão diligenciará para verificar se houve fraude por parte das empresas apontadas no Relatório de Ocorrências Impeditivas Indiretas.

6.7.1. A tentativa de burla será verificada por meio dos vínculos societários, linhas de fornecimento similares, dentre outros.

6.7.2. O fornecedor será convocado para manifestação previamente a uma eventual desclassificação.

6.7.3. Constatada a existência de sanção, o fornecedor será reputado inabilitado, por falta de condição de participação.

6.8. Caso o fornecedor provisoriamente classificado em primeiro lugar tenha se utilizado de algum tratamento favorecido às ME/EPPs ou tenha se valido da aplicação da margem de preferência, o gestor verificará se o fornecedor faz jus ao benefício aplicado.

6.9. Verificadas as condições de participação e de utilização do tratamento favorecido, o gestor examinará a proposta classificada em primeiro lugar quanto à adequação ao objeto e à compatibilidade do preço em relação ao máximo estipulado para contratação neste Aviso de Contratação Direta e em seus anexos.

6.10. Será desclassificada a proposta vencedora que:

6.10.1. contiver vícios insanáveis;

6.10.2. não obedecer às especificações técnicas pormenorizadas neste Aviso ou em seus anexos;

6.10.3. apresentar preços inexequíveis ou que permanecerem acima do preço máximo definido para a contratação;[A2]

6.10.4. não tiver sua exequibilidade demonstrada, quando exigido pela Administração;

6.10.5. apresentar desconformidade com quaisquer outras exigências deste Aviso ou seus anexos, desde que insanável.

6.11. Se houver indícios de inexequibilidade da proposta de preço, ou em caso da necessidade de esclarecimentos complementares, poderão ser efetuadas diligências, para que o fornecedor comprove a exequibilidade da proposta.

6.12. Erros no preenchimento da planilha não constituem motivo para a desclassificação da proposta. A planilha poderá ser ajustada pelo fornecedor, no prazo indicado pelo sistema, desde que não haja majoração do preço e que se comprove que este é o bastante para arcar com todos os custos da contratação.

6.12.1. O ajuste de que trata este dispositivo se limita a sanar erros ou falhas que não alterem a substância das propostas;

6.12.2. Considera-se erro no preenchimento da planilha passível de correção a indicação de recolhimento de impostos e contribuições na forma do Simples Nacional, quando não cabível esse regime.

6.13. Para fins de análise da proposta quanto ao cumprimento das especificações do objeto, poderá ser colhida a manifestação escrita do setor requisitante do serviço ou da área especializada no objeto.

6.14. Se a proposta ou lance vencedor for desclassificado, será examinada a proposta ou lance subsequente, e, assim sucessivamente, na ordem de classificação.

6.15. Havendo necessidade, a sessão será suspensa, informando-se no “chat” a nova data e horário para a sua continuidade.

6.16. Encerrada a análise quanto à aceitação da proposta, será iniciada a fase de habilitação, observado o disposto neste Aviso de Contratação Direta.

7. DA FASE DE HABILITAÇÃO

7.1. Os documentos a serem exigidos para fins de habilitação, nos termos dos arts. 62 a 70 da Lei nº 14.133, de 2021, constam do Termo de Referência e serão solicitados do fornecedor mais bem classificado na fase de lances.

7.2. A habilitação dos fornecedores será verificada por meio do Sicaf, nos documentos por ele abrangidos.

7.2.1. É dever do fornecedor atualizar previamente as comprovações constantes do Sicaf para que estejam vigentes na data da abertura da sessão pública, ou encaminhar, quando solicitado, a respectiva documentação atualizada.

7.2.2. O descumprimento do subitem acima implicará a inabilitação do fornecedor, exceto se a consulta aos sítios eletrônicos oficiais emissores de certidões lograr êxito em encontrar a(s) certidão(ões) válida(s).

7.3. Quando permitida a participação de empresas estrangeiras que não funcionem no País, as exigências de habilitação serão atendidas mediante documentos equivalentes, inicialmente apresentados em tradução livre.

7.4. Na hipótese de o vencedor ser empresa estrangeira que não funcione no País, para fins de assinatura do contrato ou da ata de registro de preços, os documentos exigidos para a habilitação serão traduzidos por tradutor juramentado no País e apostilados nos termos do disposto no Decreto nº 8.660, de 29 de janeiro de 2016, ou de outro que venha a substituí-lo, ou consularizados pelos respectivos consulados ou embaixadas.

7.5. Na hipótese de necessidade de envio de documentos complementares, indispensáveis à confirmação dos já apresentados para a habilitação, ou de documentos não constantes do Sicaf, o fornecedor será convocado a encaminhá-los, em formato digital, por meio do sistema, no prazo de **02 (duas) horas**, sob pena de inabilitação.

7.6. Somente haverá a necessidade de comprovação do preenchimento de requisitos mediante apresentação dos documentos originais não-digitais quando houver dúvida em relação à integridade do documento digital.

7.7. Não serão aceitos documentos de habilitação com indicação de CNPJ/CPF diferentes, salvo aqueles legalmente permitidos.

7.8. Se o fornecedor for a matriz, todos os documentos deverão estar em nome da matriz, e se o fornecedor for a filial, todos os documentos deverão estar em nome da filial, exceto para atestados de capacidade técnica, e no caso daqueles documentos que, pela própria natureza, comprovadamente, forem emitidos somente em nome da matriz.

7.9. Serão aceitos registros de CNPJ de fornecedor matriz e filial com diferenças de números de documentos pertinentes ao CND e ao CRF/FGTS, quando for comprovada a centralização do recolhimento dessas contribuições.

7.10. O fornecedor provisoriamente vencedor em um item, que estiver concorrendo em outro item, ficará obrigado a comprovar os requisitos de habilitação cumulativamente, isto é, somando as exigências do item em que venceu às do item em que estiver concorrendo, e assim sucessivamente, sob pena de inabilitação, além da aplicação das sanções cabíveis.

7.11. Havendo necessidade de analisar minuciosamente os documentos exigidos, a sessão será suspensa, sendo informada a nova data e horário para a sua continuidade.

7.12. Será inabilitado o fornecedor que não comprovar sua habilitação, seja por não apresentar quaisquer dos documentos exigidos, ou apresentá-los em desacordo com o estabelecido neste Aviso de Contratação Direta.

7.12.1. Na hipótese de o fornecedor não atender às exigências para a habilitação, o órgão ou entidade examinará a proposta subsequente, e assim sucessivamente, na ordem de classificação, até a apuração de uma proposta que atenda às especificações do objeto e as condições de habilitação

7.13. Constatado o atendimento às exigências de habilitação, o fornecedor será habilitado.

8. DA ATA DE REGISTRO DE PREÇOS

8.1. Não se Aplica.

9. DA FORMAÇÃO DO CADASTRO DE RESERVA

9.1. Não se Aplica.

10. DA CONTRATAÇÃO

10.1 Após a homologação e adjudicação, caso se conclua pela contratação, será firmado Termo de Contrato ou emitido instrumento equivalente.

10.2. O adjudicatário terá o prazo de **03 (três) dias úteis**, contados a partir da data de sua convocação, para aceitar instrumento equivalente, conforme o caso (Nota de Empenho/Carta Contrato/Autorização), sob pena de decair o direito à contratação, sem prejuízo das sanções previstas neste Aviso de Contratação Direta.

> 10.2.1. Alternativamente à convocação para comparecer perante o órgão ou entidade para a assinatura do Termo de Contrato, a Administração poderá encaminhá-lo para assinatura, mediante correspondência postal com aviso de recebimento (AR), disponibilização de acesso à sistema de processo eletrônico para esse fim ou outro meio eletrônico, para que seja assinado e devolvido no prazo de **03 (três) dias úteis**, a contar da data de seu recebimento ou da disponibilização do acesso ao sistema de processo eletrônico.
>
> 10.2.2. O prazo previsto no subitem anterior poderá ser prorrogado, por igual período, por solicitação justificada do adjudicatário e aceita pela Administração.

10.3. O Aceite da Nota de Empenho ou do instrumento equivalente, emitida ao fornecedor adjudicado, implica o reconhecimento de que:

> 10.3.1. referida Nota está substituindo o contrato, aplicando-se à relação de negócios ali estabelecida as disposições da Lei nº 14.133, de 2021;
>
> 10.3.2. a contratada se vincula à sua proposta e às previsões contidas no Aviso de Contratação Direta e seus anexos;
>
> 10.3.3. a contratada reconhece que as hipóteses de rescisão são aquelas previstas nos arts. 137 e 138 da Lei nº 14.133, de 2021, e reconhece os direitos da Administração previstos nos arts. 137 a 139 da mesma Lei.

10.4. O prazo de vigência da contratação é o estabelecido no Termo de Referência.

10.5. Na assinatura do contrato ou do instrumento equivalente será exigida a comprovação das condições de habilitação e contratação consignadas neste aviso, que deverão ser mantidas pelo fornecedor durante a vigência do contrato.

11. DAS INFRAÇÕES E SANÇÕES ADMINISTRATIVAS

11.1. Comete infração administrativa o fornecedor que praticar quaisquer das hipóteses previstas no art. 155 da Lei nº 14.133, de 2021, quais sejam:

> 11.1.1. dar causa à inexecução parcial do contrato;

11.1.2. dar causa à inexecução parcial do contrato que cause grave dano à Administração, ao funcionamento dos serviços públicos ou ao interesse coletivo;

11.1.3. dar causa à inexecução total do contrato;

11.1.4. deixar de entregar a documentação exigida para o certame;

11.1.5. não manter a proposta, salvo em decorrência de fato superveniente devidamente justificado;

11.1.6. não celebrar o contrato ou não entregar a documentação exigida para a contratação, quando convocado dentro do prazo de validade de sua proposta;

11.1.7. ensejar o retardamento da execução ou da entrega do objeto da contratação direta sem motivo justificado;

11.1.8. apresentar declaração ou documentação falsa exigida para o certame ou prestar declaração falsa durante a dispensa eletrônica ou a execução do contrato;

11.1.9. fraudar a dispensa eletrônica ou praticar ato fraudulento na execução do contrato;

11.1.10. comportar-se de modo inidôneo ou cometer fraude de qualquer natureza;

11.1.10.1. Considera-se comportamento inidôneo, entre outros, a declaração falsa quanto às condições de participação, quanto ao enquadramento como ME/EPP ou o conluio entre os fornecedores, em qualquer momento da dispensa, mesmo após o encerramento da fase de lances.

11.1.11 praticar atos ilícitos com vistas a frustrar os objetivos deste certame; e

11.1.12 praticar ato lesivo previsto no art. 5º da Lei nº 12.846, de 1º de agosto de 2013.

11.1.13. O fornecedor que cometer qualquer das infrações discriminadas nos subitens anteriores ficará sujeito, sem prejuízo da responsabilidade civil e criminal, às seguintes sanções:

11.1.14. Advertência pela falta do subitem 11.1.1 deste Aviso de Contratação Direta, quando não se justificar a imposição de penalidade mais grave;

11.1.15. Multa de 10% (dez por cento) sobre o valor estimado do(s) item(s) prejudicado(s) pela conduta do fornecedor, por qualquer das infrações dos subitens 11.1.1 a 11.1.12;

11.1.16. Impedimento de licitar e contratar no âmbito da Administração Pública direta e indireta do ente federativo que tiver aplicado a sanção, pelo prazo máximo de 3 (três) anos, nos casos dos subitens 11.1.2 a 11.1.7 deste Aviso de Contratação Direta, quando não se justificar a imposição de penalidade mais grave;

11.1.17. Declaração de inidoneidade para licitar ou contratar, que impedirá o responsável de licitar ou contratar no âmbito da Administração Pública direta e indireta de todos os entes federativos, pelo prazo mínimo de 3 (três) anos e máximo de 6 (seis) anos, nos casos dos subitens 11.1.8 a 11.1.12, bem como nos demais casos que justifiquem a imposição da penalidade mais grave.

11.2. A aplicação das sanções previstas neste Aviso de Contratação Direta não exclui, em hipótese alguma, a obrigação de reparação integral do dano causado à Contratante.

11.3 Todas as sanções previstas neste Aviso poderão ser aplicadas cumulativamente com a multa.

11.4. Antes da aplicação da multa, será facultada a defesa do interessado no prazo de 15 (quinze) dias úteis, contado da data de sua intimação.

11.5. Se a multa aplicada e as indenizações cabíveis forem superiores ao valor do pagamento eventualmente devido pelo Contratante ao Contratado, além da perda desse valor, a diferença será descontada da garantia prestada ou será cobrada judicialmente.

11.6. Previamente ao encaminhamento à cobrança judicial, a multa poderá ser recolhida administrativamente no prazo máximo de 10 (dez) dias, a contar da data do recebimento da comunicação enviada pela autoridade competente.

11.7. A aplicação das sanções realizar-se-á em processo administrativo que assegure o contraditório e a ampla defesa ao Contratado, observando-se o procedimento previsto no caput e parágrafos do art. 158 da Lei nº 14.133, de 2021, para as penalidades de impedimento de licitar e contratar e de declaração de inidoneidade para licitar ou contratar.

11.8 Na aplicação das sanções serão considerados:

11.8.1. a natureza e a gravidade da infração cometida;

11.8.2. as peculiaridades do caso concreto;

11.8.3. as circunstâncias agravantes ou atenuantes;

11.8.4. os danos que dela provierem para o Contratante; e

11.8.5 a implantação ou o aperfeiçoamento de programa de integridade, conforme normas e orientações dos órgãos de controle.

11.9. Os atos previstos como infrações administrativas na Lei nº 14.133, de 2021, ou em outras leis de licitações e contratos da Administração Pública que também sejam tipificados como atos lesivos na Lei nº 12.846, de 1º de agosto de 2013, serão apurados e julgados conjuntamente, nos mesmos autos, observados o rito procedimental e autoridade competente definidos na referida Lei.

11.10. A personalidade jurídica do Contratado poderá ser desconsiderada sempre que utilizada com abuso do direito para facilitar, encobrir ou dissimular a prática dos atos ilícitos previstos neste Contrato ou para provocar confusão patrimonial, e, nesse caso, todos os efeitos das sanções aplicadas à pessoa jurídica serão estendidos aos seus administradores e sócios com poderes de administração, à pessoa jurídica sucessora ou à empresa do mesmo ramo com relação de coligação ou controle, de fato ou de direito, com o Contratado, observados, em todos os casos, o contraditório, a ampla defesa e a obrigatoriedade de análise jurídica prévia.

11.11. O Contratante deverá, no prazo máximo 15 (quinze) dias úteis, contado da data de aplicação da sanção, informar e manter atualizados os dados relativos às sanções por ele aplicadas, para fins de publicidade no Cadastro Nacional de Empresas Inidôneas e Suspensas (Ceis) e no Cadastro Nacional de Empresas Punidas (Cnep), instituídos no âmbito do Poder Executivo Federal.

11.12. As sanções de impedimento de licitar e contratar e declaração de inidoneidade para licitar ou contratar são passíveis de reabilitação na forma do art. 163 da Lei nº 14.133, de 2021.

11.13. As sanções por atos praticados no decorrer da contratação estão previstas nos anexos a este Aviso.

12. DAS DISPOSIÇÕES GERAIS

12.1. No caso de todos os fornecedores restarem desclassificados ou inabilitados (procedimento fracassado), a Administração poderá:

12.1.1. republicar o presente Aviso com uma nova data;

12.1.2 valer-se, para a contratação, de proposta obtida na pesquisa de preços que serviu de base ao procedimento, se houver, privilegiando-se os menores preços, sempre que possível, e desde que atendidas às condições de habilitação exigidas;

12.1.2.1. No caso do subitem anterior, a contratação será operacionalizada fora deste procedimento.

12.1.2.2.fixar prazo para que possa haver adequação das propostas ou da documentação de habilitação, conforme o caso.

12.2. As providências dos subitens 12.1.1 e 12.1.2 também poderão ser utilizadas se não houver o comparecimento de quaisquer fornecedores interessados (procedimento deserto).

12.3. Havendo a necessidade de realização de ato de qualquer natureza pelos fornecedores, cujo prazo não conste deste Aviso de Contratação Direta, deverá ser atendido o prazo indicado pelo agente competente da Administração na respectiva notificação.

12.4. Caberá ao fornecedor acompanhar as operações, ficando responsável pelo ônus decorrente da perda do negócio diante da inobservância de quaisquer mensagens emitidas pela Administração ou de sua desconexão.

12.5. Não havendo expediente ou ocorrendo qualquer fato superveniente que impeça a realização do certame na data marcada, a sessão será automaticamente transferida para o primeiro dia útil subsequente, no mesmo horário anteriormente estabelecido, desde que não haja comunicação em contrário.

12.6. Os horários estabelecidos na divulgação deste procedimento e durante o envio de lances observarão o horário de Brasília-DF, inclusive para contagem de tempo e registro no Sistema e na documentação relativa ao procedimento.

12.7. No julgamento das propostas e da habilitação, a Administração poderá sanar erros ou falhas que não alterem a substância das propostas, dos documentos e sua validade jurídica, mediante despacho fundamentado, registrado em ata e acessível a todos, atribuindo-lhes validade e eficácia para fins de habilitação e classificação.

12.8. As normas disciplinadoras deste Aviso de Contratação Direta serão sempre interpretadas em favor da ampliação da disputa entre os interessados, desde que não comprometam o interesse da Administração, o princípio da isonomia, a finalidade e a segurança da contratação.

12.9. Os fornecedores assumem todos os custos de preparação e apresentação de suas propostas e a Administração não será, em nenhum caso, responsável por esses custos, independentemente da condução ou do resultado do processo de contratação.

12.10. Em caso de divergência entre disposições deste Aviso de Contratação Direta e de seus anexos ou demais peças que compõem o processo, prevalecerá as deste Aviso.

12.11. Da sessão pública será divulgada Ata no sistema eletrônico.

12.12. Integram este Aviso de Contratação Direta, para todos os fins e efeitos, os seguintes anexos:

12.12.1 ANEXO I – Formulário de Condição de Fornecimento;

12.12.2. ANEXO II – Modelo de Autorização de Compras/Serviços;

São José dos Campos, [dia] de [mês] de [ano].

13. Responsáveis

Todas as assinaturas eletrônicas seguem o horário oficial de Brasília e fundamentam-se no §3º do Art. 4º do Decreto nº 10.543, de 13 de novembro de 2020.

JOSE ARISTEU DE SOUZA RUAS

Chefe de Serviço de Compras, Recebimento e Importação - SECRI

Assinou eletronicamente em 02/10/2025 às 10:35:24.

INSTITUTO NACIONAL DE PESQUISAS ESPACIAIS
Av. dos Astronautas, 1758, - Bairro Jardim da Granja,
CEP 12227-010, São José dos Campos - SP - http://www.inpe.br/

AUTORIZAÇÃO DE COMPRA/SERVIÇO

AUTORIZAÇÃO DE COMPRA/SERVIÇO		**Nº: 115/2025**	
DE: 90106/2025		**Dispensa Eletrônica: 256/2025**	**SÃO JOSÉ DOS CAMPOS, 2 de Outubro de 2025**
IOP PUBLISHING			
CNPJ:		**IE:**	
Endereço: N.2 THE DISTILLERY, GLASSFIELDS,AVON STREET,BRISTOL BS2 OGR UK Bairro: - Cidade/UF: EXTERIOR / EX			
Telefone: ,	**Fax:**	**CEP:**	
Banco:	**C/C:**	**Agência:**	
Nome Banco:	**Contato:**		
Email: ,			
Chave Pix:			

Item ATA	Código	Descrição / Observação	Unid.	Qtde.	Preço Unitário	IPI %	Total
1	13141	PUBLICAÇÃO DE ARTIGO CIENTÍFICO EM REVISTA	SV	1.00	R$ 15.123,02	0.00	R$ 15.123,02

		INTERNACIONAL E NACIONAL .					
					Total:	R$ 15.123,02	

Observações:
Conforme proposta datada de 11 de setembro de 2025; **Serviço deverá ser prestado no INPE/São José dos Campos/SP;** **Amparo legal: art. 75, Inciso II da Lei 14.133 de 1º de abril de 2021;** **Sanções e Multa moratória, será aplicada em caso de inadimplência, conforme item 11 do edital;** **Esta autorização de Compras/serviço, somente terá validade mediante Nota de empenho;** **Referente ao processo SEI n° 01340.006530/2025-30**
Local de entrega: MINISTÉRIO DA CIÊNCIA, TECNOLOGIA E INOVAÇÃO - MCTI - AV. DOS ASTRONAUTAS, 1758 JD. DA GRANJA SÃO JOSÉ DOS CAMPOS São Paulo CEP: 12227-010 CNPJ: 01.263.896/0005-98 IE: ISENTO Telefone: +55(12)3208-6993 Telefone 2: +55(12)3208-6105 Fax:
- Condições de Fornecimento -
Prazo de entrega...: 5 dias
Prazo de pagamento...: 10 DIAS UTEIS
Validade da proposta...: 60 dias
O faturamento deverá ser para:
Ministério da Ciência, Tecnologia e Inovação - MCTI
AV. DOS ASTRONAUTAS, 1758 JD. DA GRANJA SÃO JOSÉ DOS CAMPOS, SP CEP: 12227-010
CNPJ: 01.263.896/0005-98 IE: ISENTO Telefone: +55(12)3208-6993 Fax:

Documento assinado eletronicamente por **José Aristeu de Souza Ruas**, **Chefe do Serviço de Compras, Recebimento e Importação**, em 02/10/2025, às 15:41 (horário oficial de Brasília), com fundamento no § 3º do art. 4º do Decreto nº 10.543, de 13 de novembro de 2020.

Documento assinado eletronicamente por **Raul Ferreira da Silva Junior**, **Ordenador de Despesas**, em 03/10/2025, às 10:49 (horário oficial de Brasília), com fundamento no § 3º do art. 4º do Decreto nº 10.543, de 13 de novembro de 2020.

A autenticidade deste documento pode ser conferida no site https://sei.mcti.gov.br/verifica.html, informando o código verificador **13194819** e o código CRC **B2EC16D5**.

INSTITUTO NACIONAL DE PESQUISAS ESPACIAIS
Serviço de Compras, Recebimento e Importação
Coordenação de Administração
Coordenação-Geral de Gestão Organizacional
Instituto Nacional de Pesquisas Espaciais

ORDEM DE COMPRA REFERENTE AO PROCESSO	Processo de Compra: 90106/2025

Ordem de Compra: 115/2025

Fornecedor: IOP PUBLISHING

Item	Requisição	Material	Fonte	PTRES	P.I.	ND.	Qtd Comprada	Preço Unitário	Valor Total
1	DIHPA-017/2025-RC	13141	1000	233467	955656-PO09	33903992	1,00000	R$ 15.123,02	R$ 15.123,02
Total:									R$ 15.123,02

Resumo do Processo: 90106/2025

Fonte	PTRES	P.I.	ND.	Valor Total
1000	233467	955656-PO09	33903992	R$ 15.123,02
Valor Total das OCs:				R$ 15.123,02

Documento assinado eletronicamente por **José Aristeu de Souza Ruas**, **Chefe do Serviço de Compras, Recebimento e Importação**, em 02/10/2025, às 15:41 (horário oficial de Brasília), com fundamento no § 3º do art. 4º do Decreto nº 10.543, de 13 de novembro de 2020.

SIAFI Sistema Integrado de Administração Financeira do Governo Federal

TESOURO NACIONAL

Data e hora da consulta: 03/10/2025 16:42
Usuário: ***.848.099-**
Impressão Completa

Nota de Empenho

UG Emitente

Código	Nome	Moeda
240106	INSTITUTO NACIONAL DE PESQ. ESPACIAIS-INPE	REAL - (R$)

CNPJ	Endereço	CEP
01.263.896/0005-98	AV.DOS ASTRONAUTAS, NR. 1.758	12227-010

Município	UF	Telefone
SAO JOSE DOS CAMPOS	SP	(012) 32086079 - 32086080 - 32086075-32086081

Ano	Tipo	Número
2025	NE	410

Célula Orçamentária

Esfera	PTRES	Fonte de Recurso	Natureza da Despesa	UGR	Plano Interno
1	233467	1000000000	339039	-	955656-PO09

Data de Emissão	Tipo	Processo	Taxa de Câmbio	Valor
03/10/2025	Estimativo	01340.006530/2025-30	0,0000	15.123,02

Favorecido

Código	Nome
EX3613023	IOP PUBLISHING

Endereço	CEP
TEMPLE CIRCUS, TEMPLE WAY, BRISTOL BS1 6HG, UK - REINO UNIDO	00000-000

Município	UF	Telefone
		+44(0)117 929 7481

Amparo Legal

Código	Modalidade de Licitação
139	DISPENSA DE LICITACAO

Ato Normativo	Artigo	Parágrafo	Incíso	Alínea
LEI 14.133 / 2021	75	-	II	-

Descrição

PUBLICACAO DE ARTIGO CIENTIFICO EM REVISTA INTERNACIONAL E NACIONAL CONFORME REQUISICAO DIHPA-017/2025-RC SEI 13100660, D.E. N. 256/2025 SEI 13194819 E AUTORIZACAO DE COMPRA Nº 115/2025 SEI 13194819. PTRES 233467. TED INPE/AEB Nº 955656/2024.

Local da Entrega

INPE - SAO JOSE DOS CAMPOS

Informação Complementar

24010606002562025 - UASG Minuta: 240106

Sistema de Origem

COMPRASNET-ME

Versão	Data/Hora	Operação
002	03/10/2025 16:33:37	Alteração

Data e hora da consulta: 03/10/2025 16:42
Usuário: ***.848.099-**
Impressão Completa

Nota de Empenho

Lista de Itens

Natureza de Despesa	Total da Lista
339039 - OUTROS SERVICOS DE TERCEIROS - PESSOA JURIDIC	15.123,02

Subelemento 92 - SERVICOS DE PUBLICIDADE INSTITUCIONAL

Seq.	Descrição	Valor do Item
001	Item compra: 00001 - Publicacao, impressao de jornal / revista / livro	15.123,02

Data	Operação	Quantidade	Valor Unitário	Valor Total
03/10/2025	Inclusão	1,00000	15.123,0200	15.123,02

Assinaturas

Ordenador de Despesa	Gestor Financeiro
RAUL FERREIRA DA SILVA JUNIOR	EDUARDO AMORIM MARTINS DE SOUZA
***.163.688-**	***.773.344-**
03/10/2025 16:33:37	03/10/2025 16:28:58

Versão	Data/Hora	Operação
002	03/10/2025 16:33:37	Alteração